NICHTMETALLISCH-ANORGANISCHE WERKSTOFFE (NAW)

Lead-free high-temperature dielectrics in the $Bi_{0.5}Na_{0.5}TiO_3$-$BaTiO_3$ and $Bi_{0.5}Na_{0.5}TiO_3$-$BaTiO_3$-$K_{0.5}Na_{0.5}NbO_3$ systems

Matias Acosta

07/15/2011

Director: Prof. Dr. Jürgen Rödel
Advisor: Lic. Gerardo G. Thern

TECHNISCHE
UNIVERSITÄT
DARMSTADT

MATERIAL-
WISSENSCHAFT

Matias Acosta

Course: Materials engineering, Institute of Technology “Prof. Jorge A. Sabato“, Buenos Aires, Argentina.

Master Thesis
Topic: "Lead-free high-temperature dielectrics in the $Bi_{0.5}Na_{0.5}TiO_3$-$BaTiO_3$ and $Bi_{0.5}Na_{0.5}TiO_3$-$BaTiO_3$-$K_{0.5}Na_{0.5}NbO_3$ systems"

Date: 07/15/2011

Director: Prof. Dr. Jürgen Rödel

Advisor: Lic. Gerardo G. Thern

This work was performed in:

Fachgebiet Nichtmetallisch-Anorganische Werkstoffe
Fachbereich Material- und Geowissenschaften
Technische Universität Darmstadt
Petersenstraße 23
64287 Darmstadt

Solemn Declaration

I do solemnly declare that I have made this work independently. All taken thoughts from foreign sources directly or indirectly are identified as such. The work will be submitted only to an examination board from the Institute of Technology “Prof. Jorge A. Sabato” and has not been published yet.

Matias Acosta

Darmstadt, 15th July 2011

Abstract

The motivation guidelines for the development of new high-temperature wide operational range dielectrics are given. Afterwards, the fundamental physics of dielectricity are described, followed by a brief general description of ferroelectricity and piezoelectricity. Moreover, the material detailed requirements for high-temperature dielectrics are given and a literature review of materials with suitable properties for high-temperature capacitors is presented.

Regarding the experimental part, lead-free high-temperature dielectrics in the $Bi_{0.5}Na_{0.5}TiO_3$-$BaTiO_3$ and $Bi_{0.5}Na_{0.5}TiO_3$-$BaTiO_3$-$K_{0.5}Na_{0.5}NbO_3$ systems doped with different concentrations of $CaZrO_3$ were synthesized. Their structural, microstructural and electrical properties were characterized.

Keywords: ferroelectric materials, lead-free ferroelectric materials, BNT, BNT-BT, BNT-BT-KNN, high-temperature dielectrics, relaxor ferroelectrics.

Acknowledgements

The research work of this thesis was carried out between February 2011 and July 2011 in the “Nichtmetallisch-AnorganischeWerkstoffe” group led by Prof. Dr.-Ing. Jürgen Rödel, Department of Materials and Earth Sciences, Technische Universität Darmstadt.

I would like to thank first Prof. Dr. Jürgen Rödel. I wouldn’t have been able to work in this group of excellence in ceramic materials without his consent. He showed always support on my work and on me. He always respected my ideas and allowed me to perform new experiments, thus encouraging me to obtain new and improved results. I would like to say that his open mind, respect, gentleness and dedication for work and people are qualities worthy of admiration.

I would like to thank also Dr. Wook Jo. He was my referent for doubts and concerns during this work. His dedication, knowledge in the field and gentleness were of great help. His comments were important to enrich and improve my results and knowledge in ferroelectric materials.

I would like to give a special thank to M. Sc. Jiadong Zang. He was my direct referent for personal doubts and professional concerns. I learned from him all kind of work-related issues, from fundamental physics to operating equipment details. Moreover, he helped me in all the non-technical aspects of this work. His kindness, gentleness and predisposition were present at all times. Without his support, inspiration and assistance this work would not have been possible.

I would also like to thank the other members of Nichtmetallisch-AnorganischeWerkstoffe group and my roommates because they were very kind with me. They taught me a lot of things and they showed me the German customs.

I would also like to thank some people that supported me from the very beginning of this work proposal. From the Institute of Technology “Prof. Jorge A. Sabato”, my referent Lic. Gerardo G. Thern. He showed me his support and kindness at all stages of this work. He was always with an admiring predisposition to help me in specific doubts during the work. Dr. Pablo Levy and Lic. Gerardo G. were my advisors of the Spanish version of the present work. They both were of great help and their contributions were really important to enrich and improve my work. I would also like to thank some other people from the Institute of Technology “Prof. Jorge A. Sabato” that helped me to achieve my goal of doing my thesis in Prof. Dr. Jürgen Rödel’s group.

In this context, I would like to help Prof. Dr. Andrés J. Kreiner, Prof. Dr. José R. Galvele, Dra. Vivianne Bruyere, Prof. Dra. Delia Arias, Prof. Dr. Rubén Weht, Prof. Dr. Roberto C. Pasianot, Dra. Liliana Roberti and Prof. Dr. José Ovejero García. Their support at early stages of this work proposal was of great help to obtain this position.

Last but not least, I would like to thank my family, friends and colleagues from the Institute of Technology Prof. Jorge Sabato. My father and mother unconditional love and support to me, as well as from the rest of my family, were of great importance for me in order first to start studying materials engineering and afterwards in my decision of accepting this work proposal. All my personal and professional achievements are due to them and I think my eternal gratitude cannot be described in just a few words. My friends and colleagues, my second family, are of great importance in my life. Their love and support, as well as approval, are major concerns in my life decisions. Without their help and support this work could not have been done. I would also like to express to these lasts persons my love and thank them for being part of my life. This work is product and dedicate to them.

Matias Acosta

Darmstadt, 15th July 2011

Contents

List of figures

Figure 39: Imaginary relative permittivity vs. temperature for the BNT-BT-0.05CZ sample. Three frequency dependent thermal hysteresis loops from 40 to 92 ºC, 92 to 212 ºC and 212 ºC to higher temperatures than measured are observed (the crossing temperatures were measured at 1 kHz and are marked with arrows). They may be related with the presence of nanopolar regions, their different time response and thermal stability.

Figure 40: Imaginary relative permittivity vs. temperature for the BNT-BT-0.2CZ sample. Note that the anomaly at T_1 can be observed but at lower temperatures, in this case T_1= -130 ºC, measured at 1 kHz.

Figure 41: Effect of the 1150 ºC and 1200 ºC sintering temperatures in the BNT-BT-0.15CZ and BNT-BT-0.2CZ samples, respectively. Note that the relative permittivity is increased compared to that of the samples sintered at 1100 ºC.

Figure 42: Relative permittivity vs. low (left) and high (right) temperatures measured at frequencies from 100 Hz to 1 MHz for the BNT-BT-KNN-CZ system. Note that the anomalies for the 5% CZ sample are marked.

Figure 43: Loss factor vs. low (left) and high (right) temperatures measured at frequencies from 100 Hz to 1 MHz for the BNT-BT-KNN-CZ system. The anomalies at T_1 and T_2 for the 5% CZ sample are marked; while for the 10% CZ sample the one at T_f is marked.

Figure 44: Imaginary relative permittivity vs. temperature for the BNT-BT-KNN-0.05CZ sample. Note that that two anomalies are observed in for this system at T_1= 15 ºC and T_2= 180 ºC, as was reported for the BNT-BT-CZ system. Nevertheless, in this case the anomaly at high-temperatures presents a more diffuse shape and can be seen clearly in the inset at 100 Hz (the arrows mark the change in curvature of the 100 Hz curve).

Figure 45: Imaginary relative permittivity vs. temperature for the BNT-BT-KNN-0.05CZ sample. Note the two frequency dependent thermal hysteresis loops observed in the temperature ranges from 10 to 130 ºC and from 130 ºC to higher temperatures than measured (the crossing temperatures are measured at 1 kHz and marked with arrows).

Figure 46: Effect of CZ doping on the relative permittivity of the BNT-BT-CZ system. All the curves correspond to a frequency of 1 kHz. Note the flattened and decreased relative permittivity curves obtained with increasing CZ doping.

Figure 47: Effect of CZ doping on the loss factor of the BNT-BT-CZ system. All the curves correspond to a frequency of 1 kHz. Note that the low-temperature loss factor is reduced with increasing CZ doping, while the conductivity is increased.

Figure 48: Effect of CZ doping on the relative permittivity of the BNT-BT-KNN-CZ system. All the curves correspond to a frequency of 1 kHz. Note the flattened and decreased relative permittivity curves obtained with increasing CZ doping.

List of tables

Abbreviations

E	Macroscopic electric field inside a body
E_0	External electric field
E_1	Depolarization field
D	Electric displacement
ε	Permittivity of a medium
ε_0	Permittivity of vacuum
μ_0	Vacuum permeability
C	Speed of light
χ	Susceptibility
ε_r	Relative permittivity
$\tan(\delta)$	Loss factor
Q_s	Quality factor
P	Polarization
α	Polarizability
d	Piezoelectric constant

T	Applied stress
S	Strain
T_c	Curie temperature
MPB	Morphotropic phase boundary
P_{sat}	Saturation polarization
P_r	Remanent polarization
E_c	Coercive field
P_s	Spontaneous polarization
T_0	Critical temperature
C	Curie constant
γ	Diffuseness exponent
T_m	Temperature of the maxima relative permittivity
T_d	Depolarization temperature
R	Resistance
C	Capacitance
τ	Response time
T_g	Glass transition temperature
FP	Fluorinated polybenzoxazoles
FP-E	Fluorinated polyimide with adamantyl ester pendant
FP-D	Fluorenyl polyester with 4,9-diamantyl group
FPy	Fluorene polyester
BT	$BaTiO_3$
BNT	$Bi_{0.5}Na_{0.5}TiO_3$
BN	$BiNbO_4$
CZ	$CaZrO_3$
KNN	$K_{0.5}Na_{0.5}NbO_3$
KNLN	$(K_{0.5}Na_{0.5})_{0.94}Li_{0.06}NbO_3$
ZMT	$Zn_{0.8}Mg_{0.2}TiO_3$
k_p	Coupling factor
BZT	$Ba(Ti,Zr)O_3$
FC	Furnace cooling
OFC	Open Furnace cooling
XRD	X-ray diffraction
DSC	Differential scanning calorimetry
δ_{ss}	Calculated density
DW	Dry weight
SWW	Saturated weight in water
SWA	Saturated weight in air
DC	Direct current
C_s	Sample capacity
C_m	Measurement capacity

1 Introduction

Dielectric materials are widely used in electrical devices and components such as capacitors and electronic switching devices [1]. The main purpose of the present work is to develop dielectric materials with suitable properties for high-temperature capacitors. Among the required passive devices, the capacitor is probably one of the most challenging components [2]. Ceramic capacitors are used in a variety of functions in electrical circuits and they constitute indispensable components for passive parts in contemporary electronic devices. Among their uses can be mentioned bypassing, coupling, decoupling, filtering, tension smoothing, pulse discharge, snubbing, power conditioning, etc [3] [4]. The mentioned applications imply that the market related to capacitors is growing each day [5]. This increasing demand results in higher requirements on capacitor materials such as improving performance and reliability. Furthermore, new technological applications that need to be operated in harsh environments are becoming popular in automotive, petrochemical, aero/astronautics and nuclear industries. This trend is due to the arising integrated technologies in control and sensor systems that help to reduce costs, fuel consumption and increase the performance of technological devices. Most of these applications are subjected to high-temperatures beyond 200 ºC. Hence, the limit of operating temperature becomes a severe design constraint and hinders further development [6-8]. For these reasons, the dielectric materials used in ceramic capacitors must fulfill many properties in order to be used with a reliable service as a capacitor. Among the most important properties can be mentioned a high relative permittivity (ε_r), high resistivity even at high-temperatures (beyond 200 ºC), a high RC constant and a low dielectric loss ($\tan(\delta)$). In order to obtain dielectric materials with these properties it was decided to use BNT-based materials. Moreover, it is known that one variable to change a material property is to dope it with other elements. For this reason, in order to obtain high-temperature dielectric materials with suitable properties it was decided to synthesize the $(1–x)(0.94Bi_{0.5}Na_{0.5}TiO_3–0.06BaTiO_3)–xCaZrO_3$ and $(1–x)(0.82(0.94Bi_{0.5}Na_{0.5}TiO_3–0.06BaTiO_3)–0.18K_{0.5}Na_{0.5}NbO_3)–xCaZrO_3$ (x=0, 0.05, 0.1 and 0.2) systems. Afterwards, a characterization of these materials regarding structural, microstructural and electrical properties was done. Among the techniques used for the structural and microstructural characterization can be mentioned density, high-resolution electron microscopy

(HREM), X-ray diffraction (XRD) and differential scanning calorimetric measurements (DSC). Regarding the electrical characterization the techniques used were temperature and frequency dependent ε_r and tan(δ), direct current (DC), polarization and strain measurements.

2 Theoretical background

2.1 Dielectricity

2.1.1 Macroscopic physics of dielectricity

The macroscopic electric field inside a body (**E**) has two contributions: one is that of the applied external electric field ($\mathbf{E_0}$), while the other is the sum of the fields of all charges that constitute the body. The latter contribution may be expressed in terms of the sum of the fields of all the atomic dipoles of the specimen. To simplify this calculation, the macroscopic electric field caused by a uniform polarization (*i.e.* a uniform polarization must be assumed) can be replaced by an electric field in vacuum of a ficticious surface charge density. This charge will create an electric field called depolarization field ($\mathbf{E_1}$) that will oppose $\mathbf{E_0}$. Taking into account this mentioned mathematical artifice, **E** is defined as the sum of $\mathbf{E_0}$ and $\mathbf{E_1}$ ($\mathbf{E}=\mathbf{E_0}+\mathbf{E_1}$). Therefore, the polarization **P** is defined as the dipole moment per unit of volume, averaged over the volume of a cell[1].

The electric displacement (**D**) in a medium is defined in Equation 1.

$$\mathbf{D} = \varepsilon\mathbf{E} \qquad \text{Equation 1,}$$

where the permittivity (ε) of a homogeneous and isotropic medium relative to vacuum with instantaneous response is defined in terms of the macroscopic field **E** (Equation 2):

$$\varepsilon = \frac{\varepsilon_0\mathbf{E} + \mathbf{P}}{\mathbf{E}} \qquad \text{Equation 2}$$

Hence, the **P** can be calculated as[2]:

$$\mathbf{P} = \mathbf{D} - \varepsilon_0\mathbf{E} \qquad \text{Equation 3,}$$

where ε_0 is a universal constant called permittivity of vacuum and is given by:

---

[1] All the vectorial variables will be written with emphasis.

[2] The mathematical expressions will be given for ideal homogeneous and isotropic materials.

$$\varepsilon_0 = \frac{1}{\mu_0\, \mathrm{C}^2} = 8{,}854118 \cdot 10^{-12}\ \mathrm{F/m} \qquad \text{Equation 4,}$$

where μ_0 is the vacuum permeability and C the speed of light.

The susceptibility χ is another property that describes the response of a material to $\mathbf{E_0}$. It is related to the ε of a homogeneous and isotropic medium by Equation 5.

$$\chi = \frac{\boldsymbol{P}}{\varepsilon_0 \mathbf{E}} = \varepsilon - 1 \qquad \text{Equation 5}$$

The relative permittivity (ε_r) of a dielectric material is a dimensionless physical quantity equal to the ratio of the permittivity of the medium to the permittivity of vacuum. It is also sometimes miscalled the dielectric constant of the medium[3]. Hence, it is defined by the equation:

$$\varepsilon_r = \frac{\varepsilon}{\varepsilon_0} \qquad \text{Equation 6}$$

It should be noted that ε_r depends on the frequency of $\mathbf{E_0}$ (if the applied field is alternating) and can be described as a complex physical quantity, where the imaginary part is related to dielectric losses:

$$\varepsilon_r = \varepsilon_r^{'} + \mathrm{i} \cdot \varepsilon_r^{''} \qquad \text{Equation 7,}$$

where $\varepsilon_r^{'}$ is the real part of the relative permittivity, $\varepsilon_r^{''}$ the imaginary part of the relative permittivity and i the imaginary unit.

---

[3] Some authors use the term dielectric constant referring to the permittivity of a medium, relative permittivity or the static relative permittivity, indistinctly. This term should not be used to avoid confusions among the different mentioned material properties.

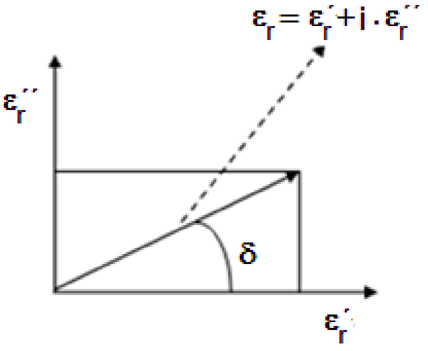

Figure 1: Relative permittivity in the complex plane, where a phase difference δ between the real and imaginary parts is observed.

In an ideal loss-less dielectric material (*i.e.* perfect capacitor), there is a phase difference between the current ($I = i_{max}\cos(wt)$) and the voltage ($V = v_{max}\sin(wt)$) of 90°. By contrast in the presence of dielectric losses, the phase difference is equal to 90°–δ (Figure 1). Taking this into account, the loss tangent is defined as the tangent of δ (tan(δ)), term which is also called dissipation factor[4]. This property is an intrinsic material property, *i.e.* it does not depend on the geometry of a capacitor (in contrast to the capacity which does depend on the geometry of it) and can be calculated with the Equation 8.

$$\tan(\delta) = \frac{\varepsilon_r''}{\varepsilon_r'} \qquad \text{Equation 8}$$

Dielectric losses are usually dissipated as heat inside the dielectric material and in the surroundings. The dissipated power (Pw) can be expressed as:

$$Pw = 2\pi\, f\, E_0^2 \tan\delta \qquad \text{Equation 9,}$$

where f is the frequency of $\mathbf{E_0}$**.** It can be seen that the power dissipation depends on the amplitude and frequency of the applied external electric field, as well as the loss factor [9-11].

---

[4] The term quality factor Q_s defined as 1/tan(δ) is often used in literature as well.

2.1.2 Microscopic physics of dielectricity

All the mentioned physic relations in the previous section were macroscopic. Nevertheless, physics of dielectrics can be also deduced in terms of the microscopic structure of a material.

The **P** of a crystal may be expressed as a result of four different microscopic contributions: electronic, ionic, dipolar and space charge polarization (also called interfacial polarization). Each contribution can be expressed in terms of the polarizability (α) of a material, which represents its dynamical response to external fields. These relations can be seen in Equation 10 and Equation 11.

$$\alpha_j = \alpha_j^e + \alpha_j^i + \alpha_j^d + \alpha_j^{sc}$$ Equation 10

$$\mathbf{P} = \sum_j N_j \mathbf{p_j} = \sum_j N_j \alpha_j \, \mathbf{E}_{\boldsymbol{local}}(j)$$ Equation 11,

where α_j is the polarizability corresponding to the material, α_j^e the electronic contribution, α_j^i the ionic contribution, α_j^d the dipolar contribution, α_j^{sc} the space group contribution; and $\mathbf{p_j}$ is the total dipole moment, N_j the concentration of atoms, $\mathbf{E_{local}}(j)$ the local field; all referred at atom sites j.

The electronic contribution is common to all materials, as it arises from the displacement of the electron shell relative to a nucleus due to the action of an electric field, resulting in an electric dipole. The ionic contribution comes from the displacement of a charged ion with respect to other ions. This contribution is common in ionic solids and thus can be high in certain ceramic materials. The dipolar polarizability arises from molecules with a permanent electric dipole moment that can change orientation in with $\mathbf{E_0}$. The space charge polarization refers to a phenomenon that arises due to charges that exist from contaminants or geometry of interfaces. Charges may accumulate in the structural interfaces which result in an extra contribution. This effect could have important consequences in heterogeneous materials [9-11].

The variation of α with frequency reflects the mentioned contributions and gives rise to the frequency dependence of the **P (**Figure 2).

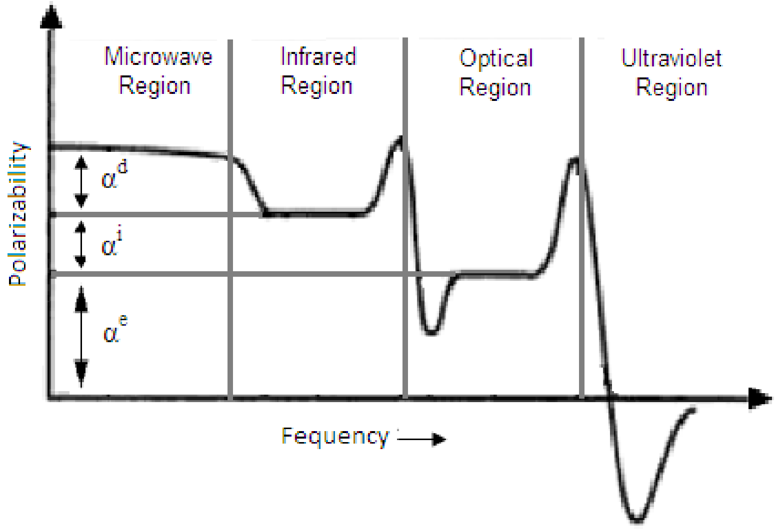

Figure 2: Variation of total polarizability with frequency. The three most important contributions to the materials polarizability can be seen; α^d: dipolar polarizability, α^i: ionic polarizability and α^e: electronic polarizability.

In the case that the Lorentz's relation ($\mathbf{E_{local}} = \mathbf{E} + \frac{\mathbf{P}}{3\varepsilon_0}$) is fulfilled, the macroscopic ε can be related to the electronic polarizability, *i.e.* a microscopic parameter, (discarding the other contributions) by the well known Clausius-Mossotti relation (Equation 12).

$$\frac{\varepsilon - 1}{\varepsilon + 2} = \frac{1}{3\varepsilon_0}\sum_j N_j\,\alpha_j^e \qquad \text{Equation 12}$$

2.2 Ferroelectricity

2.2.1 General information

Since the discovery of ferroelectricity in single-crystal materials (Rochelle salt) in 1921 and its subsequent extension into polycrystalline ceramics (such us in $BaTiO_3$) during the 1940s, there has been a continuous succession of new materials and technology developments related to ferroelectric materials. Among these applications are capacitors, piezoelectric sonar and ultrasonic transducers, radio and communication filters, and others [12] [13].

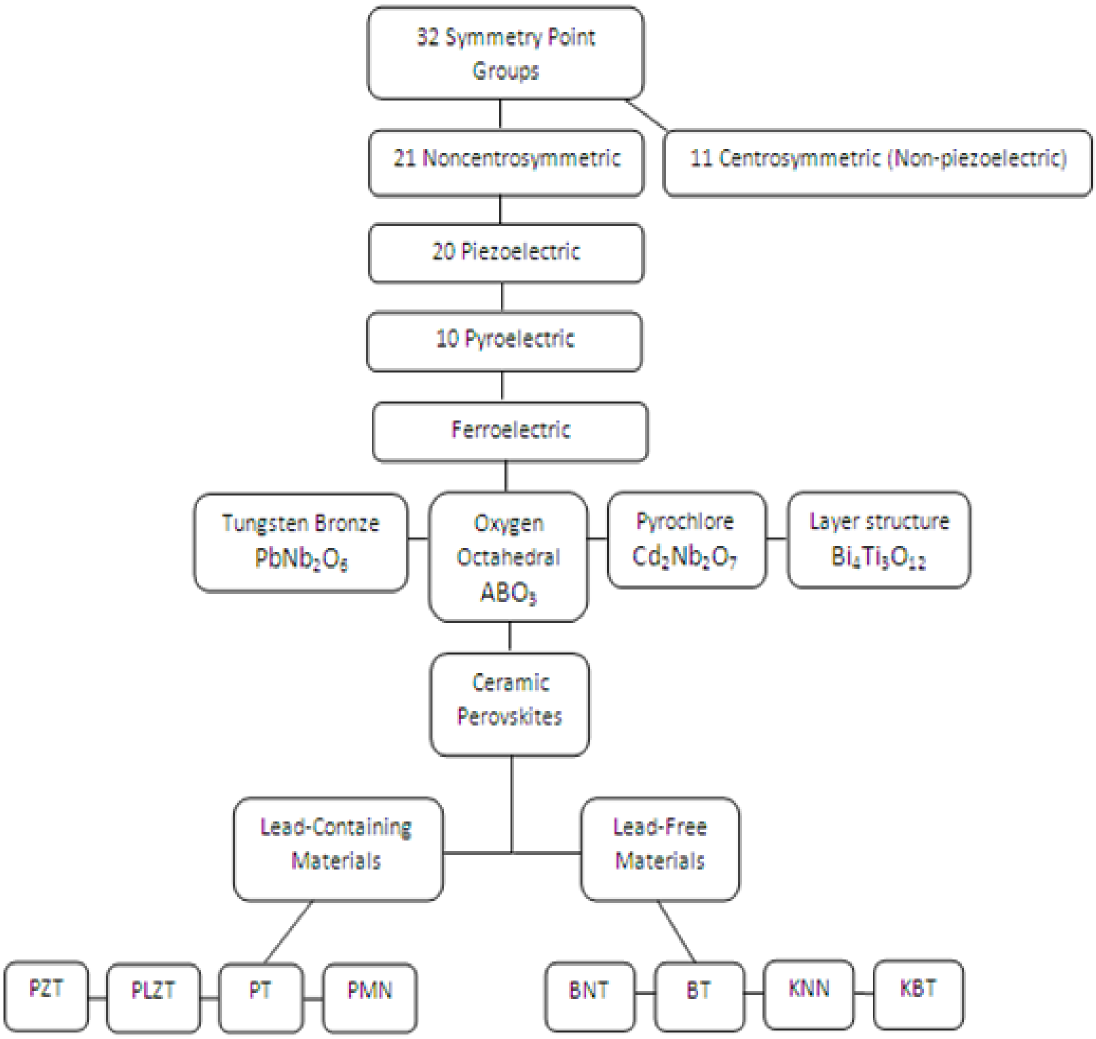

Figure 3: General materials classification according to their electrical properties.

The crystal structures found in nature can be divided into 32 different point symmetry groups[5] (Figure 3), from which 21 are non-centrosymmetric. From these, 20 have the characteristic of being piezoelectric. Piezoelectric materials are those that become polarized or undergo a change in polarization when they are stressed; conversely, when an electric field is applied they become strained. This can be seen in the following expressions:

$$P = d \cdot T \text{ (Direct effect)} \qquad \text{Equation 13}$$

$$S = d \cdot E_0 \text{ (Converse effect)} \qquad \text{Equation 14,}$$

---

[5] By symmetry point group the reader should understand crystal structures that are divided into groups taking into account rotations, reflexions and roto-reflexions of atoms around a coordinate axis.

where P is the polarization in response to the applied stress T, d is the piezoelectric coefficient and S the strain due to the applied external electric field $\mathbf{E_0}$.

Another electromechanical effect that exists in all materials, including the piezoelectric ones, is the electrostriction. In this property, contrary to the piezoelectric effect, the strain that occurs with an external electric field is proportional to the square power of $\mathbf{E_0}$ (Equation 15). This means in practical terms that electrostriction produces an expansion in most materials in the direction of the field regardless of its polarity, and this expansion relaxes back to zero when the field is removed.

$$S = M \cdot E_0^2 \qquad \text{Equation 15,}$$

where S is the strain due to the applied external electric field $\mathbf{E_0}$ and M the electrostriction constant.

From the 20 piezoelectric symmetry groups, 10 present the additional characteristic of being pyroelectric (Figure 3), which means that a change in temperature produces a change in their polarization. Unlike the more general piezoelectric classes, pyroelectrics develop a polarization spontaneously and form permanent dipoles in the structure. A subgroup of pyroelectrics is formed by the ferroelectric materials. These materials possess also spontaneous dipoles; however, unlike pyroelectrics, these dipoles are reversible, *i.e.* can be reoriented by an electric field of some magnitude less than the dielectric breakdown of the material itself[6]. These crystals present regions with uniform polarization called ferroelectric domains which are separated by interfaces called domains walls. There are many types of spontaneously polarized materials that present different characteristics regarding their domain orientation. These materials can be seen in a classical view in Figure 4.

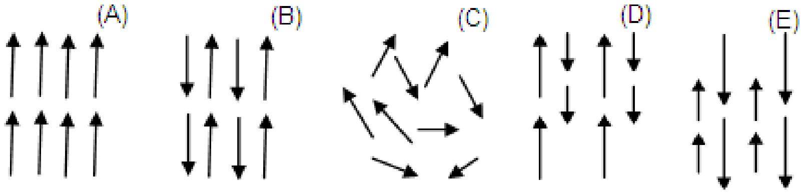

Figure 4: Scheme showing domain orientations in: (A) Ferroelectric, (B) Antiferroelectric, (C) Paraelectric, (D) Ferrielectric and (E) Antiferrielectric states.

---

[6] The term should not be confused with ferroelastic materials, which fulfill the first mentioned condition but not the second one. In these materials the change in polarization is due to mechanical stresses.

Among the spontaneously polarized materials, the most important ones regarding their technological applications are probably the ferroelectrics, antiferroelectrics and paraelectrics.

Antiferroelectric materials are essentially polar ceramics that revert to a ferroelectric state when subjected to a sufficiently high electric field. Several perovskite materials can be found whit this property. In their case, the dipoles are formed due to an alternatively displacement in opposite senses and a preferential direction of the central cations from the six oxygen geometric centre; therefore, the net spontaneous polarization is zero.

Paraelectric materials do not present a net permanent dipole moment, but under an $\mathbf{E_0}$ they become polarized. It should be pointed out that with the removal of $\mathbf{E_0}$ the material returns to its virgin state, *i.e.* net polarization becomes zero [12] [14].

Four types of ferroelectric ceramics are given in Figure 3 as subcategories of ferroelectric materials, with typical samples representing the type based on its unit-cell structure: (1) the tungsten–bronze group, (2) the oxygen octahedral group, (3) the pyrochlore group and (4) the bismuth layer–structure group. Of these, the second group, perovskite-type (called like these because of the mineral perovskite $CaTiO_3$) is by far the most important category taking into account its techno-economical features. A perovskite unit-cell taken normally as reference, due to its high symmetry, can be seen in Figure 5 (C). This is a very large family of materials with composition ABO_3, where A and B each represent a cation element or mixture of two or more such elements or vacancies. The physical properties of the entire family are extremely diverse; depending on the composition and cationic ordering, they can be metallic or insulating and exhibit many different types of structural and magnetic/electric order.

The commonly polymorphic structures found in nature of perovskite materials are presented in Figure 5. Each structure is stable at different temperatures and pressures. In all the cases, the rhombohedral and tetragonal lattice systems are stable at temperatures below the Curie temperature (T_c)[7]. They present a spontaneous polarization and most of the times *R3C* and *P4bm* space groups, respectively. The cubic structure is stable, most of the times, at high-temperatures (above T_c), in which case represents a unit-cell of the paraelectric phase of these materials. It commonly presents a $Pm\bar{3}m$ space group, with a simple cubic lattice and a motive of 5 atoms. As

---

[7] This temperature corresponds to a phase transition of the material from its ferroelectric to its paraelectric state.

shown in Figure 5 (C), if the A atom is taken at the corner of the cube, the B atom is at the center of it and there is an oxygen at the center of each face. No displacement of the central atom can be found, this is the reason that no spontaneous polarization is present when a phase presents a cubic unit-cell.

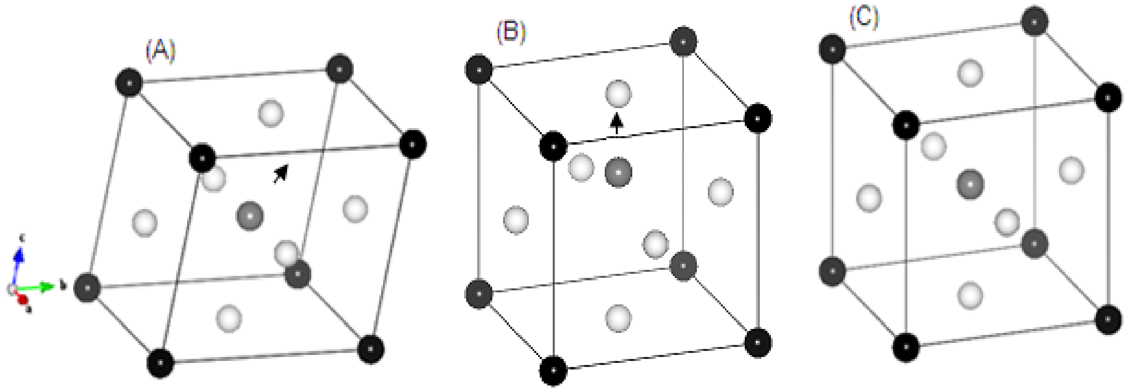

Figure 5: Normal unit-cells of perovskite structure ABO_3 materials with increasing temperature from left to right, (A) Rhombohedral, (B) Tetragonal, (C) Cubic. The high-temperature cubic perovskite structure ABO_3 is normally taken as reference. The B atom (gray) is at the center of an octahedron composed of oxygen atoms (white). The A atom (black) has 12 oxygen first neighbors. The arrows indicate the polarization direction and sense [15].

The prevalence of distortions for compounds crystallizing in the perovskite structure is related to the structural frustration of the cubic perovskite structure regarded as an ionic solid. An empirical criterion for the stability of the perfect perovskite-type structure was developed by Goldschmidt (1926), in which a tolerance factor t is defined as in Equation 16.

$$\mathrm{t} = \frac{\mathrm{r_A} + \mathrm{r_o}}{\sqrt{2}(\mathrm{r_B} + \mathrm{r_o})} \qquad \text{Equation 16,}$$

where $\mathrm{r_A}$ is the ionic radius of the A-site ions, $\mathrm{r_o}$ the ionic radius of the O ions and $\mathrm{r_B}$ the ionic radius of the B-site ions.

Goldschmidt has shown that the perovskite structure is formed when the condition expressed by Equation 16 is satisfied ($t \approx 1$). When $t > 1$, the structure is imposed by the A–O distance and the B atom is too small for the oxygen octahedron so the structure will develop a small polar distortion. Conversely, when $t < 1$, the A atom is small in comparison to the hole between the oxygen octahedral, which results in a non-effective bonding with all the 12 neighboring O atoms. If t is slightly less than one, rotations and tilting of the oxygen octahedra will be favored; for even smaller t the compound will favor a strongly distorted structure with only 6 neighbors for the A atom, *i.e.* the perovskite-type structures will be energetically unfavorable relative to another one.

The perovskite oxides readily form solid solutions, many of which show complete miscibility. The isoelectronic substitutions are particularly relevant to the study of ferroelectricity, as the formal valence counting yields insulating and dielectric behavior across the phase diagram. Moreover, the change in a cation can lead to shifts in transition temperatures as well as the appearance or disappearance of particular phases. For heterovalent substitutions on the A or B site (or both), the substitution must be in a fixed ratio in order to produce an insulating or dielectric state. The more pronounced difference between substituents, relative to the iso-valent solid solutions, produces new phenomena that can provide useful properties for technological devices. Among these can be mentioned short- and long-range ordering/disordering of the cation arrangement, relaxor-like behavior, diffuse phase transitions, among other effects [12] [13] [16].

2.2.2 Hysteresis in ferroelectric materials

Within a domain, all the electric dipoles are aligned in the same direction; nevertheless, it is feasible that an $\mathbf{E_0}$ could lead to the polarization reorientation within a domain (*i.e.* domain switching). The changes in the direction of polarization require small ionic movements in specific crystallographic directions. It follows that the greater the number of possible directions the more closely the polar axes of the crystallite in a ceramic can be brought to the direction of the poling field. The tetragonal structure allows six directions, while the rhombohedral allows eight and so this structure permits greater alignment. If both tetragonal and rhombohedral phases are present at a transition point, where they can be transformed by a field, the number of alternative crystallographic directions rises to fourteen. This phase transition is often called morphotropic phase boundary (MPB). Although, in principle, any phase boundary where a structural change occurs with a compositional modification may be labeled MPB, the term is confined in the ferroelectric materials context to a phenomenon where a structural change leads to an increase in the multiplicity of polarization states; therefore, it potentially contributes to enhance electromechanical properties. The polarization reversal can be observed by measuring the ferroelectric hysteresis (Figure 6).

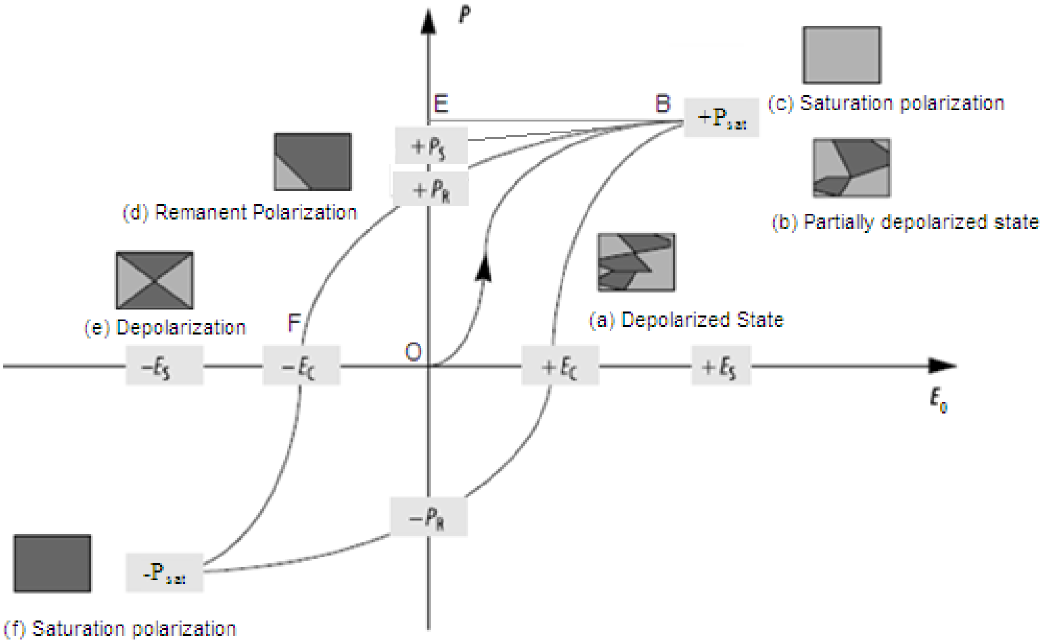

Figure 6: Polarization vs. external electric field hysteresis loop for a typical ferroelectric material [10].

As the electric field strength is increased, the domains start to align in the positive direction giving rise to a rapid increase in **P** (OB), which results in a saturation value (+P_{sat}) of magnitude OE (Figure 6 a-c). At zero $\mathbf{E_0}$, some of the domains remain aligned in the positive direction, hence the crystal will show a remanent polarization $\mathbf{P_r}$ (Figure 6 d). The crystal cannot be completely depolarized until a field of magnitude OF, called coercive field $\mathbf{E_c}$, is applied in the negative sense. If the field is increased to a more negative value, the direction of **P** flips and hence a hysteresis loop is obtained (Figure 6 d-f). Further cycles of the electric field retrace the original path, creating a continuous hysteresis effect. If this behavior is low, the material will be called soft. This indicates that the polarization switching will require a low $\mathbf{E_0}$. The spontaneous polarization ($\mathbf{P_s}$) can be obtained in any of the cycles by extrapolating the polarization at +P_{sat} back to zero along a tangent.

The ferroelectric hysteresis loop varies in shape with temperature. At lower temperatures there is less thermal motion of atoms and a greater field is required to orient the domains. At higher temperatures the coercive electric field required for polarization decreases, until at T_c the hysteresis disappears and linearity is approximated in a paraelectric state. Typical hysteresis loop schemes for (A) Paraelectric and (B) Antiferroelectric materials can be seen in Figure 7.

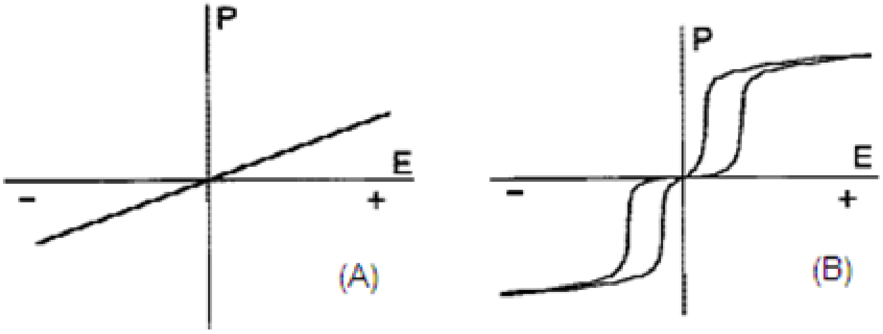

Figure 7: Typical hysteresis loops for (A) Paraelectric (B) Antiferroelectric material [13].

Note that in an antiferroelectric material, the hysteresis behavior is also observed but with a typical pinched hysteresis loop (Figure 7(B)) [13].

Most of the materials used in technological applications are polycrystalline. In an initial state, these materials possess isotropic characteristics due to the randomly oriented crystallites. In order to obtain materials capable of piezoelectric, pyroelectric and electro-optic behavior anisotropic materials should be developed. In other words, a process of aligning domains (*i.e.* polar axis) in preferred orientations of the crystallites should be done to obtain the desired properties. This process is called poling and consists in the application of an electric field under appropriate conditions of temperature and time. It should also be taken into account that the original random orientation of the domains (virgin condition) will be restored if the material is heated above its T_c. This process is called thermal depoling [12] [14] [17].

2.2.3 Ferroelectric classification

The ferroelectric materials can be divided into three different categories: (1) Normal ferroelectrics, (2) Ferroelectrics with a diffuse phase transition and (3) Relaxor materials.

The normal ferroelectrics present an abrupt anomaly in their ε_r and a sharp or progressing vanishing polarization related to a proper first order or second order phase transition from the ferroelectric to the paraelectric state at T_c. This behavior can be seen in Figure 8.

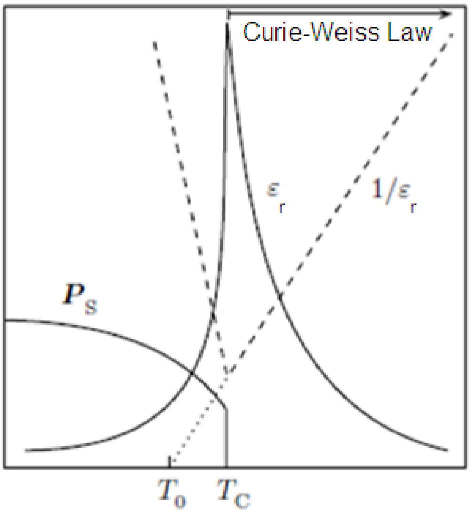

Figure 8: Schematic temperature dependence of ε_r and P_s of normal ferroelectrics. At T_c a first-order phase transition from the paraelectric to the ferroelectric state occurs. If T_c=T_0, at which the inverse of relative permittivity approaches zero when T reaches T_c from above, the phase transition is second-order [18].

In the paraelectric state the ε_r follows the Curie-Weiss law:

$$\varepsilon_r = \frac{C}{T - T_0} \qquad \text{Equation 17,}$$

where C is the Curie constant of the material and T_0 is a critical temperature defined as the temperature corresponding to the inverse of the ε_r when $\varepsilon_r \to \infty$. The phase transition from paraelectric to the ferroelectric state is usually first order. However, if T_c coincides with T_0, a second-order phase transition occurs.

The ferroelectrics with a diffuse phase transition (second category) are characterized by an improper phase transition, which results in a discontinuous variation of the ε_r with a limited step. This diffuse phase transition usually occurs in the iso-valent or off-valent substitutional solid solutions, where different kinds of ions occupy a crystallographically equivalent site, resulting in a broadening of the dielectric peak and hence diffuseness of the phase transition.

The relaxor materials (third category) exhibit a broad maximum and a significant frequency dispersion of the ε_r, with the temperature of the ε_r maxima (which corresponds to the temperature often called T_m) increasing and its magnitude decreasing with increasing frequency (Figure 9). The former behavior is reminiscent of a “diffuse ferroelectric phase transition” and the latter of a dielectric relaxation. This maximum is also associated with a maximum in tan(δ) and a thermal hysteresis upon heating and cooling. Moreover, it does not mark a phase change into a ferroelectric form (not even a diffuse one). In this context, it should be mentioned that local nanopolar regions nucleate in the material at high-temperatures far above T_m. It is believed that these nanopolar regions increase their volume fraction and size when temperatures are decreased, thus their dynamical response to $\mathbf{E_0}$ may carry a major fraction of the system polarizability. This implies that their dynamics (slowing down) must tie in closely with the massive dielectric relaxation near T_m (this process may be labeled thermal evolution of the nanopolar regions) (Figure 9). In some poled materials, upon further cooling below this temperature, a spontaneous (zero-field) phase transition takes place from the relaxor regime into a ferroelectric state. This is usually associated with another anomaly in ε_r. The temperature corresponding to this transition is sometimes called depolarization temperature (T_d). In relaxor-like materials the transition of ε_r at T_m does not follow the Curie-Weiss law, but a modified one:

$$\varepsilon_r = \frac{C}{(T - T_0)^{\gamma}} \qquad \text{Equation 18,}$$

where γ is an exponent between 1 and 2 which represents the relaxor-like behavior of a material. The lower extreme represents a normal ferroelectric and the upper one a relaxor.

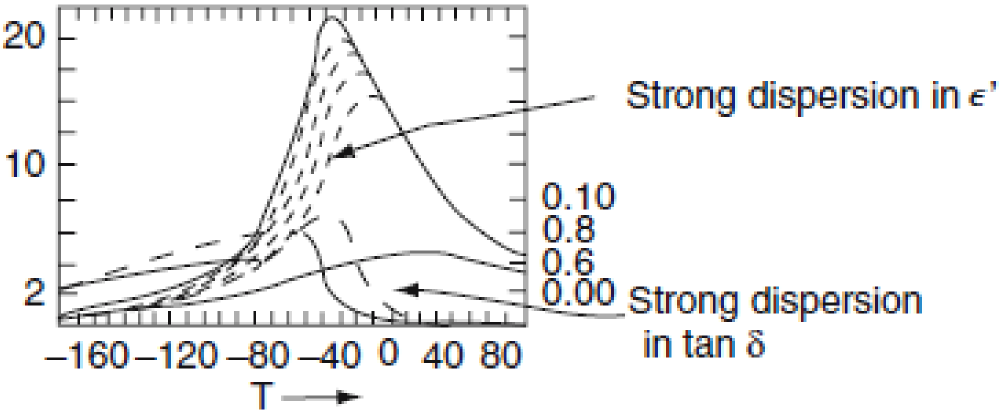

Figure 9: Dielectric dispersion in $Pb(Mg_{1/3}Nb_{2/3})O_3$ (typical relaxor) as a function of temperature and frequency [19].

Another common characteristic in relaxor materials is that the hysteretic response slowly degenerates into just nonlinearity as the temperature increases, *i.e.* the spontaneous polarization is not suddenly lost at the T_c but it rather decays more gradually to zero (Figure 10).

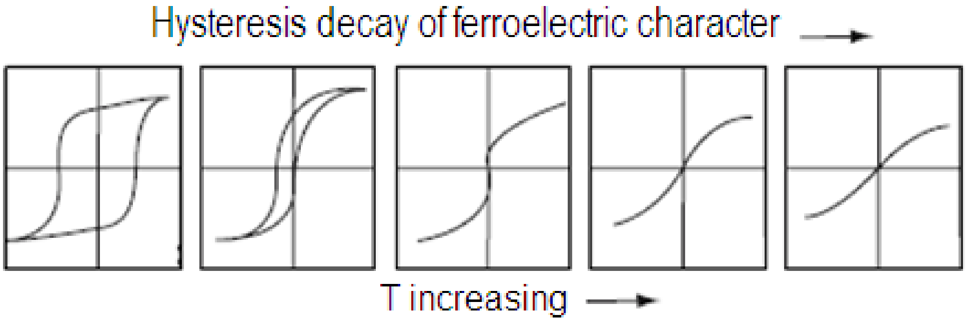

Figure 10: Decay in the hysteresis loop with increasing temperature [19].

The most startling behavior of a relaxor material is that samples even at very low-temperature show no evidence of optical anisotropy or X-ray line splitting, which would be characteristic of a macro-volume changing to a polar phase (Figure 11). The explanation to this behavior is the presence of the mentioned nanopolar regions in the material [19-21].

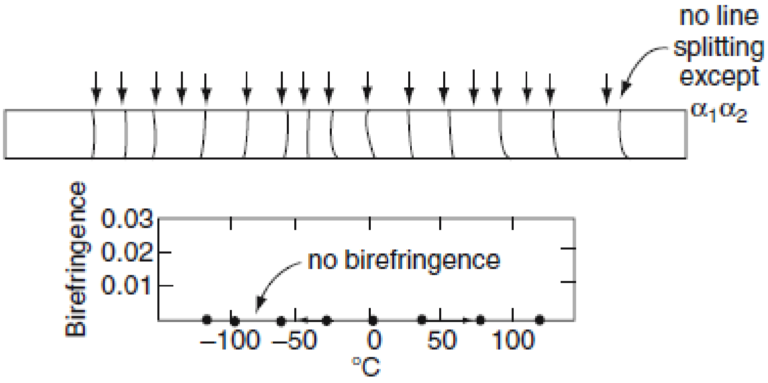

Figure 11: Optical and X-ray evidence for the absence of a macroscopic phase change below the T_c [19].

The commonly observed hysteresis strain loops when (A) Normal and (B) Relaxor-like ferroelectric materials are subjected to an $\mathbf{E_0}$ are given in Figure 12. In the normal ferroelectrics, the switching strain accompanying the polarization reversal process results in the familiar “butterfly” loop, with the remanent strain state in the center of the loop. Positive voltage results in a longitudinal expansion of the ceramic, whereas a negative voltage (less than the coercive field) results in a longitudinal contraction, *i.e.* the strain developed is due to the piezoelectric effect mentioned previously. For the relaxor-like ferroelectrics, there is no remanent strain when the electric field is not applied. This is a consequence of the rest position of the central ion in the unit-cell, which corresponds to the unit-cell geometrical center. However, when the field is applied, ionic movement (polarization) and strain occur simultaneously, both being dependent upon the strength of the field. Because the sense of the strain produced is the same regardless the polarity of the field, this is the electrostrictive effect mentioned previously [13] [19].

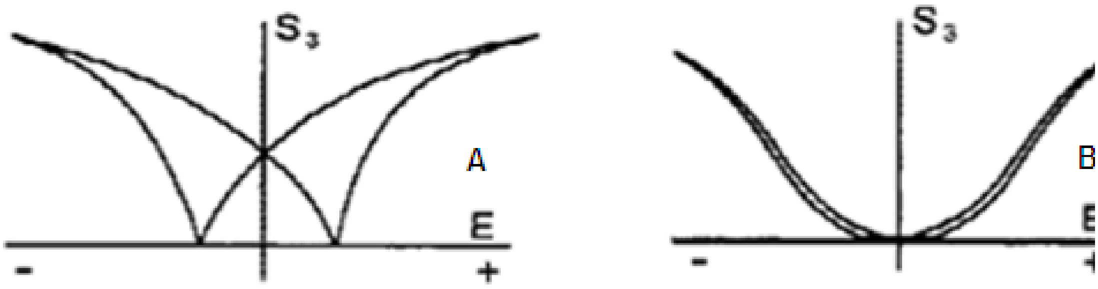

Figure 12: Longitudinal strain curves for (A) Ferroelectric and (B) Relaxor materials [13].

3 Literature review

3.1 High-temperature dielectric materials

3.1.1 High-temperature dielectric materials requirements

Dielectric materials have to fulfill many properties regarding their dielectric behavior and this is the main reason why the development of high-temperature dielectrics is a challenging area. Among these properties, the following requirements can be mentioned:

1. A high ε_r. This property should be as high as possible because it allows large value capacitors with proper volumetric efficiency and hence permits system miniaturization. This has an important constraint since material formulations for capacitors are chosen near their MPB resulting in a high ε_r but also a high-temperature dependence of it.
2. The material resistivity should be as high as possible even at elevated temperatures (beyond 200 ºC), mainly because if the material becomes a conductor its role as capacitor is vanished.
3. A high resistance-capacitance (RC) constant, which indicates a high charging and discharging response time τ[8]. This property is often considered as the insulation resistance of a capacitor, *i.e.* it is another way of expressing that the dielectric material would not become conductor at high-temperatures.
4. The tan(δ) should be kept as low as possible, since it is proportional to the heat dissipation. If heating is too high, this can produce the breakdown of the capacitor or the circuit.

Moreover it should be mentioned that these characteristics should remain as constant as possible in a large temperature and frequency range to allow a reliable service of the capacitor.

It should also be taken into account that a capacitor is a massive application, thus a minimized cost/product ratio has a major importance. In other words, the raw

---

[8] τ = RC is the time required to charge the capacitor to ~63.2%, or in analogy discharge it to ~38.2%.

materials and manufacturing processing choice should be as inexpensive as possible. The cost of the different suitable chemical elements can be seen in Figure 13.

During the last years, an increased awareness for environmental issues has spurred considerable efforts to reduce the amount of hazardous substances in consumer products. Most of the commercial available dielectric materials used as capacitors are ferroelectric materials. Among them, most are lead containing; this results in a severe design constraint due to the toxicity and hazard of this element. Moreover, the amount of electronic component waste generated all around the world is growing rapidly and their disposal areas are a major concern. For these reasons new initiatives and laws are promulgated regarding the prohibition of toxic elements and promoting electrical waste disposals around the world [22-32]. Nevertheless, it should be noted that lead is not the only element that should be avoided in the development of new non-contaminant dielectric materials (Figure 13).

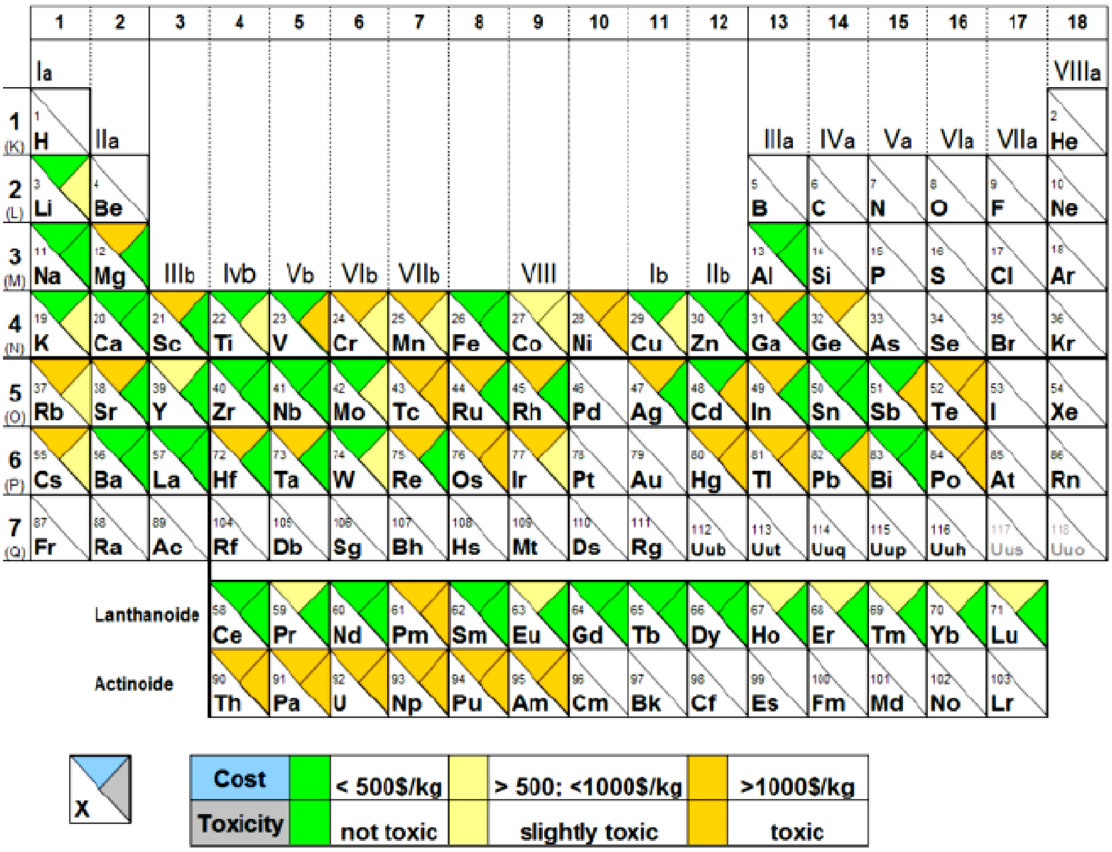

Figure 13: Periodic table showing relative cost and toxicity of the elements of interest in ferroelectric materials [32].

The present work focuses on the development of dielectric ceramics. In this context, it should be mentioned that a four group classification exists for these materials. Class I materials present the least variable temperature, voltage and frequency properties; however, they present the lowest levels of volumetric efficiency. On the other hand, class IV materials have the highest volumetric efficiency, but present highly variable dielectric properties.

Class II materials are ceramic dielectrics with non-linear predictable temperature and frequency dependence on their ε_r and capacity. Materials of this group would be developed in the present work. For this reason it is convenient to present the international nomenclature often used to classify them. The classification is made by two letters and a number indicating the minimum working temperature, change permitted in capacitance and maximum temperature of the dielectric material, respectively (*i.e.* a common dielectric ceramic used for high-temperatures is a X7R) [10] [33]. This information can be seen in Table 1.

Minimum temperature		**Maximum temperature**		**Capacitance change permitted**	
X	-55 °C	**4**	+65 °C	**A**	±1.0%
Y	-30 °C	**5**	+85 °C	**B**	±1.5%
Z	+10 °C	**6**	+105 °C	**C**	±2.2%
		7	+125 °C	**D**	±3.3%
		8	+150 °C	**E**	±4.7%
		9	+200 °C	**F**	±7.5%
				P	±10%
				R	±15%
				S	±22%
				T	22% / -33%
				U	22% / -56%
				V	22% / -82%

Table 1: Class II dielectric materials classification [33].

Note that till these days it does not exist yet a proper nomenclature for dielectrics materials working at temperatures beyond 200 ºC [33].

3.1.2 Current status in the development of high-temperature dielectrics

Several polymer, composite and ceramic materials that present suitable properties for high-temperature capacitors can be found in literature [2] [34] [35]. Nevertheless, most of these materials present suitable properties in a narrow temperature range either at moderate or high-temperatures. Therefore, it can be said that to the date there is no material that fulfils all the application requirements mentioned (Section 3.1.1).

Polymers are used as dielectric materials because of their low tan(δ) and high breakdown strengths. In high-temperature applications the polymers with a high glass transition temperature (T_g) and high thermal stability are the best candidates. Nevertheless, their inherently low ε_r (*i.e.* their low volumetric efficiency) and limited service temperature compared to that in ceramic materials are clear disadvantages for high-temperature capacitors. Venkat *et al.* [35] reported the synthesis of high-temperature dielectric materials based on metallized films derived from polymer materials such as fluorinated polybenzoxazoles (FP), fluorinated polyimide with adamantyl ester pendant (FP-E) and fluorenyl polyester with 4,9-diamantyl group (FP-D). The FP showed an almost linear increment dependence with temperature and frequency in the film ε_r. The changes were around 2-3% at 250 ºC and 1 MHz compared to that at room temperature and 1 kHz, respectively. Moreover, the tan(δ) was below 2% in the temperature range mentioned. The FP-E showed similar values and dependence in ε_r with temperature and frequency; however, it presented a tan(δ) below 1% in the same temperature range. The FP-D showed a variation below 2% in its ε_r for a frequency range from 1 kHz to 1 MHz and a range from room temperature to 350 ºC. Moreover, the average ε_r was around 3.5 and the tan(δ) was below 0.3% for the same temperature range [35]. The fluorene polyester (FPy) is also an attractive material for high-temperature applications due to its high T_g (T_g ~ 330°C). Moreover, it presents a low tan(δ) and a stable ε_r over a wide frequency (up to 1 MHz) and temperature (up to 250 ºC) ranges. For instance, Stricker *et al.* [36] reported the development and evaluation of wound capacitors made of FPy metallized films that were able to work properly in a temperature range from 0 to 200 ºC [36]. Saarinen *et al.* [37] reported capacitors made of polyethylene naphthalate and polyphenylene sulphide. Both materials are abundant in today's market and present high melting points of 266 and 285 ºC, respectively. These materials presented an average ε_r around 3 with a tan(δ) below 0.4% at 1 kHz. Taking into account these characteristics, the materials reported by Saarinen *et al.* [37] can be used as high-temperature dielectrics in applications with service temperatures around 175 ºC.

Composite materials with a polymer based matrix and ceramic fibers can also present suitable properties for high-temperature dielectrics. Akram *et al.* [38] studied the dielectric properties of different polyester resin matrix composites with different types of glass fibers: E, C and S-type fibers. Pure polyester resin samples and with 50 vol. % of the different glass fiber mentioned were prepared by a compression molding process. The highest ε_r was measured in the sample with C-glass fibers which presented an average value below 50. Moreover, it was observed that ε_r increased with increasing temperature from 30 to 150 ºC and this behavior was more prominent at lower frequencies. In all the cases, the tan(δ) was below 15% with increasing average values at lower frequencies [38]. Dang *et al.* [39] reported a film polymer matrix composite with nanohybrid fillers. Polyimide was chosen as matrix due to its high-temperature durability, good mechanical and insulation properties in a wide temperature range. As filler $BaTiO_3$ particles with an average size of 100 nm in different concentrations were used. It was observed that the samples with 40 vol. % $BaTiO_3$ particles presented the higher ε_r with an average value around 17. Moreover, this material presented a low dependence of its ε_r with temperature and frequency. Therefore, it presented a variation in its capacity within 15% in the temperature range from -50 to 150 ºC [39].

Du *et al.* [40] developed glass-ceramic composites in the Na_2O-PbO-Nb_2O_5-SiO_2 system. They produced bulk materials with nanometer-sized crystals grown in a glass phase via roll-quenching followed by controlled crystallization. The ε_r of the as-quenched glass was around 40 at room temperature. Upon further heat treatment, the ε_r was increased as a result of the formation of crystalline phases with high ε_r within the glass. The ε_r was continuously improved with increasing crystallization up to a heat treatment of 850 ºC, temperature at which the highest ε_r was achieved. Its average value was between 600 and 700 in a temperature range from -25 to 150 ºC. For this temperature range it also presented a low tan(δ) around 4%. The increased dielectric properties observed in the sample heat-treated at 850 ºC were attributed to the presence of an optimum amount of $NaNbO_3$ and $PbNb_2O_6$ phases and/or their solid solutions [40]. Mao *et al.* [41] studied other glass-ceramic composites in the Nb_2O_5-BaO-Na_2O-SiO_2 system. The initial ε_r of the as-quenched glass was around 30 at room temperature. With an increasing crystallization temperature, the ε_r increased with the formation of crystalline phases. The higher ε_r was observed for the sample heat-treated at 900 ºC, which presented an average value of around 170. Moreover, for all the samples a variation within 10% in their ε_r was observed for the temperature range from -50 to 150 ºC and frequency from 100 Hz to 100 kHz [41].

Ceramic materials can be used as high-temperature dielectrics in either their amorphous or crystalline structures. Jamison *et al.* [34] studied amorphous films of SiO_2. These films presented an average ε_r of 4.9, which was almost independent of temperature in the range from room temperature to 350 ºC. Moreover, the ε_r was also almost independent of frequency in the range from 100 kHz to 1MHz. The tan(δ) presented an average value of 0.2% from room temperature to 200 ºC and was also almost independent of temperature in this range. However, an increase in tan(δ) was observed for higher temperatures reaching a value of almost 1.4% at 350 ºC [34]. In this context, it should be mentioned that Jamison *et al.* [42] developed a United States patent which describes high-temperature capacitors based on the amorphous SiO_2 films described. Bray *et al*. [43] developed multilayer capacitors based on amorphous AlN films that could work in a wide temperature range from -200 to 300 ºC with an almost constant capacitance. Nevertheless, the capacitors developed presented low average capacity values of less than 2 nF [43]. Kamel *et al.* [44] studied amorphous $BaTiO_3$ thin films. It was observed that the ε_r and tan(δ) increased with temperature and decreased with frequency. For a 100 kHz frequency an average ε_r of 20 was observed for the temperature range from -100 to 225 ºC [44].

Many of the ceramic compounds commonly found cannot be obtained with amorphous structures as bulk materials. In some other cases to obtain them demands a complex processing. For these reasons, many investigations focus on crystalline ceramic materials. Among the crystalline ceramic materials, the $BaTiO_3$ (BT) is by far the most commonly used material as dielectric. For instance, this can be seen in the high amount of patents published on high-temperature dielectric materials based on modified BT [45-48]. Yuan *et al.* [49] studied the BT- $0.05Bi_{0.5}Na_{0.5}TiO_3$ (BNT) system doped with $BiNbO_4$ (BN) and the BT-BNT-BN system doped with Nb_2O_5. A core-shell structure with chemical inhomogeneity was formed which was attributed to the low diffusion rate of the Nb^{5+} ions. It was observed that the ε_r presented two anomalies. The one at high-temperature was attributed to the ferroelectric-paraelectric phase transition of the cores, while the one at low-temperature was attributed to that of the shells. The sample with 3 mol % BN presented a ε_r variation within 15% of variation in the temperature range from -55 to 150 ºC. Nevertheless, in temperatures above 150 ºC the ε_r was decreased significantly. For the 4 mol % Nb_2O_5 a dielectric material with a working temperature range from -55 to 200 ºC within 15% variation in its capacitance was developed. Nevertheless, for temperatures beyond 200 ºC the capacitance decreased significantly [49]. In another study, Yuan *et al.* [50] investigated the BT doped with different concentrations of BNT, ZnO and $CaZrO_3$ (CZ). It was observed that the ε_r decreased over a wide temperature range with increasing BNT content. Moreover, the ε_r peak at T_c was markedly suppressed and broadened. On the other hand, the overall ε_r was enhanced gradually with increasing ZnO concentration. This was attributed to the increased density and grain size in the samples. For the samples doped with 7 and 8 mol % CZ, dielectric materials with a temperature range from -55 to 175 ºC within 15% of variation in its capacitance were achieved. It was observed that with increasing CZ content, an overall decrease of the ε_r was obtained. Moreover, this decrease was enhanced for the ε_r peak at T_c, *i.e.* the ε_r curves became flattened with increasing CZ content [50]. The addition of 3 and 6 mol % CZ in the BT-0.025Yb_2O_3-0.07MnO_2 and BT-0.025Yb_2O_3-0.07NiO systems was also studied by Zhang *et al.* [51]. For the system with MnO_2 an overall decrease in the ε_r was observed. However, for the system with the presence of NiO the ε_r was increased below room temperature with increasing CZ amount. Nevertheless, in both systems a flattened ε_r resulted when CZ content was increased, *i.e.* the ε_r peak at T_c was significantly decreased. This result was similar as in the previous study. All the samples developed in this study presented a core-shell structure, which was attributed to the presence of the Mn and Ni ions that could suppress the diffusion of Yb and CZ into the BT grains. It was also observed that the addition of CZ decreased the core/shell volume ratio. The authors attributed the mentioned flattened ε_r to this phenomenon. It should be highlighted that all the compositions mentioned above presented suitable properties for high-temperature dielectrics with working temperature ranges from -55 to 150 ºC within 15% of variation in their capacity [51]. In this context, it should be mentioned that other BT-based materials with core-shell structures and second phases have suitable dielectric properties for high-temperature applications [52-56]. One disadvantage that can be observed in all the BT-based systems reported is that their working temperature range is below 200 ºC. This can be attributed to the low T_c of the BT (Section 2.3.4 for further details). For this reason, other studies can be found in literature regarding high-temperature dielectrics in crystalline ceramics. Lim *et al.* [57] showed that the $BiScO_3$-BT-$K_{0.5}Bi_{0.5}TiO_3$

exhibits good electrical properties over a wide temperature range [57]. Other scientists also proposed similar materials with the presence of Sc as high-temperature dielectrics [58] [59]. Nevertheless, those systems incorporate the expensive element Sc, which limit the systems to academic research. High-temperature dielectrics had been also reported in lead-containing systems [60] [61]. Nevertheless, taking into account the toxicity of this element it is not convenient to develop lead-based or lead-doped high-temperature dielectrics. Yuan *et al.* [62] developed high-temperature dielectric materials in BNT-based systems. The (1-x-y) BNT-xBT-y$CaTiO_3$ system presented suitable properties in the temperature range from -55 to 150 ºC within 15% of variation in its capacitance. Nevertheless, for temperatures outside the mentioned range the dielectric properties decreased significantly [62]. Bridger *et al.* [64] showed that the 0.9BNT-0.1$KTaO_3$ system exhibits a relatively flat ε_r from 80 to 260 °C, though the ε_r outside this range rapidly decreases. On the other hand, Dittmer *et al.* [2] developed a promising dielectric material with a high-temperature operational range. Nevertheless, this material was not able to work properly below room temperature [2]. Wang *et al.* [65] studied the pure $K_{0.5}Na_{0.5}NbO_3$ (KNN) compound and the 0.995[0.06($K_{0.5}Na_{0.5}$)0.94$Li_{0.06}$]NbO_3 (KNLN)-0.005AETiO_3 (AE=Ca, Sr, Mg, Ba) systems. It was observed that ε_r for the pure KNN samples showed two different anomalies, which were attributed to the T_c and the orthorhombic-tetragonal phase transition of the material, respectively. The T_c of the ceramics was shifted to lower temperatures with the addition of Li, Ba, Sr and Mg. However, it was found that the T_c of the KNLN-$CaTiO_3$ ceramics was shifted to higher ones. Moreover, it was found that all the dopants shifted the orthorhombic-tetragonal phase transition to lower temperatures significantly. In the case of the sample doped with $CaTiO_3$, a significant increase in the density was also observed and an almost constant ε_r in the temperature range from room temperature to 350 ºC was achieved. Nevertheless, for higher temperatures a significant ε_r anomaly was observed [65]. Tang *et al.* [66] studied the influence of Nb and $Zn_{0.8}Mg_{0.2}TiO_3$ (ZMT) in the BT-Nb_2O_5 system. It was observed that the system presented secondary phases when the addition of Nb or ZMT exceeded the 1 and 2 mol %, respectively. For the compositions with 1 mol % Nb and 2 to 4 mol % ZMT, as well as for the composition with 1 mol % ZMT and 2 to 4 mol % Nb, a decrease in ε_r peak at T_c was observed. This resulted in high-temperature dielectrics with a working temperature range from -55 to 150 ºC within 15% of variation in their ε_r. Moreover, increasing the Nb content resulted in a core-shell structure [66]. Bridger *et* *al.* [67] [68] successfully developed high-temperature dielectrics in BNT-based materials with working temperature ranges from -55 to 200 ºC and with high-temperature operational windows within 15% of variation in their ε_r. Nevertheless, a wide operational range from low to high-temperatures (beyond 300 ºC) was not achieved in any of the materials developed [67] [68].

Taking into account all the presented high-temperature materials, the BNT-based ones were chosen as starting materials to develop new non-contaminant high-temperature dielectrics with wide operational range. Moreover, it was decided that the best procedure to obtain a wide temperature operational range and proper dielectric properties was by doping. The CZ was chosen as a dopant due to the characteristic of each of the chemical elements. Calcium is a known T_m shifter and a ferroelectric depressor [62], while zirconium acts also as a ferroelectric depressor and shifts mainly the anomaly at T_d [63]. Therefore, both elements together are expected to flatten the ε_r in a wide temperature range. For these reasons the systems studied in the present work were decided to be $(1–x)(0.94Bi_{0.5}Na_{0.5}TiO_3\text{-}0.06BaTiO_3)\text{-}xCaZrO_3$ and $(1–x)(0.82(0.94Bi_{0.5}Na_{0.5}TiO_3\text{-}0.06BaTiO_3)\text{-}0.18K_{0.5}Na_{0.5}NbO_3)\text{-}xCaZrO_3$, with x=0, 0.05, 0.1 and 0.2. It should also be highlighted that in future investigations the role of sintering temperature and atmosphere, grain size, density and second phases should be analyzed for major properties improvement.

3.1.3 $Bi_{0.5}Na_{0.5}TiO_3$

The BNT system is one of the important lead-free piezoelectric materials with perovskite structure discovered by Smolenskii *et al.* [69] in 1960. The Bi^{3+} ion is an excellent candidate for the substitution of Pb^{2+} in perovskite oxides due to the similar ‘inert-pair’ $6s^2$ electronic configuration. For instance, BNT presents a remanent polarization $P_r = 38\ \mu C/cm^2$, a coercive field $E_c = 7.3$ kV/mm and high T_c= 320 ºC [70-72]. Taking into account these properties, this compound has been considered a good candidate for lead-free piezoelectric ceramics. Moreover, it also reveals a very interesting ε_r anomaly that, together with its high T_c, can be useful for high-temperature applications. Another interesting characteristics is that many Bi-containing perovskite materials present high T_c, such as $BiFeO_3$ (>800 ◦C), $BiScO_3$ (∼450 ◦C), among others. Therefore, not only BNT, but also BNT-based materials are inspiring for high-temperature dielectrics [73-75]. Nevertheless, it should be mentioned that one important drawback of this material in this application is its high conductivity. This creates also an extra difficulty for the poling process [76].

Jones *et al.* [77] studied the BNT via neutron scattering and the Rietveld profile fitting method. From 5-593 K the phase observed was rhombohedral. This phase was described with a *R3c* space group, with $(a^-a^-a^-)$ antiphase tilt rotations (ω) (Glazer Notation [78]) of the TiO_6 octahedra about the pseudo-cubic axes, which resulted in the doubling of the unit-cell axes (Figure 14). This octahedral tilting was presumed to be driven by the need to optimize the anion coordination about the A cation since Bi^{3+} and Na^+ are relatively small cations for A-sites. Moreover, A (Na/Bi)- and B (Ti)-cation displacements were observed in the same sense and result parallel to the [111] direction (the shifts of the O atoms were also noted in the same direction). These displacements resulted from a need to achieve electrostatic energy minimization associated with the tilting octahedra and also are presumably driven (to a differing extent) by the need to accommodate the stereoactive lone pair on Bi^{3+}. The Na and Bi positions were allowed to refine separately, this resulted in a Bi displacement of 0,003 Å along the polar axis (c^+) with respect to Na and thus a polar ferroelectric phase. The mentioned structure can be seen in Figure 14.

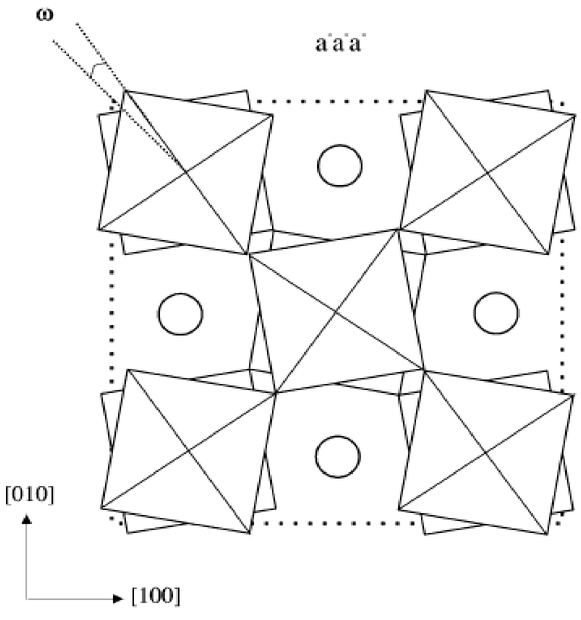

Figure 14: The projection of the rhombohedral structure down [001]; open circles represent Na/Bi sites [77].

The coexistence of rhombohedral and tetragonal phases was indicated by the presence of superstructure reflections in the temperature range 573-593K. Rhombohedral superstructure reflections diminish as the tetragonal ones appeared with increasing temperature.

The region from 673-773K showed a pure tetragonal phase (note that the temperature range from 593-673 K was not analyzed). It presented a *P4bm* space group, which can be described as a distorted phase from the high-temperature cubic one. Contrary to the rhombohedral phase, Na/Bi and Ti atoms were displaced in opposite senses along the polar [001] direction (c axis), combined with in-phase ($a^0a^0c^+$) tilts of oxygen octahedral TiO_6 about the same direction [79]. This resulted in cell doubling of the [100] and [010] directions. Thus an indistinguishable environment for the A cation when viewed (from the cation) along the c^+ and c^- senses was obtained. Therefore, from the geometry of the framework alone, there was no incentive for the A cation to move off-centre. Since A cation displacement along [001] was not driven by the octahedral tilts, the conclusion was that it resulted from the need to accommodate the stereoactive lone pair in the Bi^{3+} ions. It should be noted, however, that Bi^{3+} and Ti^{4+} were displaced in opposite senses along the c^+ direction and thus establish an almost non-polar arrangement in the unit-cell. Therefore, although the freedom of the polar space group *P4bm*, the tetragonal structure was found to be weakly polar (*i.e.* ferrielectric). On the other hand, Suchanicz *et al.* [80] believed that this was a non-polar phase, but with the presence of rhombohedral nanopolar regions (*i.e.* similar to a relaxor-like material).

The coexistence of tetragonal and cubic phases was observed between 773-813K. As the temperature was increased in the region mentioned, the distorted structure progressively gave rise to an ideal prototype cubic perovskite structure by octahedral tilting. This resulted in a zero octahedral tilt angle and no cation displacements as the cubic phase appeared. For further increase in temperature the octahedra were no longer rotated. This high-temperature paraelectric phase had a $Pm\bar{3}m$ space group and showed no evidence of cation ordering either from the neutron data or powder X-ray, *i.e.* Na/Bi cations distributed at sites randomly at temperatures of 813 K or higher [77].

Some authors argued that the ε_r anomaly at T_d in BNT is due to a low-temperature phase transition from ferroelectric to antiferroelectric [81] [82]. Nevertheless, Jones *et al.* [77] observed no superstructure peaks associated with long antiferroelectric cation ordering either in X-ray or neutron experiments. Note that from the point of view of differing size mechanisms, as the ionic radii difference in BNT is close to zero and the $(Na/Bi)O_{12}$ cuboctahedra are approximately the same size, no long-range ordering would be expected. However, the possibility that short range polar ion order exists (*i.e.* nanopolar regions) still remains [77]. Kreisel *et al.* [83] performed Raman spectroscopy in this material and observed a weak diffuse scattering in Raman spectroscopy, which was attributed to Na/Bi nanopolar regions, in agreement with Suchanicz *et al.* [80].

Zuo *et al.* [84] studied the effect of Nb^{5+} doping on the electrical properties of BNT, specifically the $(Bi_{0.5}Na_{0.5})_{1-x/2}(Ti_{1-x}Nb_x)O_3$ was studied. It was revealed that the solubility limit of this ion in the perovskite structure is 3 mol %. In solid solution it was observed that it helped to increase the resistivity and sinterability. Moreover, it acted (in solid solution or at higher concentrations) as a repressor flattening the ε_r, thus giving promising properties for high-temperature dielectric materials. With an addition of 20 mol % of Nb an almost constant ε_r with an average value of 700 was achieved in the temperature range from room temperature to 400 ºC. Moreover, an average tan(δ) below 15% was also obtained for the same temperature range. The authors attributed these results to the creation of A-site vacancies due to the donor character of the Nb ions [84].

Yuan *et al.* [85] developed high-temperature dielectrics in the BNT-$CaTiO_3$ system doped with Mn^{2+}. In all the samples a TiO_2 second phase was found due to Na and Bi evaporation during processing which lead to Ti segregation in grain boundaries. They observed that as the amount of $CaTiO_3$ increased, the ε_r at higher temperatures was decreased significantly. Nevertheless, at lower temperatures the tendency was inverse and the ε_r was clearly enhanced with more than 8 mol % $CaTiO_3$. Therefore, increasing the Ca content resulted in a flattened ε_r and shifted the T_d to lower temperatures for all the samples. These phenomena implied that that this element decreased the polarization of the BNT (*i.e.* it weakened its dielectricity). Due to ionic radii, it was assumed that the Ca^{2+} would dissolve preferentially in the A-sites replacing partially the Bi ions. As Ca^{2+} polarizability is lower than that of the Bi^{3+}, this would explain the weakened dielectricity of the system with Ca incorporation. This phenomenon was confirmed by ferroelectric hysteresis measurements, which showed an almost paraelectric state with 14 mol % of $CaTiO_3$. When Mn^{2+} was added, an increase in resistivity and a decrease in the tan(δ) was observed. Moreover, for the composition with 12 mol % of $CaTiO_3$ and 1.5 wt % of Mn^{2+}, a dielectric material with an average ε_r of around 900 within 15% of variation in the temperature range from -55 to 250 ºC was achieved. Nevertheless, as mentioned previously it should be highlighted that Mn is an expensive and toxic element that should be avoided in further developments [32] [85].

Hiruma *et al.* [86] studied the phase transition temperatures of BNT A-site doped samples with divalent (Ca^{2+}, Sr^{2+} and Ba^{2+}) and trivalent (La^{3+}, Nd^{3+}, Ho^{3+} and Yb^{3+}) ions. They used piezoelectric and dielectric temperature dependent measurements in order to observe variations in T_d and T_m. For the divalent ions, it was found that when the ionic radius is larger than that of ($Bi_{0.5}Na_{0.5}$) such as in the cases of Sr^{2+} and Ba^{2+} ions, T_m decreased with increasing doping. It was also found that T_d presented a dependence with doping, but only for compositions doped with less than 3 mol %. In this case the T_d increased with increasing doping. In this context, it is important to highlight that a significant decrease of both T_d and T_m was observed for the compositions with more than 5 mol % of Ba^{2+} ions. The Ca^{2+} had a similar effect on T_d; however, with increasing amount of this element a significantly increased T_m was observed. For the trivalent ions, it was observed that T_m increased with increasing doping and with decreasing ionic radii. On the other hand, it was found that T_d decreased with increasing doping and decreasing ionic radii. A manipulation of T_d and/or T_m could lead to a flattened ε_r; therefore, these results can be used to adjust the dielectric properties of different systems [86].

3.1.4 $BaTiO_3$

BT was the first piezoelectric transducer ceramic ever developed; however, its use in recent years has shifted away from transducers to an almost exclusive use as high ε_r dielectric materials used in capacitors of discrete and multilayer types. The reasons for this are primarily twofold: (1) its relatively low T_c of 120 °C, which limits its use as high-power transducer and also limits its application in wide temperature range applications; (2) its low electromechanical coupling factor in comparison to lead containing materials, which limits its operational output [13].

BT is a definite chemical compound possessing relatively-high-stability components, making it easy to sinter while maintaining good chemical stoichiometry. The low-temperature stable phase is a rhombohedral one with *R3m* space group. At 183 K this phase transforms into an orthorhombic with *C2mm* space group. With further heating, at 278 K this phase transforms into a tetragonal with *P4mm* space group. Finally, above 408 K the material undergoes a ferroelectric to paraelectric transition from the mentioned phase to a cubic with $Pm\bar{3}m$ space group [20]. Nevertheless, it should be noted that this material is not often used in its true chemical form, but combined with special additives as means of varying the ferroelectric transition temperature, flattening the ε_r, and controlling the defect chemistry or defect mobilities [87-89].

When BT is used in its primary application as a capacitor, specific dopants are used to achieve proper dielectric properties. Two general types of modifiers are commonly used: T_c shifters and T_c depressors. Examples of the former one are $SrTiO_3$, $CaZrO_3$, $PbTiO_3$ and $BaSnO_3$. They have the effect of shifting T_c to higher or lower temperatures, depending on the intended result. Depressors, such as $Bi_2(SnO_2)_3$, $MgZrO_3$, $CaTiO_3$, $NiSnO_3$, may be or not added together with the mentioned shifters. They are used to depress the sharpness of ε_r anomaly at T_c, thus giving a flattened ε_r [13].

3.1.5 $Bi_{0.5}Na_{0.5}TiO_3$-$BaTiO_3$ solid solution

The most studied solid solution between BNT and BT is the 0.94BNT-0.06BT. This system was first reported by Takenaka *et al.* [70]. They discovered the so called rhombohedral-tetragonal MPB at approximately 6 mol % BT, which is said to enhance the piezoelectric properties. At this composition, the system exhibits properties such as a piezoelectric constant d = 125 pC/N, coupling factor $k_p = 20\%$, $\varepsilon_r = 580$, and a high bending strength (∼200 MPa) [70]. Webber *et al.* [90] studied the phases present in this composition. They showed that the ferroelastic room temperature *R3m* rhombohedral phase evolved into a *P*4*mm* tetragonal phase at a T_d=87 °C. Further heating above this temperature up to 208 °C revealed that there is another structural transition before the structure evolved into a $Pm\bar{3}m$ cubic phase. Interestingly, this transition took place at the temperature where the frequency dependence in the ε_r vanished [90]. On the other hand, Takenaka *et al.* [70], among others [91], based on temperature-dependent ε_r measurements observed transitions that they assumed would be from ferroelectric to antiferroelectric phases at T_d=124 ºC and from antiferroelectric to paraelectric at T_m=242 ºC [91]. Both transitions occurred in a wide temperature range (*i.e.* gradually) when viewed in ε_r and tan(δ) measurements [70] [91] [92] (Figure 15).

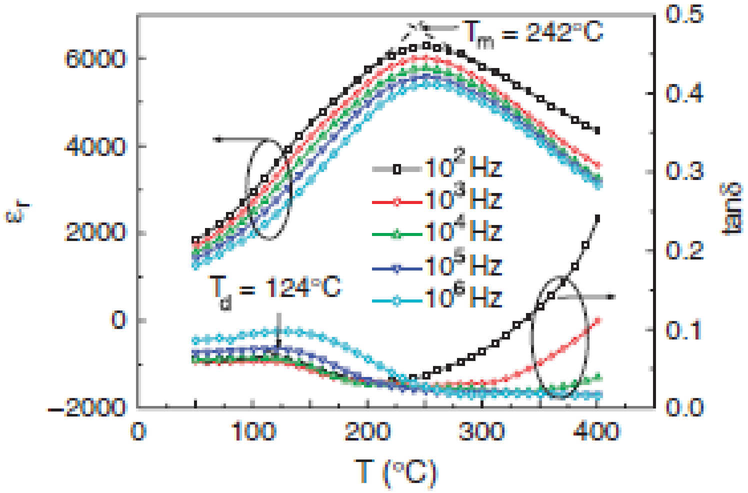

Figure 15: Temperature and frequency dependent dielectric properties of the 0.94BNT-0.06BT solid solution [91].

The phase temperature-dependent micro-Raman spectra, P(E) ferroelectric loops and temperature dependent bipolar S(E) curves were also reported. The results were similar to those mentioned above, showing diffuseness in the transitions such as in a relaxor material [91]. For these reasons, some authors believe that it is likely that the ε_r anomalies observed at T_d and T_m resulted from a relaxor-like behavior. Thus the observed diffuseness in these anomalies can be attributed to switching of nanopolar regions (such as in relaxor materials) and not to real phase transitions [92].

BNT has been combined in a binary system with BT in many investigations [17] [70] [93-95]. The phase diagram of this material obtained from scanning probe microscopy (SPM) performed in the piezoresponse force mode (PFM) for single crystals is presented in Figure 16. This study also confirmed the presence of nanopolar regions in the material similar to that present in relaxor-like materials, in agreement with other authors [92] [93].

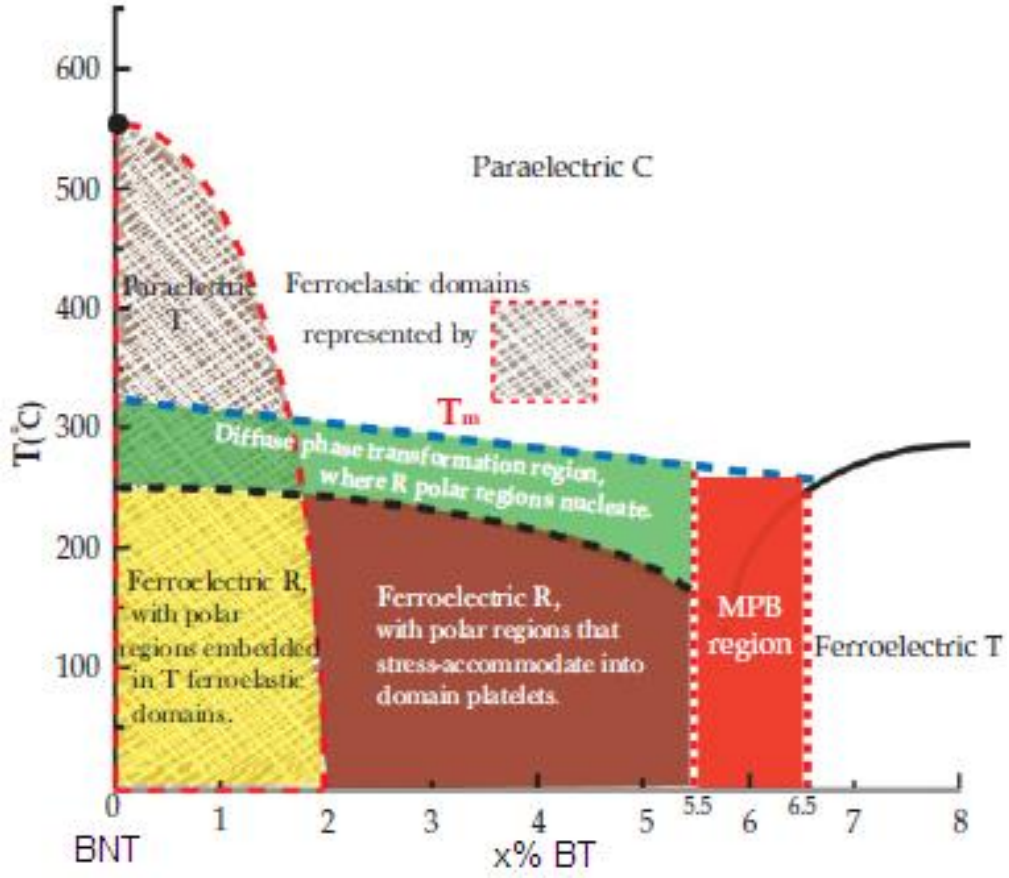

Figure 16: Diagram phase of the $(Bi_{1/2}Na_{1/2})_{1-x}Ba_xTiO_3$ system. A tetragonal (T) paraelectric phase, cubic (C) paraelectric phase, rhombohedral (R) ferroelectric and tetragonal ferroelectric phases can be seen. The last two phases mentioned are separated by a MPB and the paraelectric phases are separated from the ferroelectric ones by a diffuse phase transition. The presence of nanopolar regions was also observed in some phases by SPM performed in PFM [95].

It should be noted that the symmetries and properties at room temperature of unpoled samples differ from the poled ones [17]. Jo *et al.* [17] studied the system (1-x)BNT-xBT in a wide compositional range ($0<x<0.15$). The compositions 1BNT-0BT and 0.85BNT-0.15BT were identified as rhombohedral with *R3c* space group and tetragonal with *P4mm* space group, respectively. The Rietveld profile fitting method on the X-ray profiles was done in order to investigate the samples prior to poling. For the compositions between 0.94BNT-0.06BT and 0.9BNT-0.10BT, the given refinement parameters and X-ray data resulted in an assignment of a *R3m* space group. It was observed that dielectric properties supported its presence.

The properties at room temperature of unpoled and poled (at 6 kV/mm) samples are presented in Figure 17, respectively.

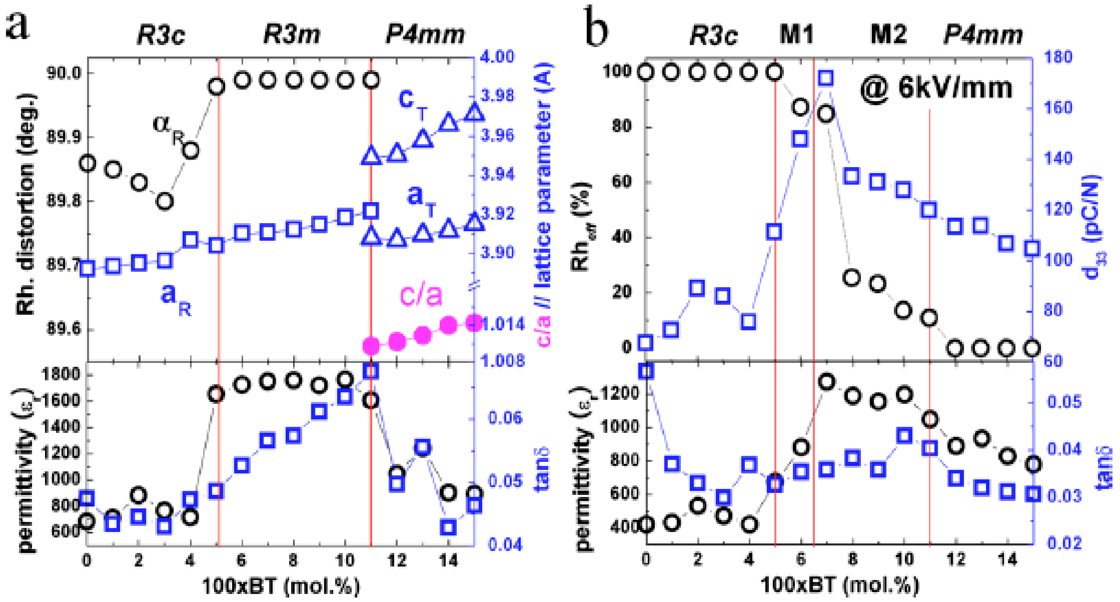

Figure 17: Phase diagram and dielectric properties (a) Before and (b) After poling, where crystal structure and phase content of (1-x)BNT-xBT are contrasted to: composition-dependent permittivity, loss factor and piezoelectric coefficient [17].

Note that the structural transformation that might conventionally be regarded as one of the features of MPB occurs at 0.89BNT-0.11BT for unpoled samples, which deviates significantly from the maximum in the electrical properties reported at 0.06-0.07 BT in the literature [70]. It can also be seen that the peak in ε_r at 0.89BNT-0.11BT is coincident with that of the tan(δ); moreover, in poled and unpoled samples a local minima is observed in the 0.88BNT-0.12BT composition. On the other hand, the abrupt change found in ε_r for the 0.95BNT-0.05BT sample is not followed by one in the tan(δ). For this reason, the last anomaly was attributed to a slight change in structure such as a tilting transition, while the former one due to the major change in the dielectric properties was attributed to a large scale instability such as a space group change (Figure 17).

The poled samples were studied observing their microestructural evolution with electric field by *in situ* synchrotron diffraction. It was seen that the poling altered the phase fraction, resulting in an extension in the composition range of the two phase coexistence. Four distinct structural regions were identified: the space groups *R3c* at the left hand side and the *P4mm* at the right hand side remained unaffected. However, the *R3m* rhombohedral compositions evolve into a two-phase mixture, either *R3c* and *P4m(b)m* (called region M1) or *R3m* and *P4mm* (called region M2). As expected, the compositional dependence of the dielectric properties changed significantly after the poling treatment [17].

On the other hand, it should also be mentioned that other authors proposed a phase mixture in unpoled samples at room temperature for the compositional range 0.94BNT-0.06BT and 0.9BNT-0.1BT. This second phase proposed were nanopolar regions, in analogy to relaxor-like materials [93] [96].

As can be seen from the scarce consistency in the presented results, the phase diagram of the BNT-BT system is still an open complex topic. Cordero *et al.* [94] reported that it is likely that the exact stoichiometry and degree of ordering of cations determine the detailed structural distortions, their correlation lengths and domain morphologies. In other words, the differences in results may result from differences in the samples quality [94].

Oxygen vacancies have an important effect on electrical properties in perovskite structures [97] [98]. Since doping can be made with heterovalent ions, they are formed due to charge compensation; moreover, the sintering atmosphere has an important effect on them as well. Babu *et al.* [97] prepared 0.94BNT-0.06BT single crystals, which afterwards were heat-treated in different atmospheres. With this method, they succeeded to obtain samples with different oxygen vacancy concentrations and they observed that the sample with less oxygen vacancy concentration had experienced a lowered tan(δ) [97]. Chen *et al.* [98] [99] studied the 0.94BNT-0.06BT and 0.94BNT-0.06BT doped with $BiFeO_3$ systems sintered in O_2 and N_2 atmospheres. It was observed that all the samples presented a mixture of rhombohedral and tetragonal symmetries. However, the samples sintered in N_2 had a decreased relative amount of tetragonality compared to that sintered in O_2 atmosphere. Moreover, for the samples sintered in the same atmosphere, the doped ones presented a decreased percentage of tetragonality. It was also observed that for a given composition and frequency the ε_r anomaly corresponding to N_2 atmosphere sintered samples was higher and occurred at lower temperature than that for the O_2 atmosphere sintered ones. For the same sintering atmosphere, the T_m was higher for the doped samples and increased with increased doping [99]. All the samples presented a diffuse phase transition and their phase transitions were described by a modified Curie-Weiss law with a diffuseness exponent γ near two. This parameter increased with oxygen vacancy concentration and with $BiFeO_3$ concentration. However, it was observed that T_m did not exhibit an obvious up-shift with increasing frequency, as in classic relaxor materials [98]. From these results the importance of oxygen vacancy concentration can be observed, and thus the importance on the doping ions charge and sintering atmosphere.

Park *et al.* [63] studied the $0.935(Bi_{0.5}Na_{0.5})(Ti_{1-x}Zr_x)O_3$-$0.065Ba(Ti_{1-x}Zr_x)O_3$ system. It was observed that with increasing Zr concentration, the coexisting MPB region gradually transformed to a tetragonal (*i.e.* pseudo-cubic symmetry). With increasing Zr, the phase transition became more diffused and also the T_d was lowered. For instance, the composition with 10 mol % presented a flattened ε_r and tan(δ) below 20%; therefore, this material can be considered as a candidate for high-temperature dielectrics in the range from room temperature to 600 ºC. It was also observed that the ferroelectric hysteresis loop at room temperature decreases with increasing Zr, which would indicate a decay in the ferroelectricity with increasing doping. For the composition with 10 mol %, the linearity in the ferroelectric hysteresis loop was almost achieved [63]. Peng *et al.* [100] studied the $(1-x)(Bi_{1/2}Na_{1/2})TiO_3$-$xBa(Ti,Zr)O_3$ (BZT) system. With increasing BZT, an increase in the tetragonality was observed at the MPB for the compositions from 0 to 12 mol % of BZT. It was observed that the T_m was decreased and the ε_r anomaly increased with increasing BZT content; however, when the addition of BZT exceeded 9 mol %, the T_m increased. As it can be observed, the ε_r anomaly at T_m had a contradictory trend in both Zr-doped studies for low concentrations of Zr. This inverse trend was also observed in the ferroelectric hysteresis loops at room temperature for compositions with less than 9 mol % BZT [100]. These differences may be attributed to the difference in BNT concentration. It should also be highlighted that Zr doping had an important effect in the dielectric properties of the systems studied [63] [100].

Zuo *et al.* [101] studied the 0.94BNT-0.06BT system doped with 0- 4 mol % of Ta. All the samples presented a rhombohedral symmetry with two observable anomalies in the ε_r, which were decreased with increasing Ta content. The first anomaly was gradually shifted to lower temperatures, while the second increased slightly with increasing Ta doping. These phenomena resulted in an almost constant ε_r for the 4 mol % Ta composition; therefore, this material is attractive for high-temperature dielectrics in the range from room temperature to 500 ºC. The ferroelectric hysteresis loop was also measured and a pinched loop (similar to that of an antiferroelectric-like or relaxor-like material) was observed [101].

3.1.6 $Bi_{0.5}Na_{0.5}TiO_3$-$BaTiO_3$-$K_{0.5}Na_{0.5}NbO_3$ solid solution

The BNT-BT binary solid solution was studied several times with the addition of $K_{0.5}Na_{0.5}NbO_3$ in order to improve piezoelectric and dielectric properties [2] [102]. This addition gives rise to a complex ternary solid solution system.

Zhang *et al.* [103] reported that BNT-BT-KNN was an interesting starting material for the development of new lead-free electrostrictors. Specifically, the compositions between 15 and 30 mol % KNN were studied. It was observed that the compositions with 20 and 25 mol % showed a pure electrostrictive behavior with a low dissipated energy and high electrostrictive coefficient. It was also reported that ε_r and tan(δ) of all the compositions studied presented typical relaxor-like characteristics. In the sample with 30 mol % a variation within 10% in its ε_r was observed in the temperature range from 40 to 250 °C [103].

In another study, Zhang *et al.* [102] reported that the solid solution 0.82 (0.94 BNT-0.06BT)-0.18KNN was a very promising electrostrictor compared with lead-based materials, mainly due its high strains and high electrostrictive coefficient at room and high-temperatures. Moreover, Dittmer *et al.* [2] studied the $(1–x)(0.94Bi_{0.5}Na_{0.5}TiO_3$-$0.06BaTiO_3)$-$xK_{0.5}Na_{0.5}NbO_3$ system (x=0.09, 0.12, 0.15 and 0.18). This study resulted in the development of a high-temperature dielectric material for the 18% KNN doped sample. As said, this material was not able to work properly at low-temperatures. Nevertheless, a reliable operating temperature range from 43 to 319 ºC within 10% of variation in its ε_r was achieved.

Hinterstein *et al.* [104] studied the structural differences between poled and unpoled samples in the $0.94Bi_{0.5}Na_{0.5}TiO_3$-$0.06BaTiO_3$-$0.02K_{0.5}Na_{0.5}NbO_3$ system. The unpoled ones were studied with high resolution X-ray and neutron diffraction at room temperature. The presence of a tetragonal phase with *P4bm* space group, and in-phase oxygen octahedral tilts along the c axis ($a^0a^0c^+$) was observed. These results were in agreement with transmission electron microscopy (TEM), X-ray and neutron diffraction studies made by Schmitt *et al.* [105]. The atomic positions exhibited the same unusual antiparallel cation displacements reported by Jones *et al.* [79]. In other words, due to the antiparallel static displacement and the low tetragonal distortion (almost cubic), the resulting spontaneous polarization was almost negligible and thus this phase was considered as non-polar. These structural results are unexpected for a normal ferroelectric material. The combination of static displacements and large isotropic displacement parameters for the A-site cations indicated a broad deviation of local displacements as found in relaxor-like materials.

Moreover, it was also observed that the unpoled samples phase structure differed from that of the poled ones (at 6.0 kV /mm). In the latter, the same phase described coexisted with a rhombohedral one with *R3c* space group and ($a^-a^-a^-$) oxygen tilts. The non-polar tetragonal phase can be considered as a locally ordered precursor for the ferroelectrically active rhombohedral phase. These results indicated that the KNN stabilized the tetragonal pseudocubic phase with *P4bm* space group in the BNT-BT system at room temperature. Moreover, an analogy to the nanopolar regions in relaxor-like materials can be drawn: the initial structure presented a pseudocubic structure with short-range ordering of the octahedral tilting and A-site cation displacements, *i.e.* nanopolar regions; and in addition, the non-polar tetragonal phase was a precursor for the ferroelectrically active rhombohedral phase [106].

Based on the mentioned results and high-temperature (up to 300 ºC) *in situ* X-ray measurements, Dittmer *et al.* [2] proposed phase transitions for the $0.82(0.94Bi_{0.5}Na_{0.5}TiO_3$-$0.06BaTiO_3)$-$0.18K_{0.5}Na_{0.5}NbO_3$ material. At 160 ºC a ferroelectric/ferroelastic tetragonal phase with a *P4bm* space group transformed into a paraelectric/ferroelastic tetragonal phase with a *P4/mbm* space group. With further heating, at approximately 250 ºC the last mentioned phase transformed into a paraelectric/paraelastic cubic with a $Pm\bar{3}m$ space group. Moreover, since a ε_r anomaly at temperatures below 100 ºC was observed and the mentioned X-ray patterns showed no obvious structural change, an assumption that the material behaved as a relaxor can be made [2]. This supports the results found by Hinterstein *et al.* [104].

4 Experimental methodology

4.1 Powder and Ceramics Processing

The ceramic powders were produced via a mixed oxide route using reagent grade oxides and carbonates (Alfa Aesar GmbH & Co. KG). First, the Bi_2O_3 (purity 99.975%), Na_2CO_3 (purity 99.5%), TiO_2 (purity 99.9%), $BaCO_3$ (purity 99.8%), K_2CO_3 (purity 99.0%), Nb_2O_5 (purity 99.9%), $CaCO_3$ (purity 99.5%) and ZrO_2 (99.5%) were mixed according to the stoichiometric formulas of the two systems developed:

- $(1–x)(0.94Bi_{0.5}Na_{0.5}TiO_3–0.06BaTiO_3)–xCaZrO_3$
- $(1–x)(0.82(0.94Bi_{0.5}Na_{0.5}TiO_3–0.06BaTiO_3)–0.18K_{0.5}Na_{0.5}NbO_3)–xCaZrO_3$,

where x=0, 0.05, 0.10 and 0.20.

All the powders were introduced in alumina containers, with stabilized zirconia balls and ethanol. These suspensions were ball-milled in a planetary ballmill (Fritsch Pulverisette 5) for 24 h at 250 rpm. Afterwards, the suspensions were dried at 100 °C (Oven D-91126, Memert GmbH & Co. KG) till the ethanol was totally evaporated and powders were obtained after being ground. These powders were calcined (L9/11/S27, Nabertherm Corporation) according to the time-temperature curve observed in Figure 18.

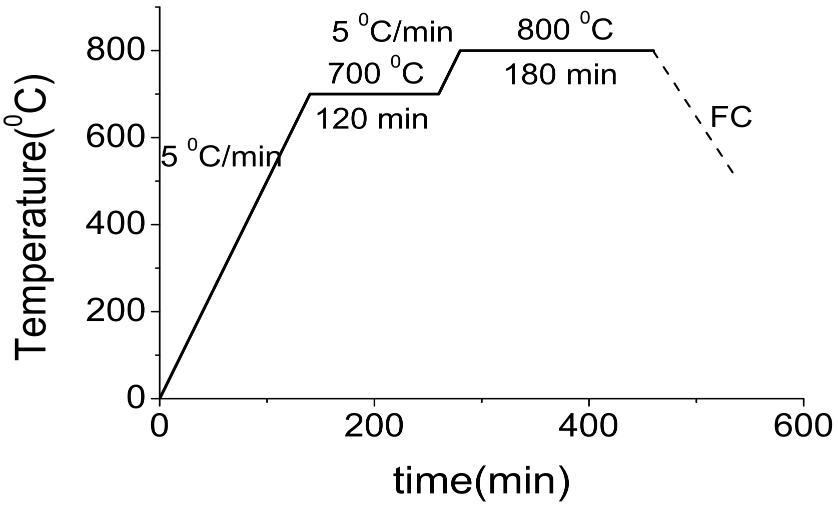

Figure 18: Calcination time-temperature curve. Note that the cooling down (dashed line) was done in the furnace (FC).

Subsequently, the obtained powders were ball-milled again for 24 h with the same conditions previously mentioned. Grounded powders were finally compacted into pellets of 30 mg (BalanceTE214S, Sartorius) and 10 mm in diameter in a manual uniaxial pressing machine. In order to increase the final density, the compacted powders were hydrostatically pressed (KIP 100 E, Weber-Pressen) under 25 MPa. The green bodies obtained were sintered in alumina crucibles with atmospheric powder of the same composition (in order to minimize the loss of volatile elements) according to the time-temperature curve observed in Figure 19 (L16/14, Nabertherm Corporation)[9].

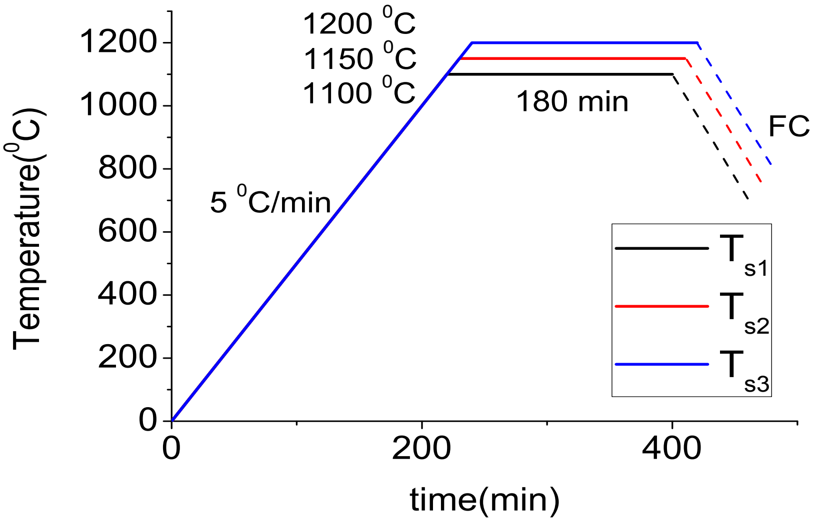

Figure 19: Sintering time-temperature curves: T_{s1} (max. T=1100 °C), T_{s2} (max. T=1150 °C) and T_{s3} (max. T= 1200 °C). The samples were cooled down in the furnace (FC).

Finally, the sintered pellets were grounded (200 grit), polished (600, 1200 and 2000 grit) (manual machine Dap-V, Struers) and electroded with a silver paste on both sides. These electrodes needed an annealing treatment (L9/11/S27, Nabertherm Corporation) in order to be burnt-in completely (and thus allow subsequent high-temperature measurements). This time-temperature curve is observed in Figure 20.

---

[9] If any other sintering temperature than 1100 °C is used, it will mentioned explicitly.

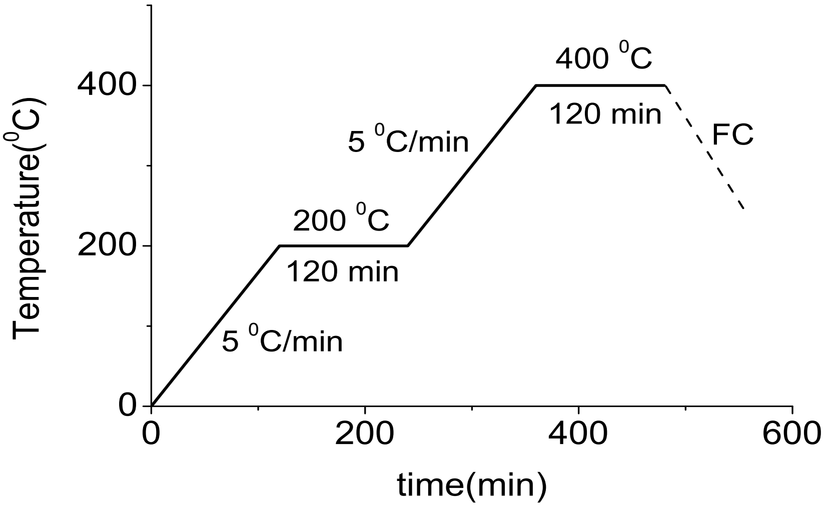

Figure 20: Tempering electrode time-temperature curve. Samples were cooled down in the furnace (FC).

4.2 Structure and Microstructure

4.2.1 X-ray diffraction

The XRD from all the samples were obtained in a Bragg-Brentano geometry diffractometer (D5000, Siemens Corporation). All the XRD were performed at room temperature on powders obtained from ground sintered unpoled samples. Prior to the measurement all the powders were annealed (Oven L9/11/S27, Nabertherm Corporation) at 300 ºC for 30 minutes in order to relieve stresses. The measurement was done in the 2θ range from 10 to 80º, with a step width of 0.05º. The probing x-ray beam was Cu $K_{\alpha 1}$ with a λ=1.5406 Å.

4.2.2 Differential Scanning calorimetric measurements

The DSC measurements were done in powders obtained from ground sintered unpoled samples. Prior to the measurement all the powders were annealed at 300 ºC for 30 minutes in order to relieve stresses. The measurements were performed with heating and cooling rates of 10 K/min in the temperature range from 0 to 580 ºC. In order to achieve these rates the samples were measured under a flowing nitrogen gas with a flow rate of 20 ml/min. The equipment used was a DSC 200 F3 Maia®-Differential Scanning Calorimeter (Netzsch Gerätebau GmbH).

4.2.3 Density measurements

The density measurements were done in the sintered samples by a classical Archimedes method. First, the samples were dried 24 hours at 100 ºC. Thereafter, they were weight (for all the density measurements Balance BA110S Basic, Sartorius) (dry weight(DW)). The samples were introduced in distilled water and into a vacuum chamber (RD8, Vacuubrand) for a period of 1 hour and a pressure of 50 mbar. Afterwards, they were left in water for 24 hours in order to favor the water diffusion. The samples were weight (saturated weight in water (SWW)) in water and then dried in a clean paper. Immediately after, they were weight again (saturated weight in air (SWA)). The density of each sample (δ_{ss}) was calculated taking into account the Archimedes principle (Equation 12) and the density of the water for a given temperature (corresponding to the moment of the measurement).

$$\delta_{ss} = \frac{\delta_{H_2O} * DW}{SWA - SWW} \qquad \text{Equation 19}$$

4.2.4 High-resolution electron microscopy

A HREM (XL 30 FEG, Philips Corporation) was employed to analyze the microstructure of all the samples sintered at 1100 ºC. The samples were first ground with a semiautomatic polishing machine (Phoenix 4000, Jean Wirtz) (200 grit) and polished (600, 1200, 2000 grit). This process was followed by two different thermal etchings, as can be seen in the time-temperature curve from Figure 21.

Afterwards, the samples were sputtered (Sputter Coater SCD 050, Bal-Tec Corporation) with an Au-Pd alloy for 60 seconds with a current of 60 mA to ensure conductivity. Thus, taking into account the manuals catalogue a covering metal film of approximately 25 nm was expected.

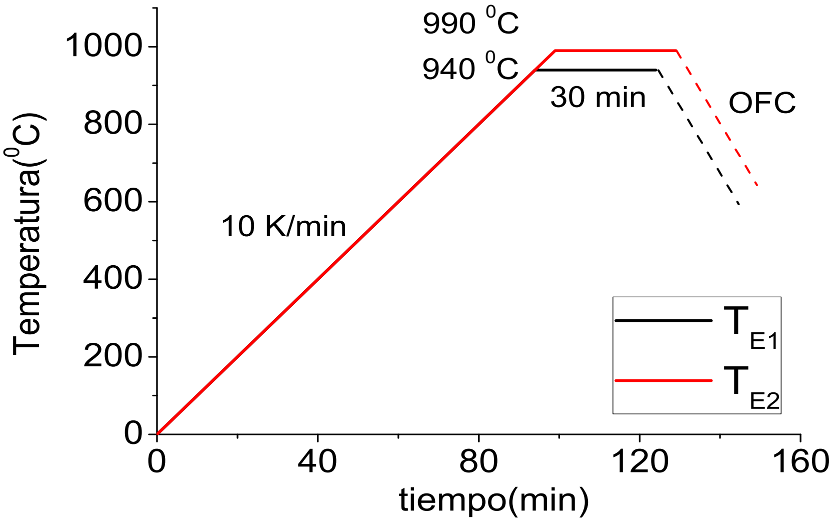

Figure 21: Thermal etching time-temperature curves: T_{E1} (max. T=940 ºC) and T_{E2} (max. T=990 ºC). The samples were cooled down with open oven (OFC).

4.3 Electrical characterization

4.3.1 Temperature and frequency dependent relative permittivity and losses

Temperature and frequency dependent ε_r and tan(δ) were measured in the unpoled samples for all the compositions. The parameters used for the measurements were frequencies of 10^2, 10^3, 10^4, 10^5, 10^6 Hz with amplitude of 1V. The temperature range measured was from -150 to 500 ºC. Due to the wide-temperature range investigated two machines were used to do the measurements. For high-temperatures a Precision LCR Meter 4284A (Hewlett Packard Corporation) was used, while for the low-temperature measurements a Alpha-A High Resolution Dielectric, Conductivity, Impedance and Gain Phase Modular Measurement System together with a Quatro Cryosystem 6.1 (Novocontrol Technoogies GmbH & Co) was employed. The samples were measured on heating and cooling (in order to study the thermal hysteresis) with rates of 2 K/min.

4.3.2 Direct current conductivity measurements

Conductivity measurements were conducted with a direct high-voltage power source (HCB, Fug). All the samples were measured with a voltage of 80 V and from room temperature to 450 ºC. The samples were heated using a temperature regulator (K43, UTRECS) and the direct current (DC) was measured by an electrometer/high resistance meter (6517B, Keithley).

4.3.3 Polarization and strain measurements

A Sawyer-Tower circuit was employed for the polarization measurements at room temperature (Figure 22). A sample with a capacity C_s was connected in series with a measurement capacitor C_m (note that to minimize the voltage drop U_m at this capacitor the condition $C_m \gg C_s$ should be satisfied). The measurement capacitor chosen was C_m=15 µF (note that C_s~10 pF). The charge Q of the measurement capacitor is equivalent to the sample’s charge response to the applied electric field since they are in series (Equation 20). A function generator (Function/Arbitrary Wave form Generator 33220A, Agilent Corporation) supplied a signal to the voltage supply (High Voltage Amplifier PZD 2000A, Trek, Inc) with uni- and bipolar signals of 6 kV/mm and a frequency of 40 Hz. Two cycles were done of each measurement in all the samples. The operational amplifier together with the measurement capacitor acted as charge converter. Furthermore, the operational amplifier increased the input resistance in order to achieve a suitable discharge time of C_m. Data acquisition was performed via an oscilloscope. The polarization was calculated based on Equation 21.

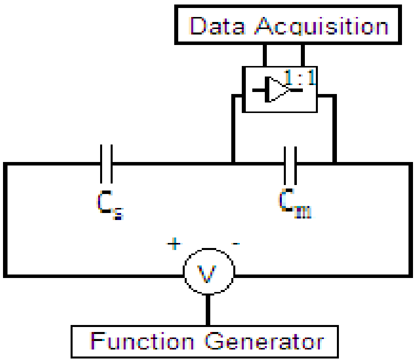

Figure 22: Sawyer-Tower circuit, signal generator and data acquisition scheme employed for the polarization measurements.

$$\mathrm{Q} = \mathrm{C_s} \cdot \mathrm{U_s} = \mathrm{C_m} \cdot \mathrm{U_m} \qquad \text{Equation 20}$$

$$\mathrm{P} = \frac{\mathrm{C_m} \cdot \mathrm{U_m}}{\mathrm{A}} \qquad \text{Equation 21,}$$

where A is the section of the sample.

The strain was measured by an optical sensor (D63, Philtec) at the same place that the polarization measurements were done. This device is able to measure high-frequency displacement changes. Electrical contact to the sample was realized by two adjustable point contacts. The bottom contact (high voltage) was placed inside a container filled with silicon oil (AK 35, Wacker Chemie). This allowed electrical fields up to 12kV/mm.

5 Results and Discussion

5.1 Structure and Microstructure

5.1.1 X-ray diffraction

The XRD studies were carried out in order to investigate changes in the lattice constants with increasing doping, appearance of secondary phases and to confirm the perovskite-type structure of the materials synthesized.

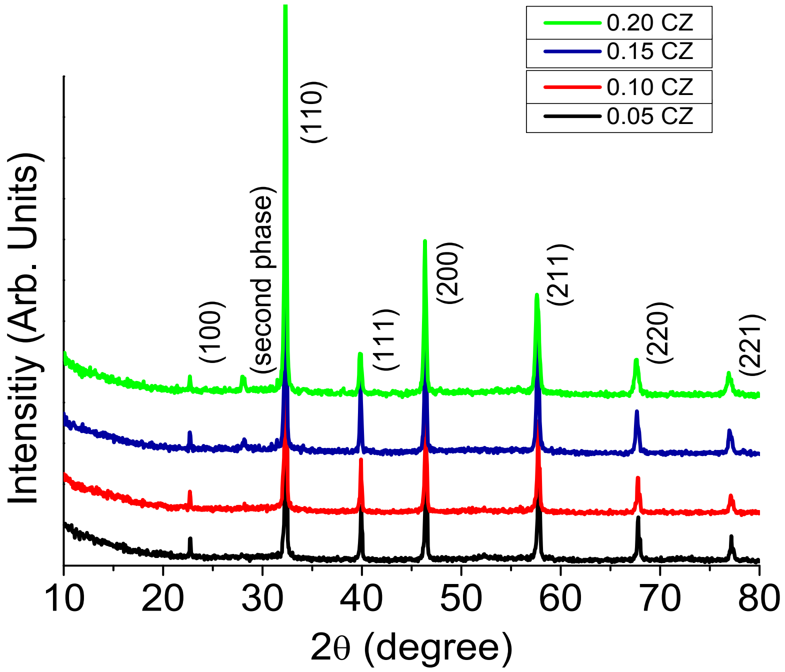

Figure 23: XRD patterns for the BNT-BT-CZ samples measured at room temperature. A cubic perovskite-type structure can be observed. In 15 and 20 % CZ samples the presence of a second phase is observed.

All the peaks appearing in the XRD patterns for the BNT-BT-CZ and the BNT-BT-KNN-CZ systems correspond to a cubic perovskite-type unit-cell for both systems (Figure 23 and Figure 24). This symmetry can be deduced form the XRD peaks position and since no clear splitting from the (110), (220), (221) peaks is observed. It should be highlighted that the (210) peaks cannot be observed in the XRD patterns from both systems; moreover, for the BNT-BT-KNN-CZ system the (100) peak cannot be observed neither. This can be attributed to the insufficient intensity of the X-ray source used. Note that for the BNT-BT-0.15CZ, BNT-BT-0.2CZ and BNT-BT-KNN-0.2CZ samples a secondary phase is observed.

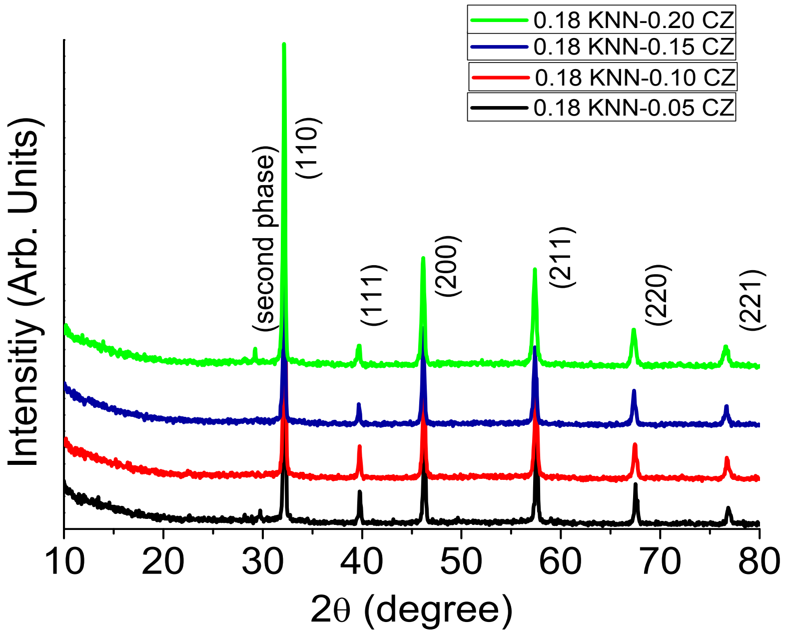

Figure 24: XRD patterns for the BNT-BT-KNN-CZ samples measured at room temperature. A cubic perovskite-type structure can be observed. In the 20 % CZ sample the presence of a second phase is observed.

The XRD patterns of the samples sintered at 1150 and 1200 ºC were also measured and present peaks that correspond to a cubic perovskite-type unit-cell (Figure 25). Moreover, a secondary phase can also be seen in these samples. Therefore, the solubility limit of the BNT-BT based material is around 15% CZ content.

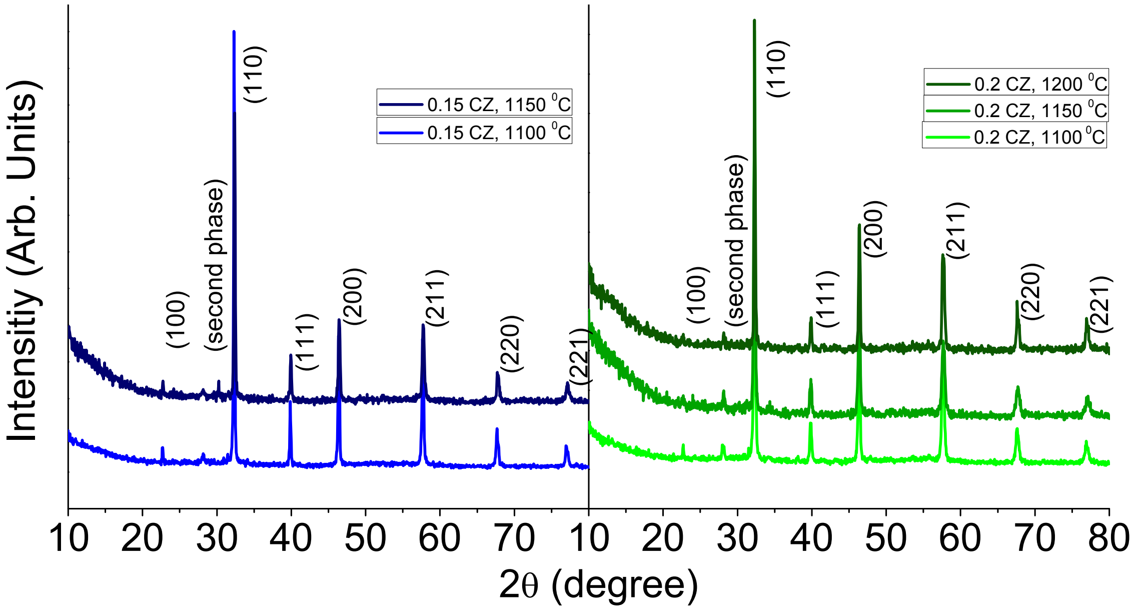

Figure 25: Effect of sintering temperature in the samples with 15% (left) and 20% (right) CZ doping on the XRD patterns. It can be seen that the second phase is still appearing in the materials sintered at 1150 and 1200 ºC.

The lattice parameter of each material was calculated taking into account Bragg's law (n λ=2d sin(θ)) and a cubic unit-cell. An almost linear change in the lattice parameter with increasing CZ doping in the BNT-BT-CZ and BNT-BT-KNN-CZ systems can be seen in Figure 26.

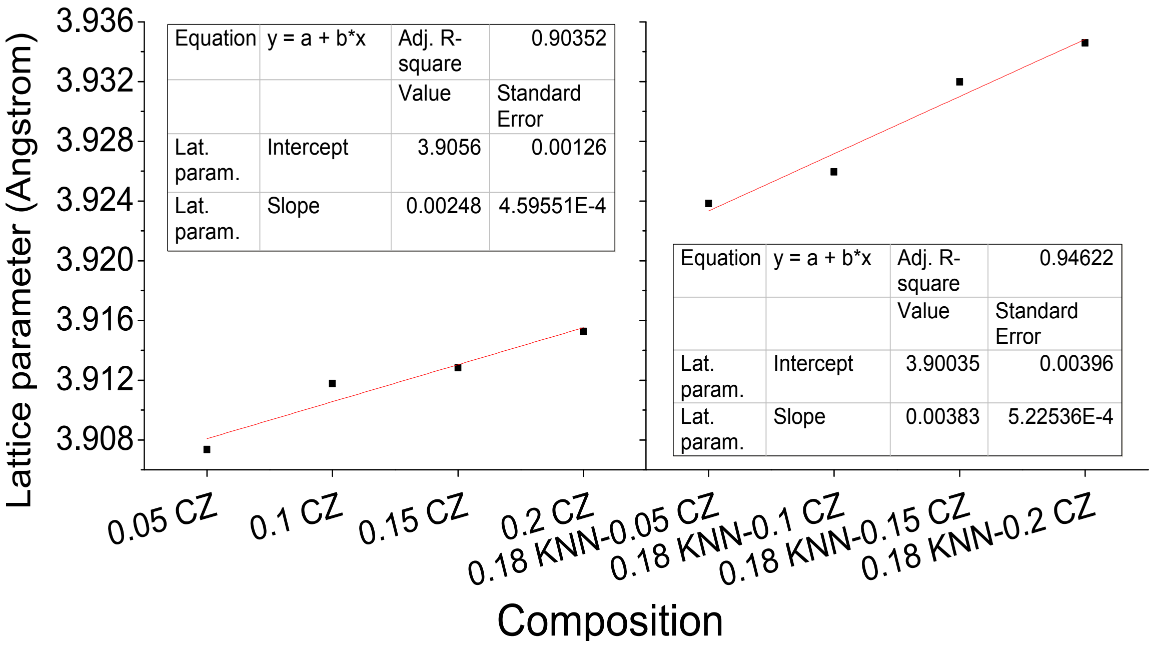

Figure 26: Effect of CZ doping in the lattice parameter of the BNT-BT-CZ and BNT-BT-KNN-CZ systems. An almost linear increase in the lattice parameter with increasing CZ doping is observed.

Taking into account the ionic radii of the elements introduced in both systems, the stoichiometry of each of the materials and the lattice site positions an average ionic radius can be calculated for the A- and B-site, respectively (Table 2). From Table 2, it can be observed that with increasing CZ doping the average A-site ionic radius decreases, while the average B-site ionic radius increases for both BNZT-BT-CZ and BNT-BT-KNN-CZ systems. Moreover, the increased t parameter (Goldschmidt, 1926) may be associated with increasing tilting and rotations of the oxygen octahedra. Taking this into account an increase in the lattice parameter is expected for both systems with increasing CZ content. Moreover, the A- and B-site ionic radii are slightly superior in the BNT-BT-KNN-CZ system compared to the BNT-BT-CZ one; therefore, a bigger lattice parameter would also be expected for the former system. Both expected results can be observed in Figure 26.

In Figure 27, a reduction in the lattice parameter with increasing sintering temperature can be observed for the 15 and 20% CZ samples.

Element	Charge	Ionic radius (pm)	Lattice site	0.05CZ	0.1CZ	0.15CZ	0.2CZ
Bi	3	117	A	52.24	49.49	46.74	43.99
Na	1	116	A	51.79	49.07	46.34	43.62
Ti	3	81	B	76.95	72.90	68.85	64.80
O	-2	126	O	378.00	378.00	378.00	378.00
Ba	2	149	A	8.49	8.05	7.60	7.15
Ca	2	114	A	5.70	11.40	17.10	22.80
Zr	4	86	B	4.30	8.60	12.90	17.20
			A-site average	118.23	118.01	117.78	117.56
			B-site average	81.25	81.50	81.75	82.00
			t parameter	0.8333	0.8315	0.8297	0.8280
Element	Charge	Ionic radius (pm)	Lattice site	KNN-0.05CZ	KNN-0.1CZ	KNN-0.15CZ	KNN-0.2CZ
Bi	3	117	A	42.84	40.58	38.33	36.07
Na	1	116	A	52.39	49.63	46.87	44.12
Ti	3	81	B	63.10	59.78	56.46	53.14
O	-2	126	O	378.00	378.00	378.00	378.00
Ba	2	149	A	6.96	6.60	6.23	5.86
K	1	152	A	13.00	12.31	11.63	10.94
Nb	3	86	B	14.71	13.93	13.16	12.38
Ca	2	114	A	5.70	11.40	17.10	22.80
Zr	4	86	B	4.30	8.60	12.90	17.20
			A-site average	120.89	120.52	120.16	119.80
			B-site average	82.11	82.31	82.52	82.72
			t parameter	0.8389	0.8368	0.8348	0.8327

Table 2: Element ionic radii for the BNT-BT-CZ and BNT-BT-KNN-CZ systems [107]. The Goldschmidt parameter t and the ionic average radius for the A- and B-site were calculated.

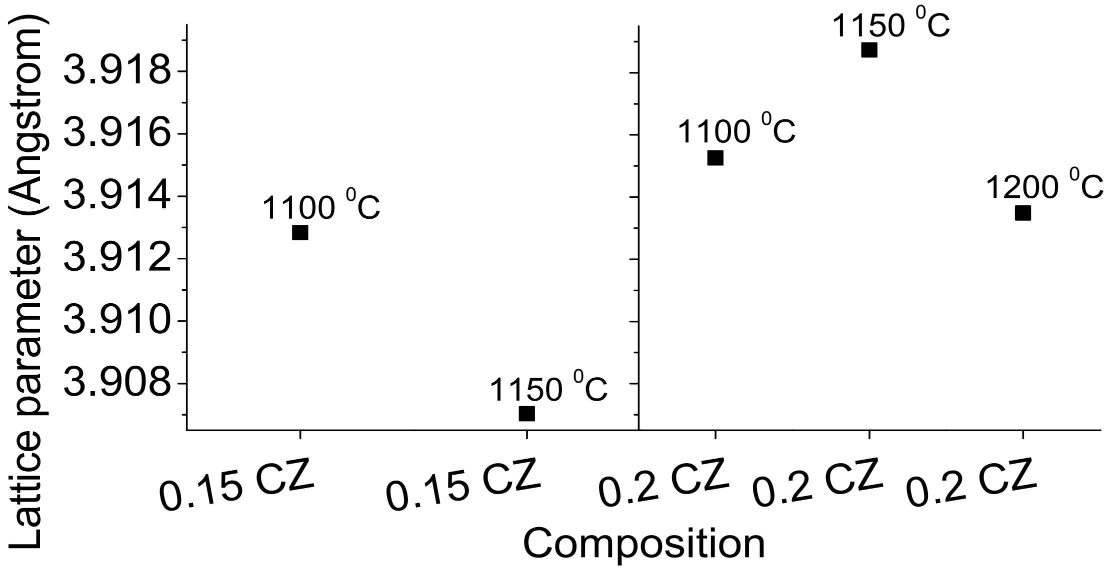

Figure 27: Effect of the sintering temperature in the BNT-BT-0.15CZ and BNT-BT-0.2CZ samples. Note that a decrease in the lattice parameter for higher sintering temperatures is observed.

5.1.2 Differential scanning calorimetric measurements

The DSC measurements were done in order to confirm structural changes in the material at different temperatures. The measurements on heating and cooling for the BNT-BT-0.05CZ, BNT-BT-0.15CZ, BNT-BT-KNN-0.5CZ and BNT-BT-KNN-0.15CZ samples are observed in Figure 28 to Figure 31. All the peaks appearing in the DSC measurements are summarized in Table 3.

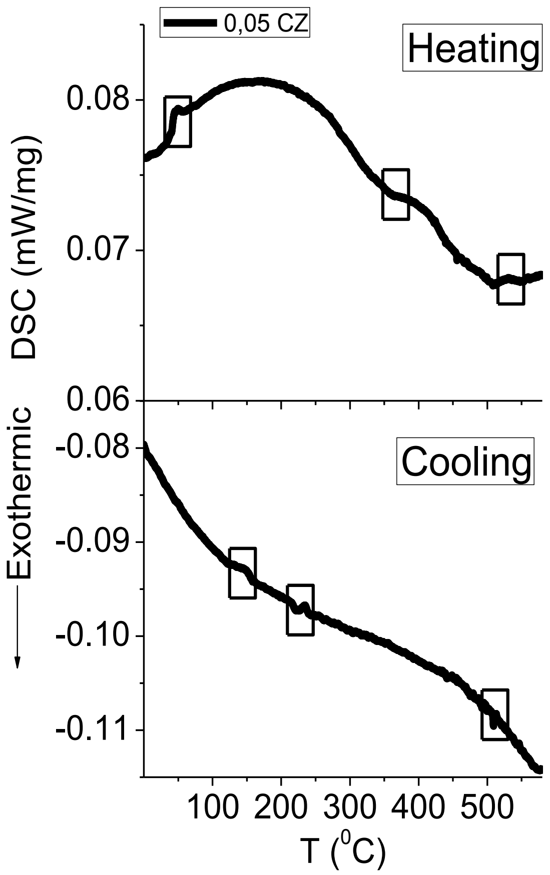

Figure 28: DSC measurements of the BNT-BT-0.05CZ sample on heating and cooling. Note on heating the presence of two endothermic and an exothermic peak. On cooling, two endothermic and an exothermic peak are observed.

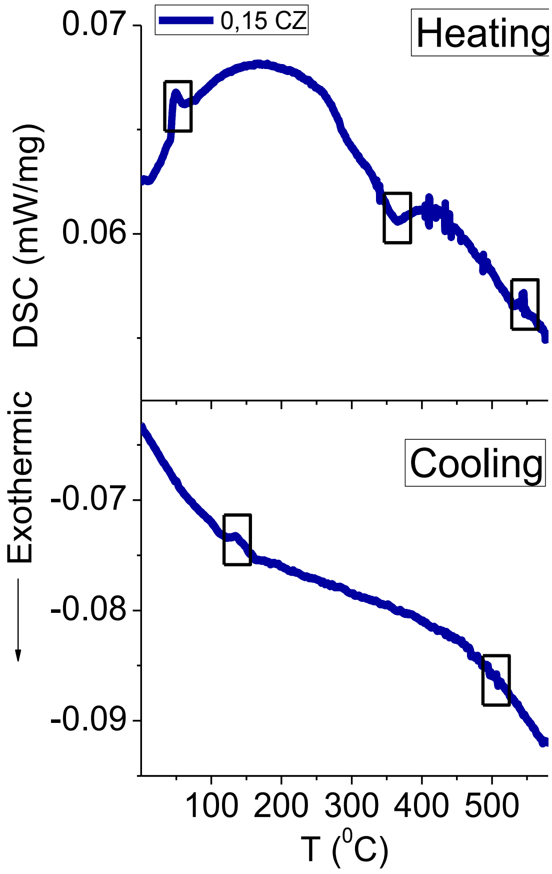

Figure 29: DSC measurements of the BNT-BT-0.15CZ sample on heating and cooling. Note on heating the presence of two endothermic and an exothermic peak. On cooling, an endothermic and an exothermic peak are observed.

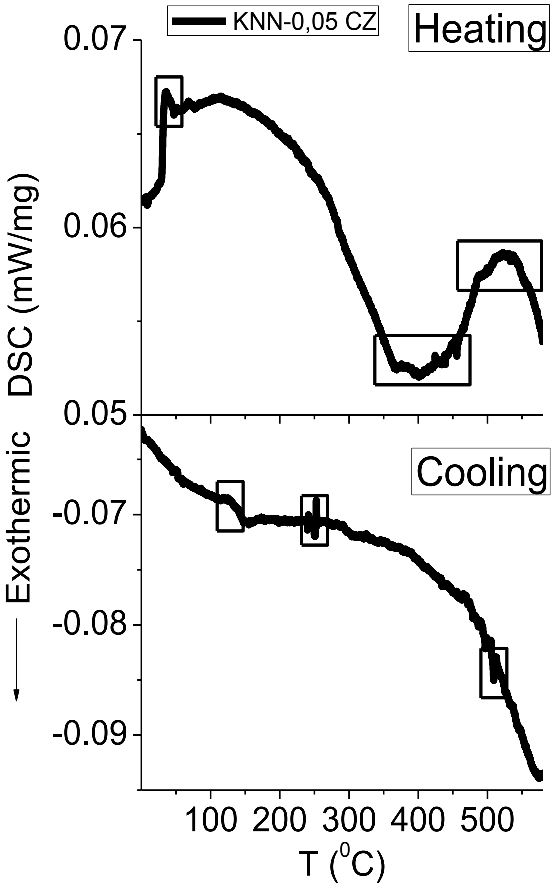

Figure 30: DSC measurements of the BNT-BT-KNN-0.05CZ sample on heating and cooling. Note on heating the presence of two endothermic and an exothermic peak. On cooling, two endothermic and an exothermic peak are observed.

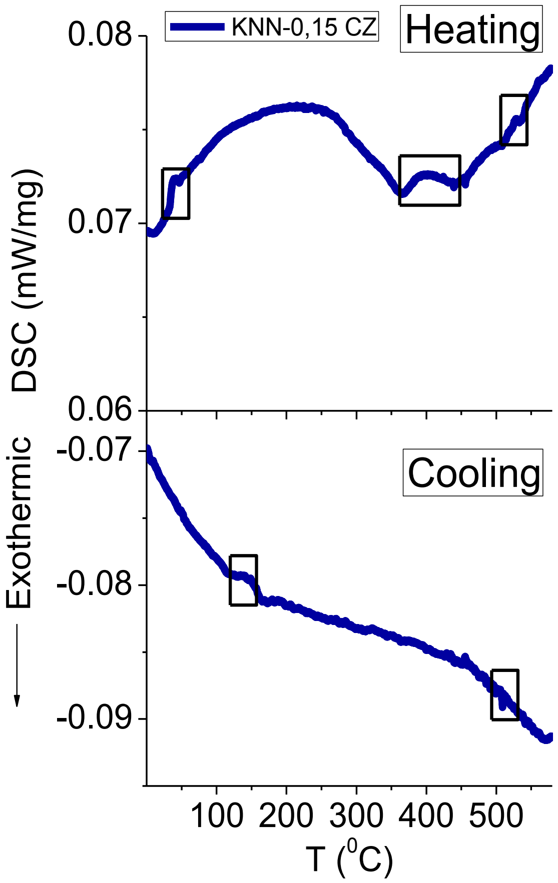

Figure 31: DSC measurements of the BNT-BT-KNN-0.15CZ sample on heating and cooling. Note on heating the presence of three endothermic peaks. On cooling, an endothermic and an exothermic peak are observed.

Almost all the peaks appearing in both systems are endothermic (Table 3). Moreover, no appreciable change in the heat flow is observed in the BNT-BT-0.05CZ and BNT-BT-0.15CZ samples, which may indicate that there are no phase transitions in the temperature range measured. This result is in agreement with another reported in literature [108]. On the other hand in the BNT-BT-KNN-0.5CZ and BNT-BT-KNN-0.15CZ samples more appreciable changes in the heat flow can be observed, which may indicate long-range symmetry distortions. Taking into account results from literature this may not be discarded [2].

Composition	Heating/cooling	Peak temperature (^{0}C)	Heat flow
BNT-BT-0.05CZ	Heating	50	Endothermic
BNT-BT-0.05CZ	Heating	364	Exothermic
BNT-BT-0.05CZ	Heating	530	Endothermic
BNT-BT-0.05CZ	Cooling	134	Endothermic
BNT-BT-0.05CZ	Cooling	234	Endothermic*
BNT-BT-0.05CZ	Cooling	509	Exothermic
BNT-BT-0.15CZ	Heating	49	Endothermic
BNT-BT-0.15CZ	Heating	365	Exothermic
BNT-BT-0.15CZ	Heating	545	Endothermic
BNT-BT-0.15CZ	Cooling	134	Endothermic
BNT-BT-0.15CZ	Cooling	509	Exothermic
BNT-BT-KNN-0.05CZ	Heating	36	Endothermic
BNT-BT-KNN-0.05CZ	Heating	413	Exothermic
BNT-BT-KNN-0.05CZ	Heating	522	Endothermic
BNT-BT-KNN-0.05CZ	Cooling	119	Endothermic
BNT-BT-KNN-0.05CZ	Cooling	253	Endothermic*
BNT-BT-KNN-0.05CZ	Cooling	508	Exothermic
BNT-BT-KNN-0.15CZ	Heating	42	Endothermic
BNT-BT-KNN-0.15CZ	Heating	402	Endothermic
BNT-BT-KNN-0.15CZ	Heating	533	Endothermic
BNT-BT-KNN-0.15CZ	Cooling	135	Endothermic
BNT-BT-KNN-0.15CZ	Cooling	509	Exothermic

Table 3: Endothermic and exothermic peaks observed in the DSC measurement of the BNT-BT-0.05CZ, BNT-BT-0.15CZ, BNT-BT-KNN-0.5CZ and BNT-BT-KNN-0.15CZ samples. *Note that this is not actually one peak but an endothermic peak followed by an exothermic peak in less than 2 ºC temperature range.

For the BNT-BT-CZ and BNT-BT-KNN-CZ systems, it is expected that at sufficient high-temperatures, thermal fluctuations are so large that no well-defined dipole moments are present. However, on cooling, these dipolar entities manifest themselves at a temperature normally called Burns or dipolar temperature (T_B). It is expected that the endothermic peaks on heating and exothermic on cooling present in all the materials at temperatures higher than 500 ºC correspond to the described phenomenon occurring at T_B.

In a first sight, the endothermic peaks at low-temperatures (appearing between 35 and 50 ºC in all the samples on heating) may be associated with adsorbed water that evaporates during heating. Nevertheless, this must be discarded since no weight loss was observed during the heating or cooling cycles. Taking into account the relaxor behavior observed in the ε_r and tan(δ) (Section 5.2.1), it may be assumed that a kinetic-dependent rearrangement of atoms is occurring at these low-temperatures. At such low-temperatures, it is expected (such as in a glass transition) that the time-scale of the relaxation processes are comparable with the time scale of the experiment. Therefore, a defreezing process from a non-ergodic to an ergodic state may be related to a strong broadening of the relaxation time spectrum of the nanopolar regions in the material whose mean extends into the regime of macroscopic times. This is expected to be happening at this low-temperatures (which will be called T_f) for all the materials developed. Thus the total heat flow from the sample at any moment would be the superposition of the heat flows from all the subsystems at this temperature. In other words, this peak is expected to be the superposition of the atoms defreezing in each nanopolar region of the material. At this temperature, in a relaxor material short-range interactions between the nanopolar regions control the kinetics of the polarization fluctuations and thus the mentioned defreezing/freezing process. An implication of the relaxation at temperatures below T_f is that the system may freeze into a state which has nonequilibrium characteristics such as time-depedent order parameters. Nevertheless, in order to confirm this kinetic-controlled behavior and to corroborate if this hypothesis is correct, future investigations should be done modifying the thermal history of the samples. Furthermore, taking into account all the mentioned characteristics T_f may be associated with a glass-like transformation due to many reasons:

- It can be assumed that the system passes through a sequence of non-equilibrium states during heating through this temperature. The typical asymmetric shape of a glass transition curve (an extensive tail on the low-temperature side and a fairly abrupt end at high-temperatures) such as the one observed, is due to a distribution of the intrinsic variables which defreeze/freeze over a wide temperature range (such as with a size distribution of nanopolar regions).
- In the developed materials the glass-like phase transition presents a diffuse broad peak with a so called enthalpy relaxation peak. This event appears normally on glass transitions on heating curves as endothermic events (such as the peak observed) at the high-temperature end of the glass transition range (as observed). This peak is produced because the superheating from the glass state (or in the case of the present materials a presumed non-ergodic relaxor state with coexistence of two different

nanopolar regions) to the liquid state (or in the case of the present materials an ergodic relaxor state with two different nanopolar regions, Section 5.2.1) ends only at temperatures well above T_g, the return to the equilibrium after this point is rapid and produces the so-called relaxation peak. The reason for the superheating effect is the drastically decreased mobility in the glassy or non-ergodic relaxor state present at the low-temperature side of the transition.

- It can be seen that there is change in the heat capacity of the sample at temperatures below and above T_f, such as in the case of a glass transition around T_g.

It should be mentioned that if these low-temperature peaks are compared to the anomalies appearing at the ε_r and tan(δ), they all appear at different temperatures (Section 5.2.1). Nevertheless, it should not be discarded that the same physical phenomenon is occurring at different temperatures in both measurements. Discrepancies may be caused by the different influences of the particular technique on the relaxation of the intrinsic variables. The principal differences must be attributed to different interactions between the method in question and the relaxation time spectrum of the intrinsic variables (note that one technique is thermal, while the other is electrical). Moreover, a far superior heating rate was employed for the DSC measurement compared to that used in the ε_r and tan(δ) measurements. Therefore, since the defreezing/freezing is a kinetic controlled transformation a discrepancy with thermal history and heating rate would also be expected [109-112].

The exothermic peaks observed for the BNT-BT-CZ system on heating at around 365 ºC may be associated with the change in symmetry of some of the nanopolar regions from rhombohedral *R3C* to tetragonal *P4bm* (since only at temperatures below is expected that the *R3C* nanopolar regions are stable [108]). On the other hand, long-range structural changes cannot be discarded at the exothermic peak appearing at around 400 ºC in the BNT-BT-KNN-0.05CZ sample, which may be correlated with some literature results [2]. Nevertheless, further investigation should be done in order to understand the complex BNT-BT-KNN-CZ system.

On cooling, the BNT-BT-0.05CZ and BNT-BT-KNN-0.05CZ samples presented a complex peak, which is composed of an endothermic response at the higher temperature side and an exothermic peak at the lower temperature part. The endothermic peak may be correlated with the thermal evolution of the *P4bm* nanopolar regions, while the exothermic peak may be associated with the change in symmetry of some of the *P4bm* nanopolar regions to the mentioned *R3C* ones. This last assumption may be done specifically for the samples with low CZ content (the peaks are appearing only for the 5% CZ samples), since it is expected that the nanopolar regions stability is increased with lower CZ content (Section 5.2.1). If this is true then a second anomaly on cooling may be expected at lower temperatures due to the thermal evolution of the *R3C* nanopolar regions nucleated (presumably appearing also with a second thermal evolution of the *P4bm* nanopolar regions). Indeed, with further cooling at around 130 ºC an endothermic peak is observed for all the samples at around 134 ºC (except for the BNT-BT-KNN-0.05CZ in which it appears at around 119 ºC). Note that all the peaks on cooling marked a change in the specific heat of the samples.

A thermal hysteresis is observed if the different characteristic temperatures on heating are compared to that appearing on cooling. A thermal hysteresis was also reported in literature in other glass-like ferroelectric materials, so this phenomenon should not be discarded [112]. Moreover, it should be considered that the thermal history of the materials was changed if the heating (annealed state) is compared to the cooling measurements. This may also influence the temperature of the peaks observed. Nevertheless, further investigation must be done in order to corroborate the last hypotheses.

5.1.3 Density measurements

The main purpose of this study was to obtain the relative density of the samples (ratio between the measured density and the theoretical density of the material) and its tendency with increasing CZ content and sintering temperature. These results were obtained taking into account the peak positions obtained in the XRD patterns, Bragg’s Law and considering a cubic unit-cell.

Material	Sintering temperature (°C)	Relative Density (%)
BNT-BT-0.05CZ	1100	97
BNT-BT-0.1CZ	1100	84
BNT-BT-0.15CZ	1100	97
BNT-BT-0.15CZ	1150	98
BNT-BT-0.2CZ	1100	98
BNT-BT-0.2CZ	1150	96
BNT-BT-0.2CZ	1200	96
BNT-BT-KNN-0.05CZ	1100	96
BNT-BT-KNN-0.1CZ	1100	96
BNT-BT-KNN-0.15CZ	1100	97
BNT-BT-KNN-0.2CZ	1100	99

Table 4: Relative densities obtained for the BNT-BT-CZ and BNT-BT-KNN-CZ systems. Note that the BNT-BT-0.1CZ sample presents a lower relative density than all the other samples. This is in agreement with the HREM results.

From Table 4 it can be observed that there is no clear tendency in the density with increasing CZ or increasing sintering temperature, neither in the BNT-BT-CZ nor the BNT-BT-KNN-CZ systems. It should also be highlighted that the BNT-BT-0.1CZ sample presents a relative density of 84%. All the other samples present relative densities above 96%.

5.1.4 High-resolution electron microscopy

The microstructures of the BNT-BT-CZ and BNT-BT-KNN-CZ systems are presented in Figure 32 to Figure 35. For the BNT-BT-CZ system there is no clear tendency in the samples porosity with increasing CZ doping (Figure 32). Nevertheless, it should be highlighted that the samples with 5 and 10% CZ presented a higher porosity than the ones with 15 and 20% CZ. The sample with 10% CZ presented the highest porosity, a result which is in agreement with the density measurements (Table 4). Note that in the sample with 15% CZ a minor superficial contamination can be observed probably due to the thermal etching atmosphere. From Figure 33, it is observed that all the samples present a bimodal distribution of grain sizes with no clear tendency in the grain size with increasing CZ doping.

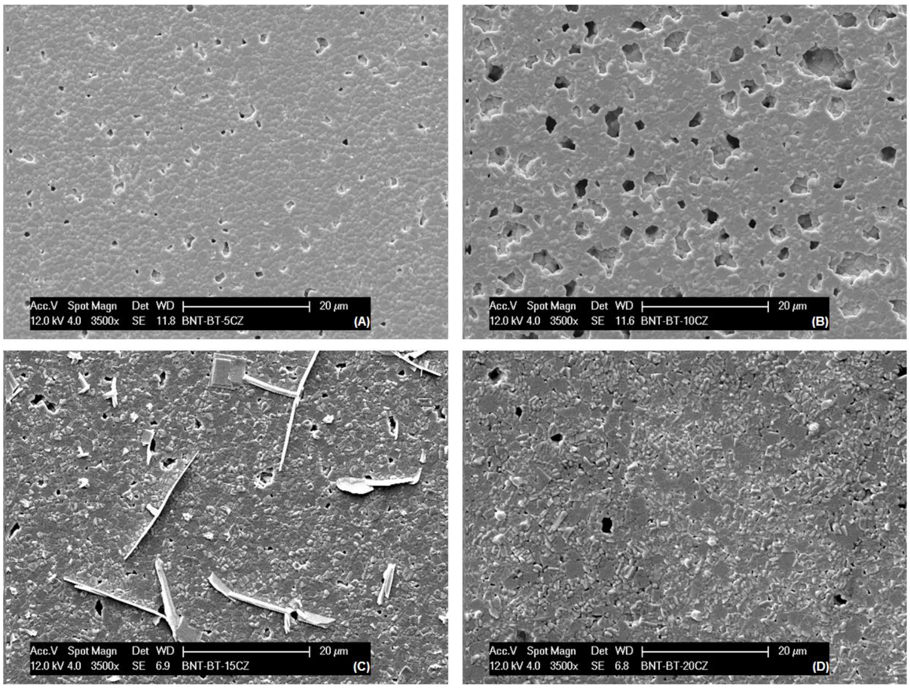

Figure 32:Microstructures of: (A) BNT-BT-0.05CZ, (B) BNT-BT-0.1CZ , (C) BNT-BT-0.15CZ and (D) BNT-BT-0.2CZ. No clear tendency in the porosity with increasing CZ doping is observed.

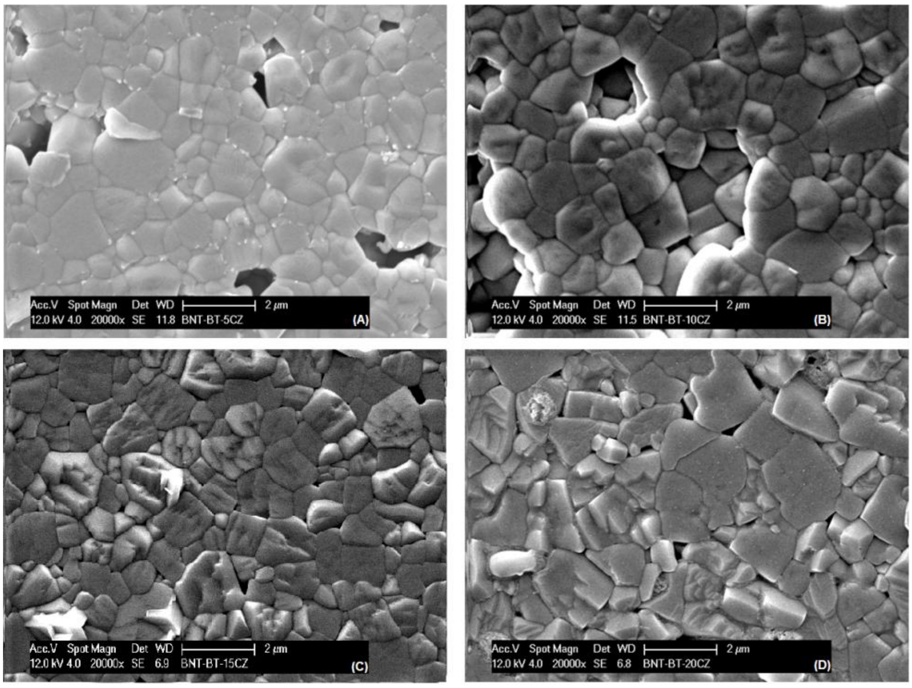

Figure 33: Detailed microstructures of: (A) BNT-BT-0.05CZ, (B) BNT-BT-0.1CZ, (C) BNT-BT-0.15CZ and (D) BNT-BT-0.2CZ. A bimodal grain size distribution with no clear tendency in the grain size with increasing CZ doping is observed.

On the other hand, it can be seen that in the BNT-BT-KNN-CZ system the porosity is reduced (Figure 34), while the grain size is increased (Figure 35) with increasing CZ doping. Moreover, as in the BNT-BT-CZ system, a bimodal grain size is observed (Figure 35).

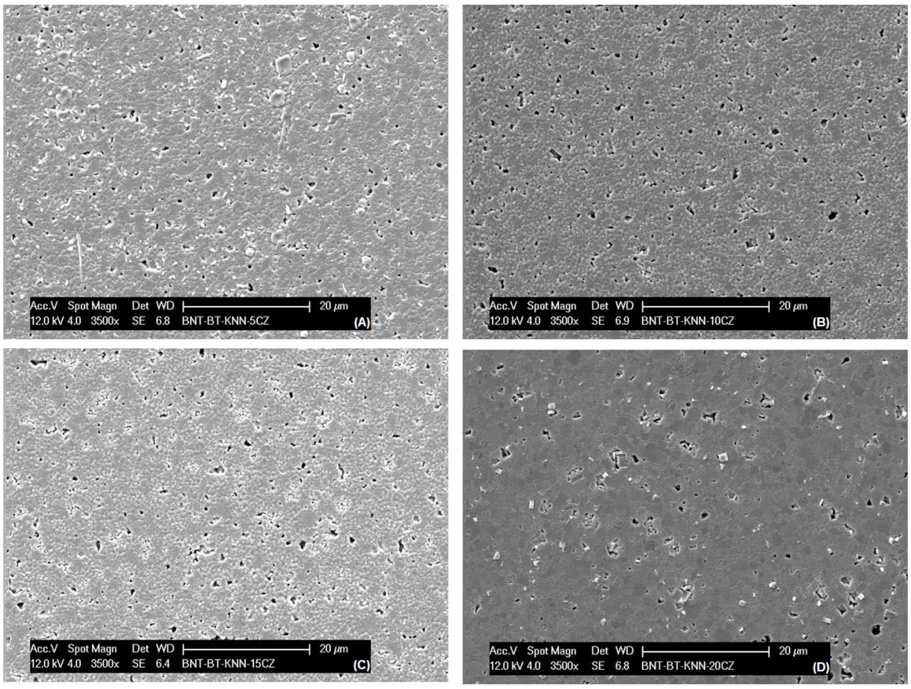

Figure 34: Microstructures of: (A) BNT-BT-KNN-0.05CZ, (B) BNT-BT-KNN -0.1CZ, (C) BNT-BT-KNN-0.15CZ and (D) BNT-BT-KNN-0.2CZ. A decrease in the porosity with increasing CZ doping is observed.

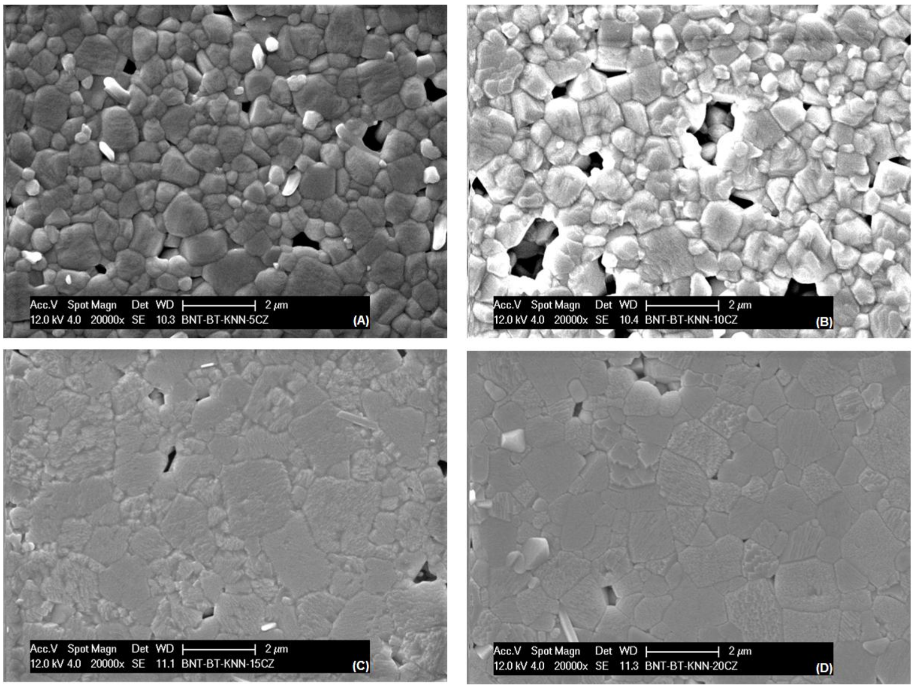

Figure 35: Detailed microstructures of: (A) BNT-BT-KNN-0.05CZ, (B) BNT-BT-KNN-0.1CZ, (C) BNT-BT-KNN-0.15CZ and (D) BNT-BT-KNN-0.2CZ. An increase in grain size and a bimodal grain size distribution with increasing CZ doping is observed.

5.2 Electrical characterization

5.2.1 Temperature and frequency dependent relative permittivity and losses

The low and high-temperature frequency dependent ε_r and tan(δ) for the BNT-BT-CZ system are observed in Figure 36 and Figure 37, respectively. Note that for the 15 and 20% CZ doped samples there is a significant increase in both ε_r and tan(δ) at high-temperatures. This phenomenon is due to a high-conductivity and space charge accumulation in interfaces (such as electrode-ceramic); therefore, it should not be confused with an intrinsic material property (Section 5.2.2 for further details).

A diffuse anomaly may be observed in all the samples at temperatures between room temperature and 60 ºC in both ε_r and tan(δ). For the 5% CZ sample this anomaly can be seen in the imaginary part of the ε_r (inset Figure 38) at around T_f = 23 ºC[10]. For this sample two more anomalies are observed (Figure 38). The first one is at around T_1= 120 ºC, while the second one at high-temperature is observed at around T_2=380 ºC. The anomalies present a frequency dispersion, but with different tendency. The anomaly appearing at T_f is a concave peak which is decreased with increasing frequency. Therefore, its diffuseness increases with increasing frequency resulting in an almost not observable peak at 1 MHz. The peak at T_1 is increased with increasing frequency, while the one at T_2 is decreased. Furthermore, the three peaks are shifted to higher temperatures with increasing frequency and are rather broad; in other words all the peaks present relaxor-like features.

In perovskite materials substituting ions of different sizes, valences and polarizabilities at both the A and B lattice sites (such as the developed materials) may introduce sufficiently high degree of disorder so as to break the translational symmetry and prevent the formation of a long-range ferroelectric ordered state even at low-temperatures. Moreover, in highly polarizable materials such as BNT-BT, the presence of defects or statistically random lattice site occupation can induce dipoles in a unit-cell at temperatures below T_B. At temperatures sufficiently above T_m and below T_B, it is expected that the dipoles that exist in the material will behave themselves as almost independent, *i.e.* as an ideal noninteracting population of dipoles. With further cooling,

---

[10] Note that all the anomalies are measured for convenience in the imaginary part of the ε_r at 1 kHz.

the polarization fluctuation would be reduced (far below the Debye frequency of the material); therefore, each dipolar entity will induce polarization in adjoining unit-cells of its host lattice. With further cooling, this dynamic polarization cloud whose extent is determined by the correlation length of dipolar fluctuations, would lead to the formation of dynamic small nanopolar regions which would result in an ergodic relaxor [110]. This is assumed to happen in the BNT-BT-CZ system. It is expected that these nanopolar regions would have a distribution of sizes and thus correlation lengths. Therefore, with further cooling a thermal evolution (slowing down of dipolar fluctuations) of the nanopolar regions will result in a broad frequency dependent anomaly in the ε_r, such as the peak at T_2. Taking into account recent results in literature [108] and the high-temperature of this anomaly it is expected that this thermal evolution is associated with tetragonal *P4bm* nanopolar regions. Moreover, this peak presents an asymmetric shape, with an increased higher temperature side which may indicate that this peak actually corresponds to a convolution of two different phenomena. Therefore, it is expected that this peak also reflects the change in symmetry of some of the *P4bm* nanopolar regions to rhombohedral *R3C* ones [108]. Moreover, since the presence of *R3C* nanopolar regions is expected, a thermal evolution of them (it should not be discarded that a second thermal evolution of the *P4bm* nanopolar regions is also taking place) may be associated with the peak observed at T_1. In this context, it should be mentioned that an ergodic relaxor material (such as the one described) transforms to a non-ergodic one at the freezing/defreezing temperature (for cooling and heating, respectively). It is assumed that this phenomenon is taking place at the temperature previously called T_f [111] [112]. The broadness of all the mentioned anomalies may indicate a distribution of correlation lengths (and thus of response times) of the nanopolar regions.

At this stage is interesting to mention the reasons why the anomalies observed may not be associated with a phase transformation for example from an antiferroelectric to a ferroelectric state such as in some literature reports for BNT-BT based materials [70] [91]. One reason that indicate that nanopolar regions exist in the material is that no presence of changes in the cubic symmetry with increasing CZ doping (from X-ray measurements, Section 5.1.1) or even with increasing temperature (from DSC measurements, Section 5.1.2) are observed. The presence at room temperature of ferroelectricity confirmed by the polarization measurements (Section 5.2.3) may be associated with a distortion of the cubic matrix resulting in ferroelectricity (*i.e.* a transformation of an ergodic relaxor material to a ferroelectric one) or with the presence of nanopolar regions (stabilized due to the $\mathbf{E_0}$) in a cubic and therefore non-polar matrix. The former assumption should be discarded since the ε_r of the poled samples did not change after poling (not shown). It may also be assumed that the nanopolar regions may be induced in this last measurement due to the $\mathbf{E_0}$. If this was true, they would not be expected in the unpoled samples. Nevertheless, taking into account the frequency dependent anomalies observed in the ε_r and tan(δ) of all the samples, their presence may be also inferred. Moreover, in the imaginary part of the ε_r three frequency dependent thermal hysteresis loops from 40 to 92 ºC, 92 to 212 ºC and 212 ºC to higher temperatures (it was not possible to measure the high-temperature limit due to the operational range of the machine used) were measured for the 5% CZ sample (Figure 39). Some literature results agree that a thermal hysteresis may be related with the presence of nanopolar regions, their different time responses and thermal stability [113] [114]. For this reason, the crossing temperature around 40 ºC is expected to be related with transformation of the material from a non-ergodic to an ergodic response. The other two crossing temperatures may be related to the thermal evolution of the nanopolar regions of the material and also may reflect the change in symmetry of the *P4bm* nanopolar regions to *R3C* ones. Nevertheless, further investigation should be done in order to confirm the lasts hypotheses.

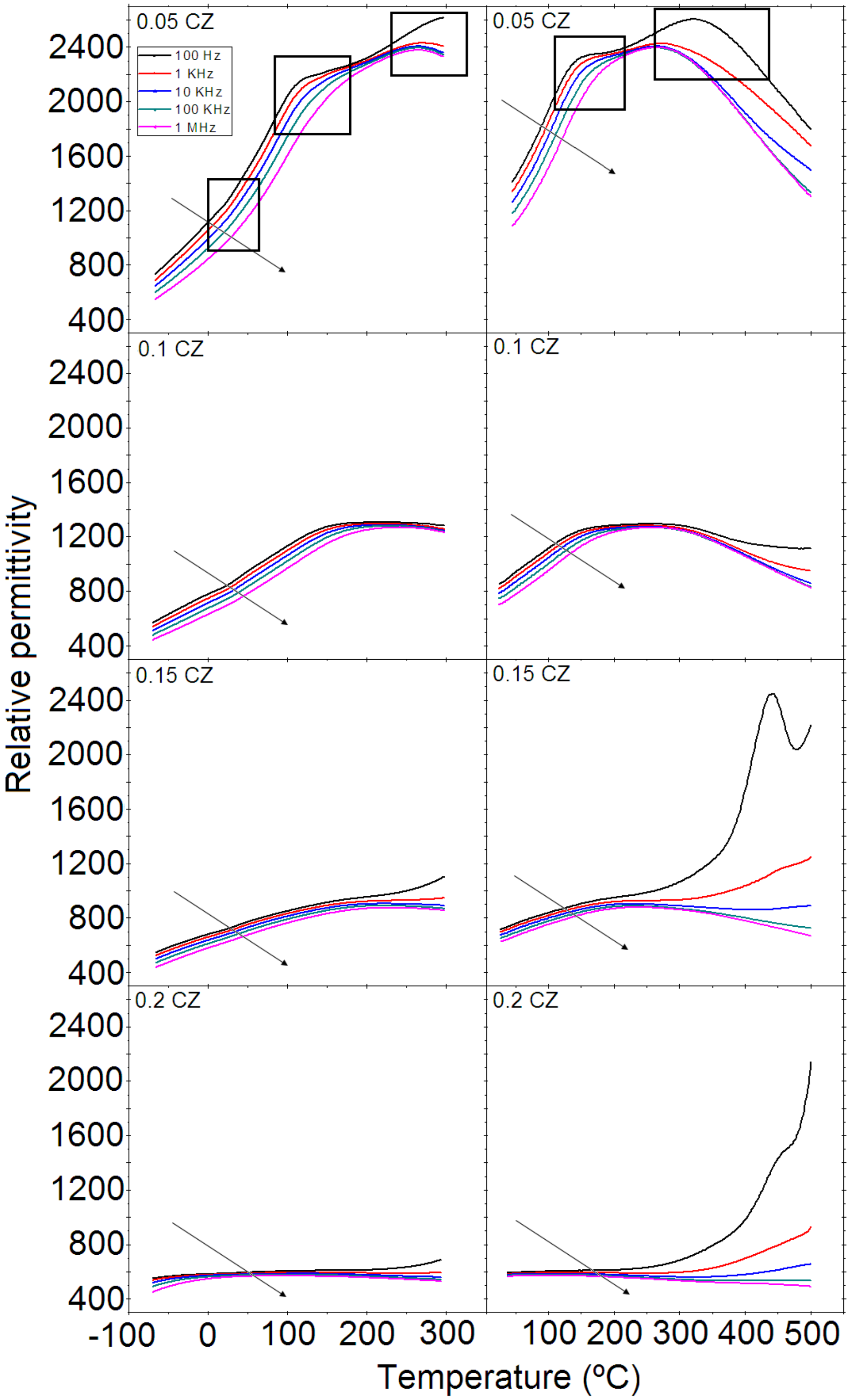

Figure 36: Relative permittivity vs. low (left) and high (right) temperatures measured at frequencies from 100 Hz to 1 MHz for the BNT-BT-CZ system. Note that the anomalies for the 5% CZ sample are marked.

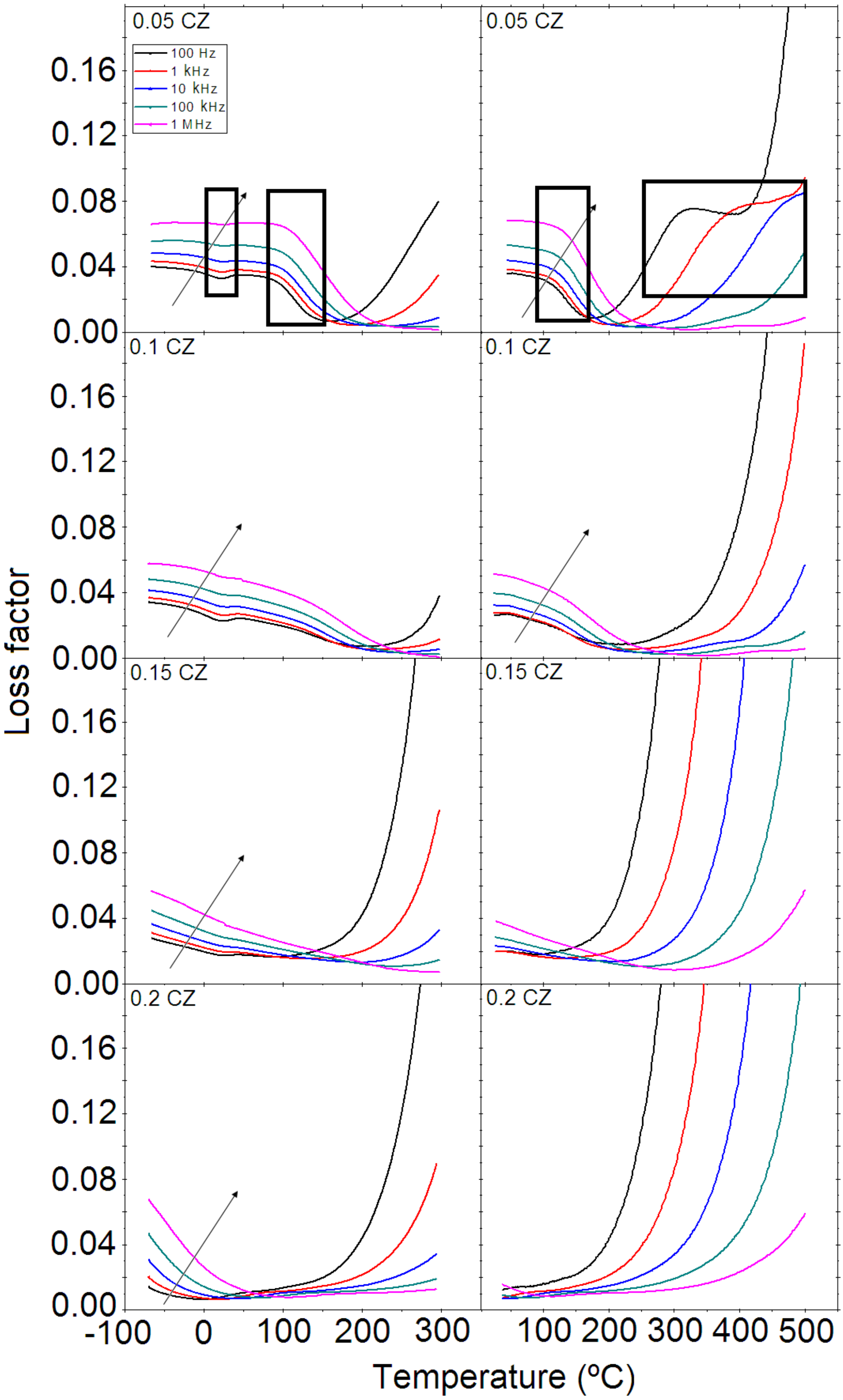

Figure 37: Loss factor vs. low (left) and high (right) temperatures measured at frequencies from 100 Hz to 1 MHz for the BNT-BT-CZ system. Note that the anomalies for the 5% CZ sample are marked.

It should also be mentioned that the dielectricity and ferroelectricity of the system is decreased significantly with increasing CZ doping (Figure 46 and Figure 55, respectively). This would indicate that the CZ stabilizes the non-polar cubic matrix (or almost non-polar similar to others described in literature [79] [104]), thus resulting in nanopolar regions of smaller sizes. This would frustrate almost totally the correlation of the nanopolar regions present in the material, thus resulting in a totally random orientation of the dipoles after the $\mathbf{E_0}$ is removed in the polarization measurements. This would indicate that a slim ferroelectric loop with almost no $\mathbf{P_r}$ is expected for high contents of CZ. Indeed, this is observed in Figure 55. Moreover, if this hypothesis is assumed to be correct, the presence of a relaxor behavior (due to a thermal evolution) would be expected at even lower temperatures for the 20% CZ sample, since the lower the temperature the more stable the nanopolar regions and the bigger their sizes and correlation lengths. This was confirmed in a low-temperature frequency dependent ε_r measurement (Figure 40).

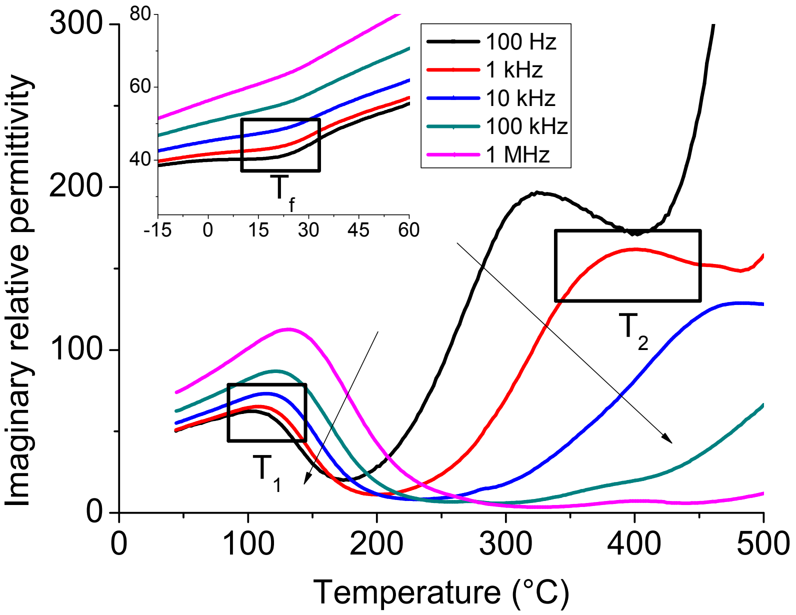

Figure 38: Imaginary relative permittivity vs. temperature for the BNT-BT-0.05CZ sample. Note that two anomalies with relaxor features are clearly seen at T_1= 120 ºC and T_2= 380 ºC. Moreover, a diffuse frequency dependent third anomaly may be observed in the inset at around T_f=23 ºC. All the anomalies were measured at 1 kHz.

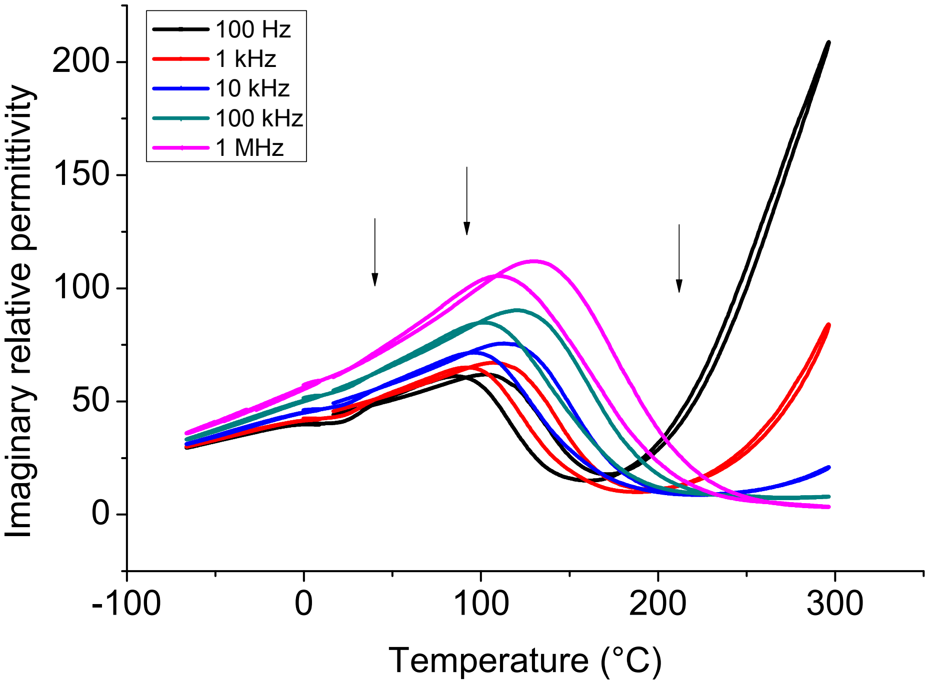

Figure 39: Imaginary relative permittivity vs. temperature for the BNT-BT-0.05CZ sample. Three frequency dependent thermal hysteresis loops from 40 to 92 ºC, 92 to 212 ºC and 212 ºC to higher temperatures than measured are observed (the crossing temperatures were measured at 1 kHz and are marked with arrows). They may be related with the presence of nanopolar regions, their different time response and thermal stability.

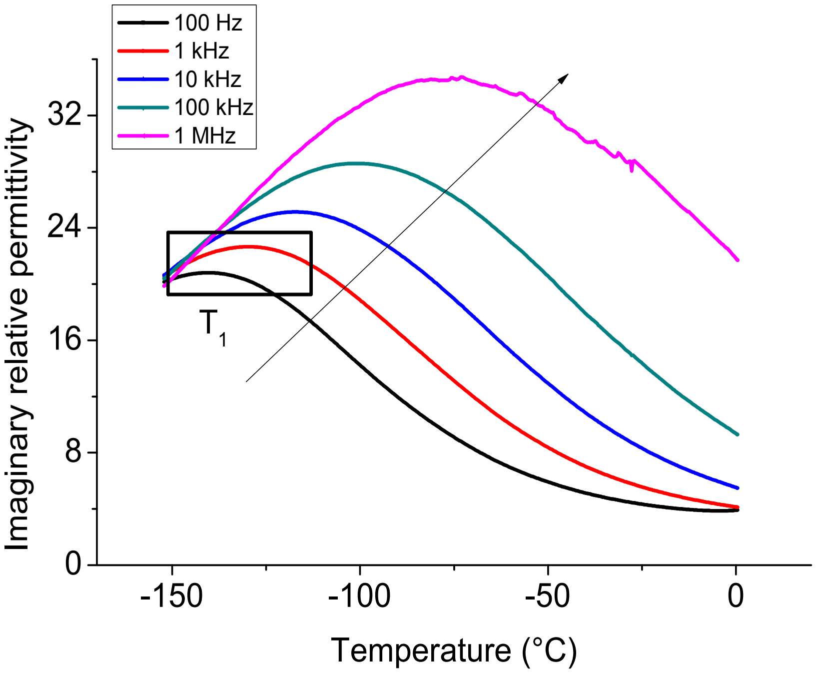

Figure 40: Imaginary relative permittivity vs. temperature for the BNT-BT-0.2CZ sample. Note that that the anomaly at T_1 can be observed but at lower temperatures, in this case T_1= -130 ºC, measured at 1 kHz.

The effect of different sintering temperatures was studied for the BNT-BT-0.15CZ and BNT-BT-0.2CZ samples (Figure 41). This was done in order to suppress the second phases observed in the XRD patterns of the 1100 ºC sintered samples (Figure 25). Note that for a given composition and sintering temperature above 1100 ºC the ε_r is overall increased compared to that measured in the 1100 ºC sintered sample (Figure 41).

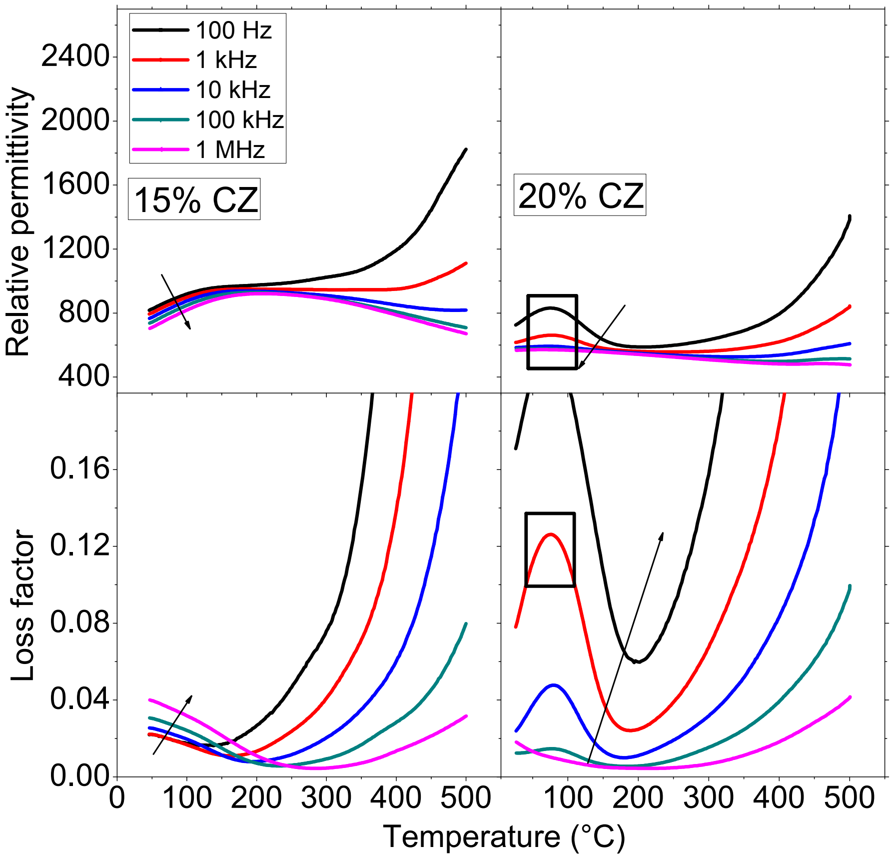

Figure 41: Effect of the 1150 ºC and 1200 ºC sintering temperatures in the BNT-BT-0.15CZ and BNT-BT-0.2CZ samples, respectively. Note that the relative permittivity is increased compared to that of the samples sintered at 1100 ºC.

In the case of the 20% CZ doped sample sintered at 1200 ºC, the anomaly at T_1 is only observable at low frequencies and no presence of frequency dispersion with temperature is observed (marked in the ε_r and tan(δ)). This may be attributed to a bigger size (since no anomaly is observed for the high-frequencies) and narrow size distribution (since no frequency dispersion is observed) of nanopolar regions in the material. Nevertheless, this hypothesis should be confirmed with further investigation in transmission electron microscopy.

The low and high-temperature frequency dependent ε_r and tan(δ) for the BNT-BT-KNN-CZ system can be observed in Figure 42 and Figure 43, respectively.

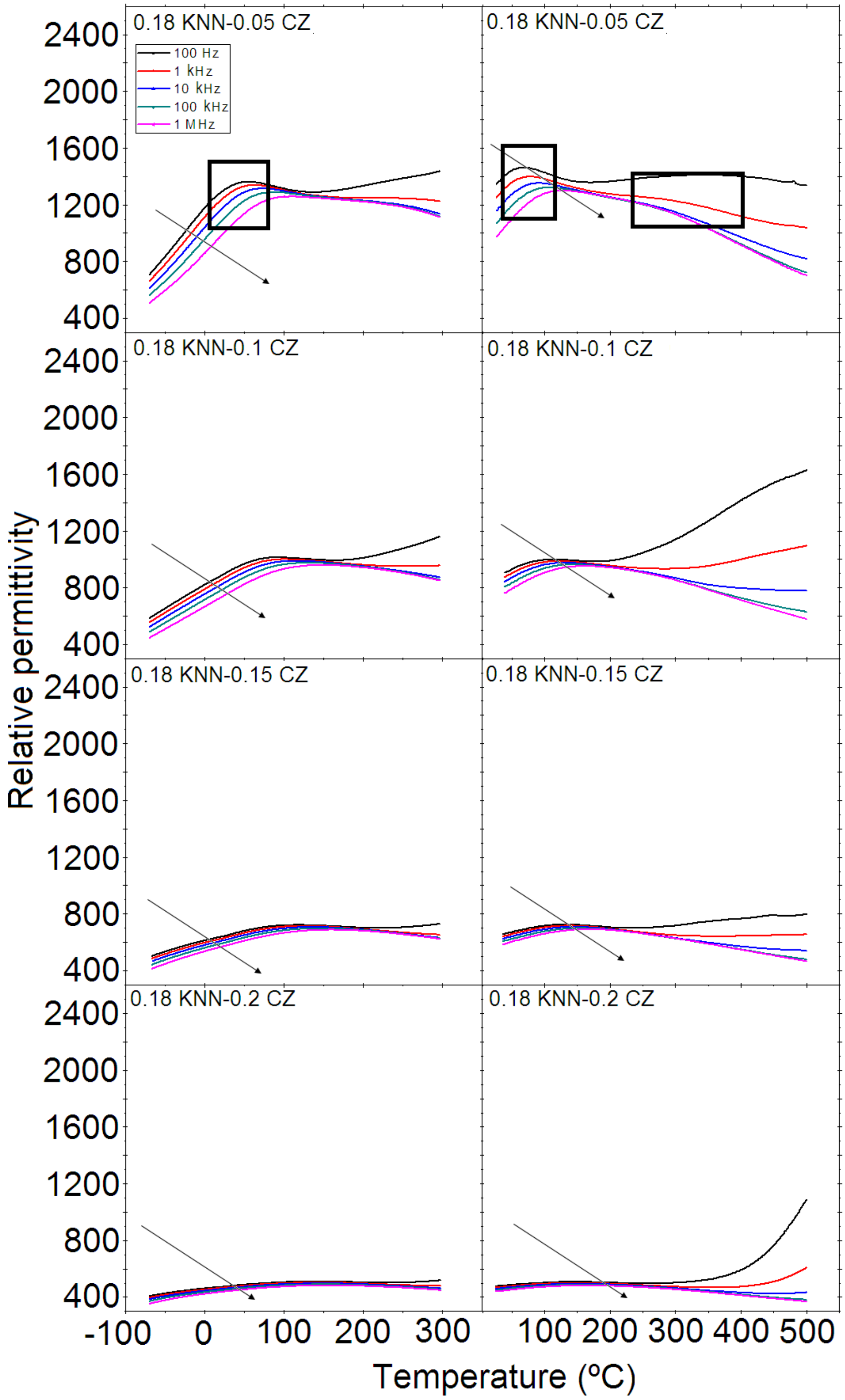

Figure 42: Relative permittivity vs. low (left) and high (right) temperatures measured at frequencies from 100 Hz to 1 MHz for the BNT-BT-KNN-CZ system. Note that the anomalies for the 5% CZ sample are marked.

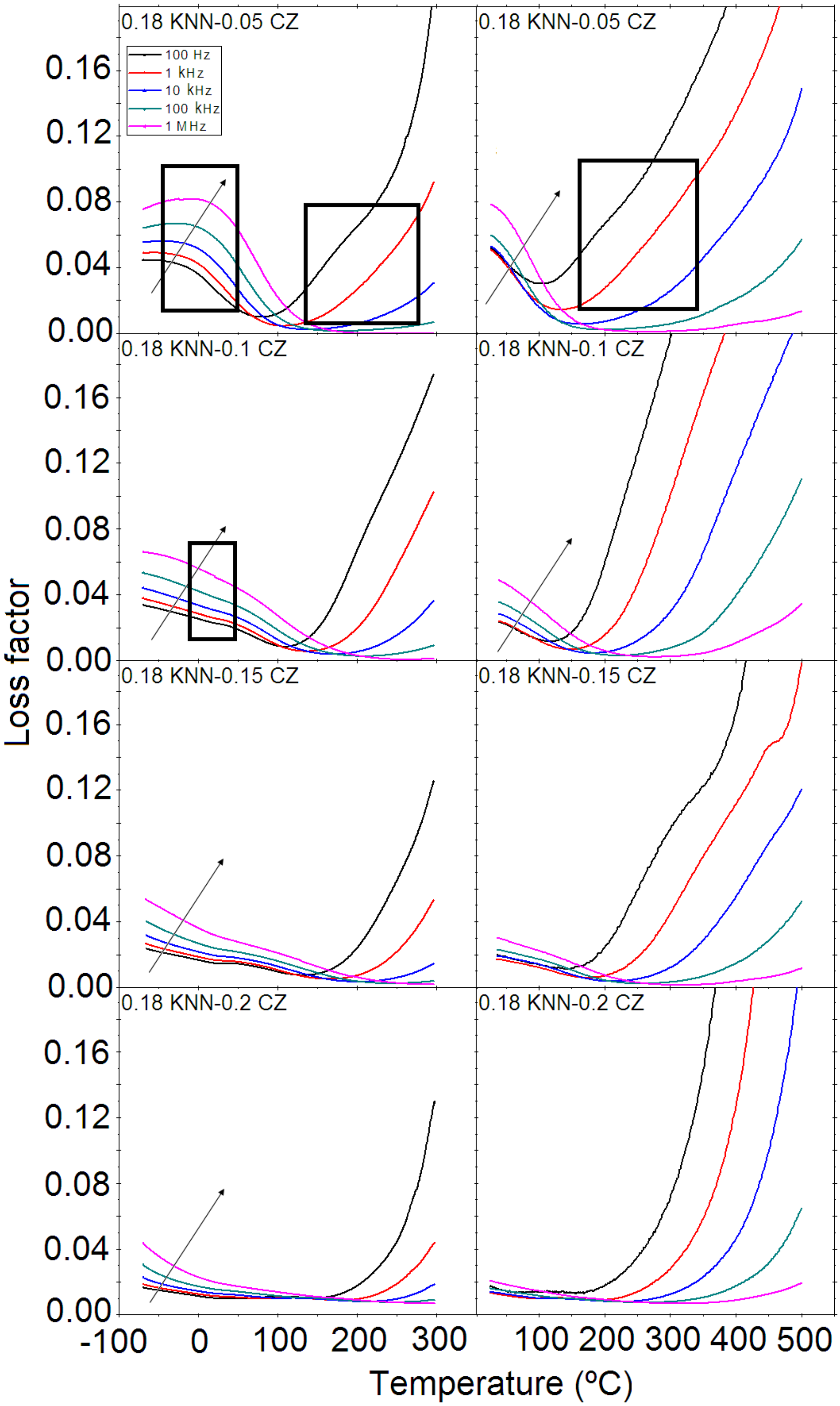

Figure 43: Loss factor vs. low (left) and high (right) temperatures measured at frequencies from 100 Hz to 1 MHz for the BNT-BT-KNN-CZ system. The anomalies at T_1 and T_2 for the 5% CZ sample are marked; while for the 10% CZ sample the one at T_f is marked.

At high-temperatures, tan(δ) is increased significantly for all the samples. As mentioned before this phenomenon is due to a high-conductivity and space charge accumulation (Section 5.2.2 for further details). For the 5% CZ doped sample two anomalies are observed at the imaginary part of the ε_r (Figure 44). The one appearing at low-temperatures may be associated with the one appearing in the BNT-BT-CZ system at T_1, since it presents the same behavior with increasing frequency. The one appearing at high-temperatures is rather smooth and almost not observable at high-frequencies. Nevertheless, in the inset of Figure 44 a change in the curvature of the 100 Hz curve is observed. This change is also appearing at the same temperature where the change in the frequency tendency is appearing, thus resulting in a similar behavior with frequency as the anomaly observed for the BNT-BT-CZ system at T_2. In this case the anomalies appear at T_1= 15 ºC and T_2= 180 ºC. Nevertheless, it should be highlighted that due to the diffuse shape of the second anomaly its temperature cannot be measured accurately. Note that the anomaly observed at T_f is not observable in this sample. Nevertheless, this anomaly is observed clearly at around T_f = 26 ºC for the 10% CZ sample (Figure 43). Therefore, it can be assumed that the anomaly present at T_1 for the 5% CZ sample is actually a convolution of the defreezing temperature and thermal evolution of the nanopolar regions of the material. Two frequency dependent thermal hysteresis were also observed in the temperature ranges from 10 to 130 ºC and from 130 ºC to higher temperatures (Figure 45). Due to the lower T_1 and T_2 temperatures observed, it is presumed that the KNN doping has a similar influence as the CZ doping. Therefore, both dopants increase the stability of the non-polar cubic matrix, thus reducing the nanopolar regions size and correlation lengths for a given temperature. Moreover, the KNN doping also introduces even more statistical random compositional changes. This may lead to a broader of sizes of the nanopolar regions in the material, which may be the reason of the broadness of the anomaly observed at T_2. In other words, each of the nanopolar regions is expected to have its own correlation length and thus thermal evolution due to their different sizes. Nevertheless, structural changes were also suggested in literature at temperatures between the anomalies observed [2], which may be correlated to the changes observed in the DSC measurements at high-temperatures (Section 5.2.1). It should also be mentioned that no structural changes were reported at temperatures near T_1 [2]; therefore, the same hypothesis as proposed for the anomaly at T_1 in the BNT-BT-CZ system can also be proposed for this system. Nevertheless, taking into account the complexity of this system, further investigation should be done in order to confirm these hypotheses.

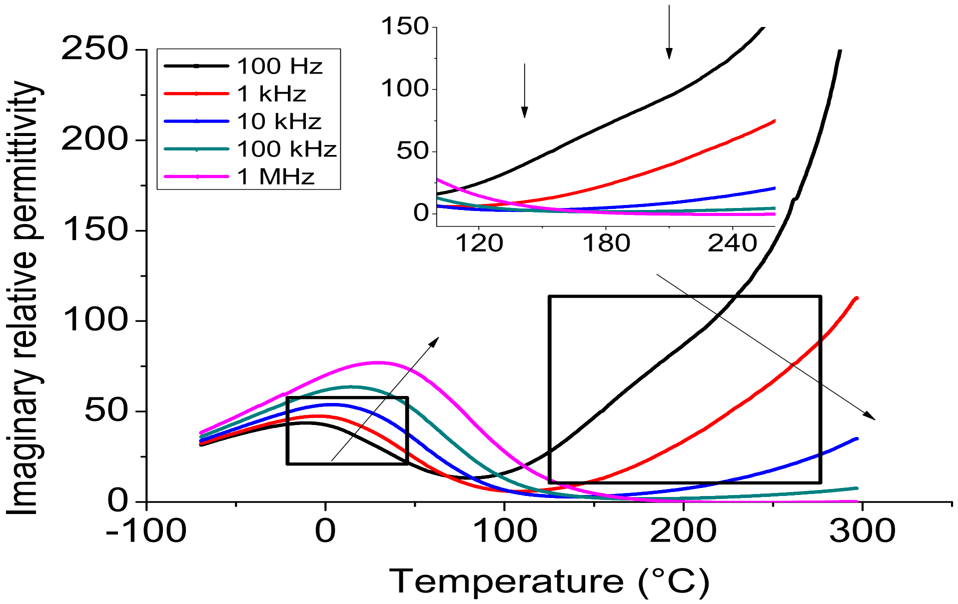

Figure 44: Imaginary relative permittivity vs. temperature for the BNT-BT-KNN-0.05CZ sample. Note that that two anomalies are observed for this system at T_1= 15 °C and T_2= 180 °C, as was reported for the BNT-BT-CZ system. Nevertheless, in this case the anomaly at high-temperatures presents a more diffuse shape and can be seen clearly in the inset at 100 Hz (the arrows mark the change in curvature of the 100 Hz curve).

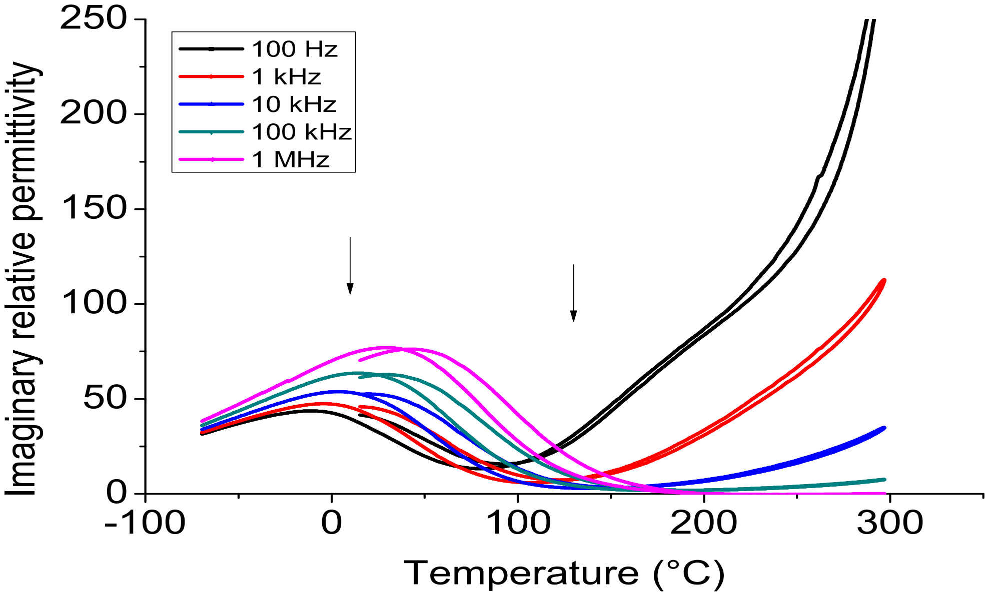

Figure 45: Imaginary relative permittivity vs. temperature for the BNT-BT-KNN-0.05CZ sample. Note the two frequency dependent thermal hysteresis loops observed in the temperature ranges from 10 to 130 °C and from 130 °C to higher temperatures than measured (the crossing temperatures are measured at 1 kHz and marked with arrows).

The effect of CZ doping in the ε_r and tan(δ) was analyzed at a frequency of 1 kHz for the BNT-BT-CZ system (Figure 46 and Figure 47). The anomalies observed in the ε_r and tan(δ) are shifted to lower temperatures with increasing CZ doping, as corroborated in Figure 40; therefore, the ε_r presents a flattened shape with increasing CZ content. It should also be highlighted that the tan(δ) is decreased significantly with increasing CZ doping at low-temperatures. Nevertheless, the tan(δ) is increased at high-temperature which reflects the increased conductivity of the samples (Section 5.2.2 for further details) . Taking into account the significantly reduced ε_r values of the samples with high CZ content, it can be deduced that the CZ is gradually suppressing the dielectricity of the BNT-BT based material. This result was expected due to the lower polarizability of the Ca^{2+} ions compared to that of the Bi^{3+} ions [85].

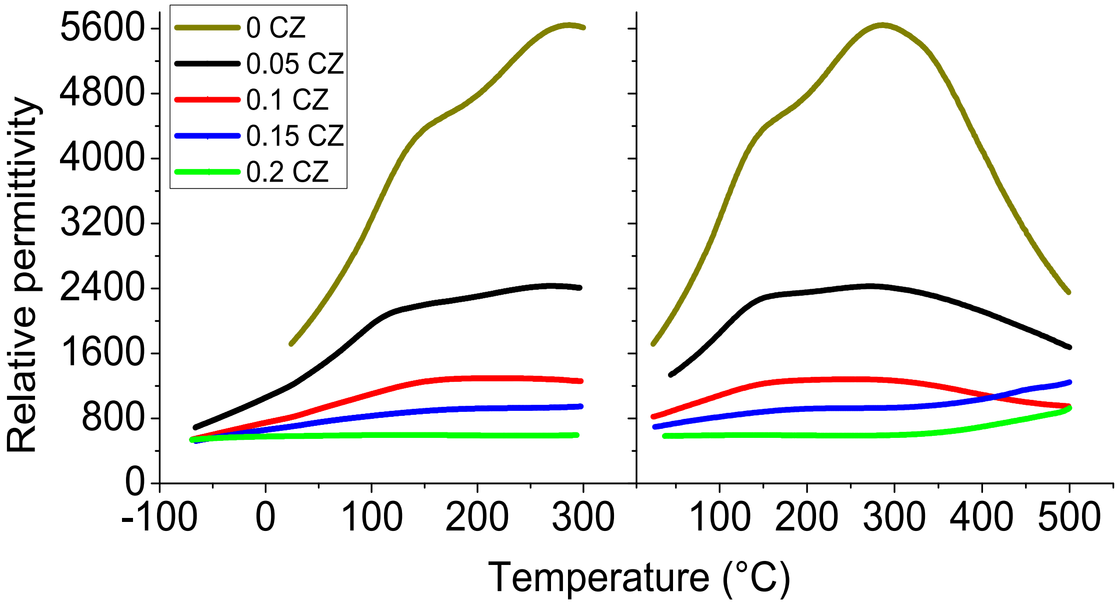

Figure 46: Effect of CZ doping on the relative permittivity of the BNT-BT-CZ system. All the curves correspond to a frequency of 1 kHz. Note the flattened and decreased relative permittivity curves obtained with increasing CZ doping.

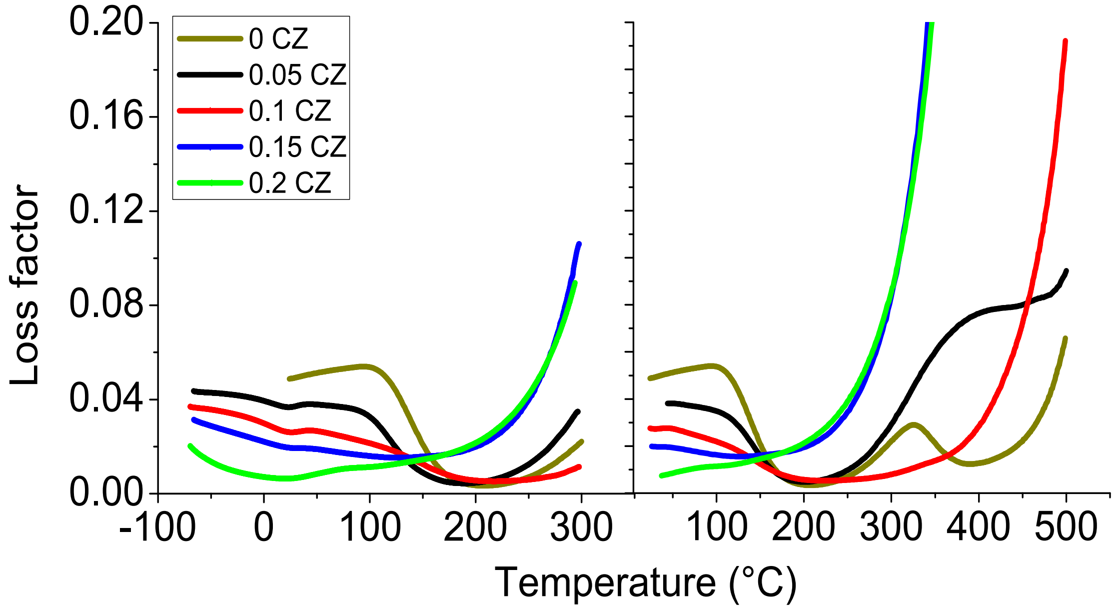

Figure 47: Effect of CZ doping on the loss factor of the BNT-BT-CZ system. All the curves correspond to a frequency of 1 kHz. Note that the low-temperature loss factor is reduced with increasing CZ doping, while the conductivity is increased.

The effect of CZ doping in the ε_r and tan(δ) for BNT-BT-KNN-CZ system was also analyzed at a frequency of 1 kHz (Figure 48 and Figure 49). As mentioned before, a flattened and reduced ε_r curve is observed with increasing CZ content. Moreover, the tan(δ) is decreased significantly with increasing CZ content at low temperatures. Nevertheless, in this case there is not a clear tendency in the tan(δ) at high-temperatures.

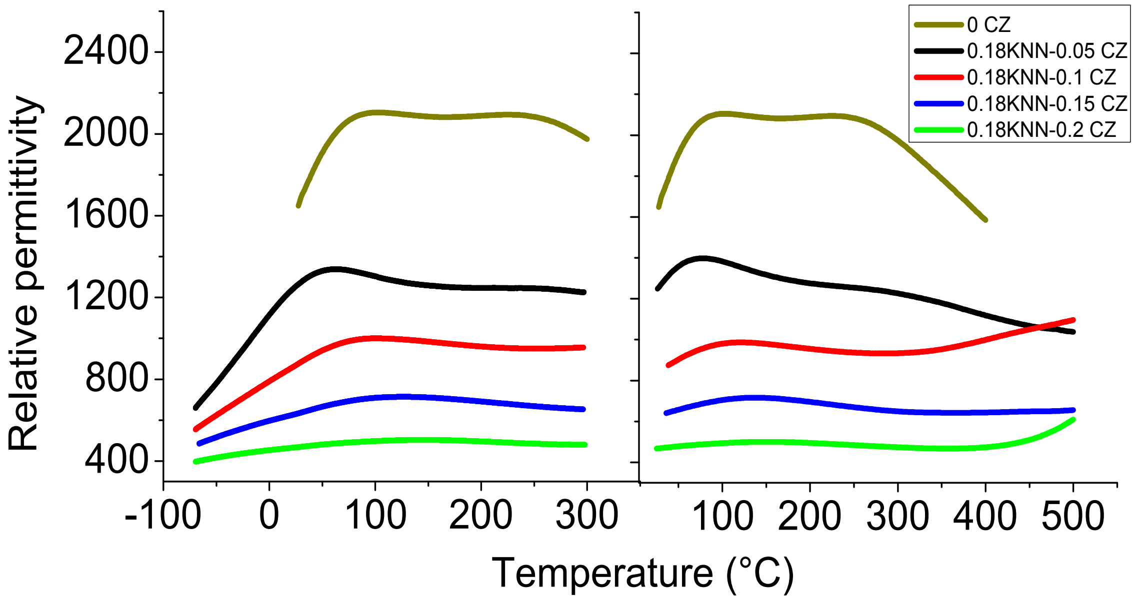

Figure 48: Effect of CZ doping on the relative permittivity of the BNT-BT-KNN-CZ system. All the curves correspond to a frequency of 1 kHz. Note the flattened and decreased relative permittivity curves obtained with increasing CZ doping.

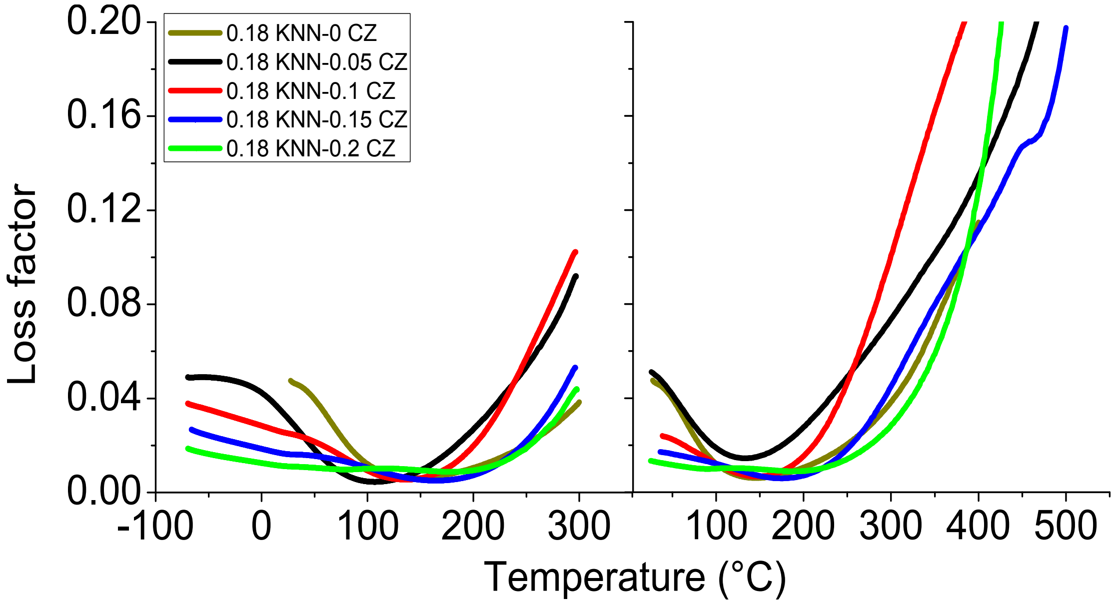

Figure 49: Effect of CZ doping on the loss factor of the BNT-BT-KNN-CZ system. All the curves correspond to a frequency of 1 kHz. Note that the low-temperature loss factor is reduced with increasing CZ doping.

The variation of the ε_r (and capacity) with temperature was analyzed by normalizing the ε_r curves (Figure 50and Figure 51). This was done dividing the ε_r curves at 1kHz (Figure 46 and Figure 48) by the ε_r value measured at 30 ºC and 1kHz.

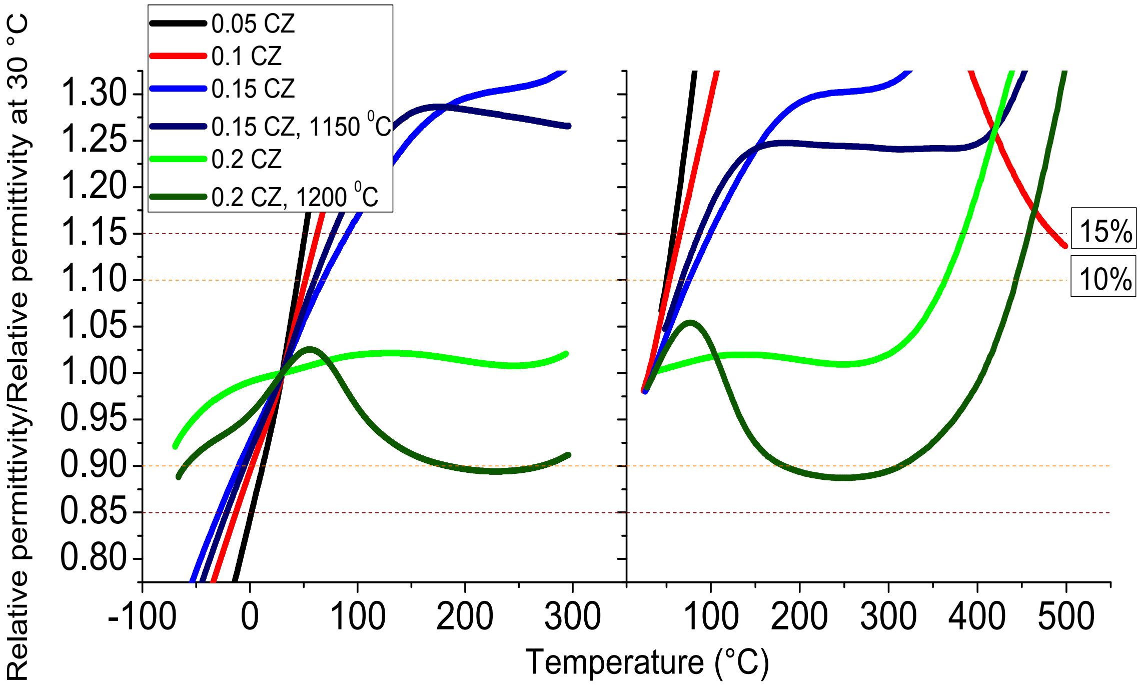

Figure 50: Normalized relative permittivity vs. temperature for the BNT-BT-CZ system. The most promising material for a high-temperature dielectric is the 20% CZ doped one. A working temperature range from below -70 to 385 and 458 ºC within 15% of variation in the relative permittivity is observed for the 20% CZ samples sintered at 1100 and 1200 ºC, respectively.

In the BNT-BT-CZ system the material with most promising properties for high-temperature dielectrics is the one doped with 20% CZ (Figure 50). The 1100 ºC sintered sample presents a working temperature range from below -70 to 365 ºC within 10% of variation in its ε_r and from below -70 to 385 ºC within 15% of variation in its ε_r. The 1200 ºC sintered sample presents a working temperature range from -60 to 443 ºC within 10% of variation in its ε_r (since the crossing temperature at around 185 ºC is almost negligible) and from below -70 to 458 ºC within 15% of variation in its ε_r.

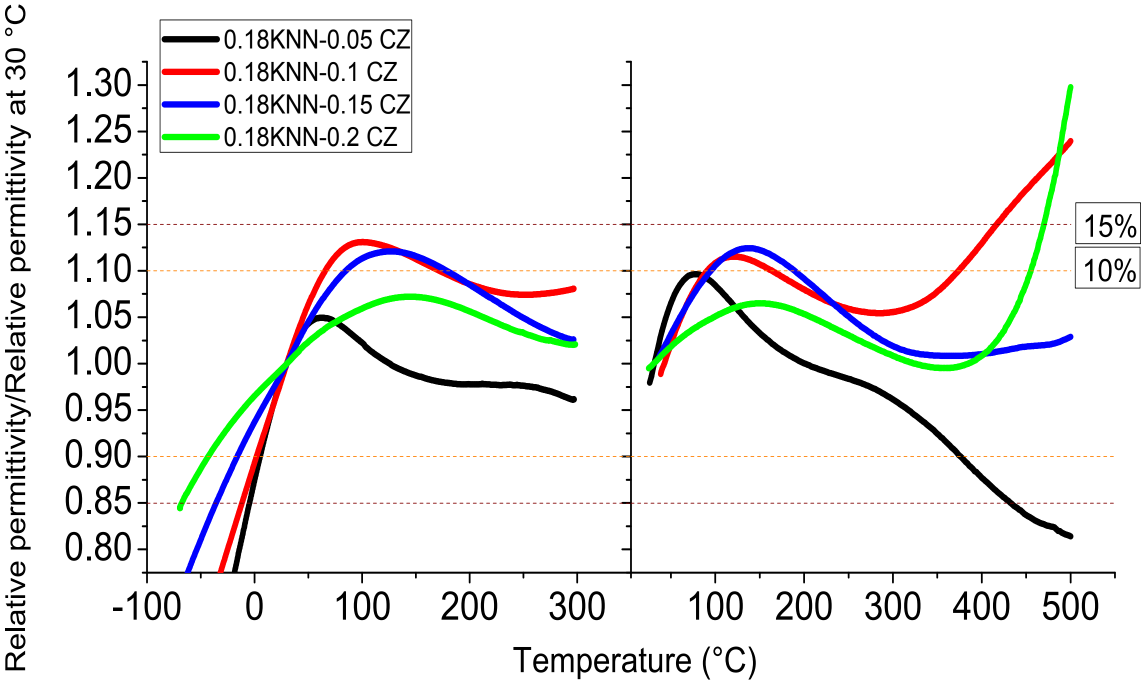

Figure 51: Normalized relative permittivity vs. temperature for the BNT-BT-KNN-CZ system. All the samples present suitable properties for high-temperature dielectrics. Working temperature ranges from below 0 ºC to at least 415 ºC within 15% of variation in the relative permittivity are observed.

In the BNT-BT-KNN-CZ system all the samples present suitable properties for high-temperature dielectrics (Figure 51). The sample doped with 5% CZ presents a working temperature range from 5 to 377 ºC within 10% of variation in its ε_r and from -4 to 435 ºC within 15% of variation in its ε_r. The sample doped with 10% CZ presents a working temperature range from 1 to 374 ºC within 10% of variation in its ε_r (since the crossing at around 90 ºC is almost negligible) and from -12 to 417 ºC within 15% of variation in its ε_r. The sample doped with 15% CZ presents a working temperature range from -16 to above 500 ºC within 10% of variation in its ε_r (since the crossing at around 95 ºC is almost negligible) and from -35 to above 500 ºC within 15% of variation in its ε_r. The sample doped with 20% CZ presents a working temperature range from -43 to 455 ºC within 10% of variation in its ε_r and from -68 to 470 ºC within 15% of variation in its ε_r. The information regarding the materials working temperature ranges is summarized in Table 5.

Material	Sintering temperature (ºC)	Low working temperature (ºC)	High working temperature (ºC)	ε_r at 30 ºC	Variation (%)
BNT-BT-0.2CZ	1100	below -70	365	583	10
BNT-BT-0.2CZ	1100	below -70	385	583	15
BNT-BT-0.2CZ	1200	-60	443	628	10
BNT-BT-0.2CZ	1200	below -70	458	628	15
BNT-BT-KNN-0.05CZ	1100	5	377	1275	10
BNT-BT-KNN-0.05CZ	1100	-4	435	1275	15
BNT-BT-KNN-0.1CZ	1100	1	374	885	10
BNT-BT-KNN-0.1CZ	1100	-12	417	885	15
BNT-BT-KNN-0.15CZ	1100	-16	above 500	637	10
BNT-BT-KNN-0.15CZ	1100	-35	above 500	637	15
BNT-BT-KNN-0.2CZ	1100	-43	455	470	10
BNT-BT-KNN-0.2CZ	1100	-68	470	470	15

Table 5: Working temperatures and normalizing relative permittivity of the materials developed with suitable dielectric properties for high-temperature capacitors.

5.2.2 Direct current conductivity measurements

The DC conductivity measurements were done in order to observe the variation of this property in a wide temperature range. The sintering temperature and composition also affected this property (Figure 52 and Figure 53).

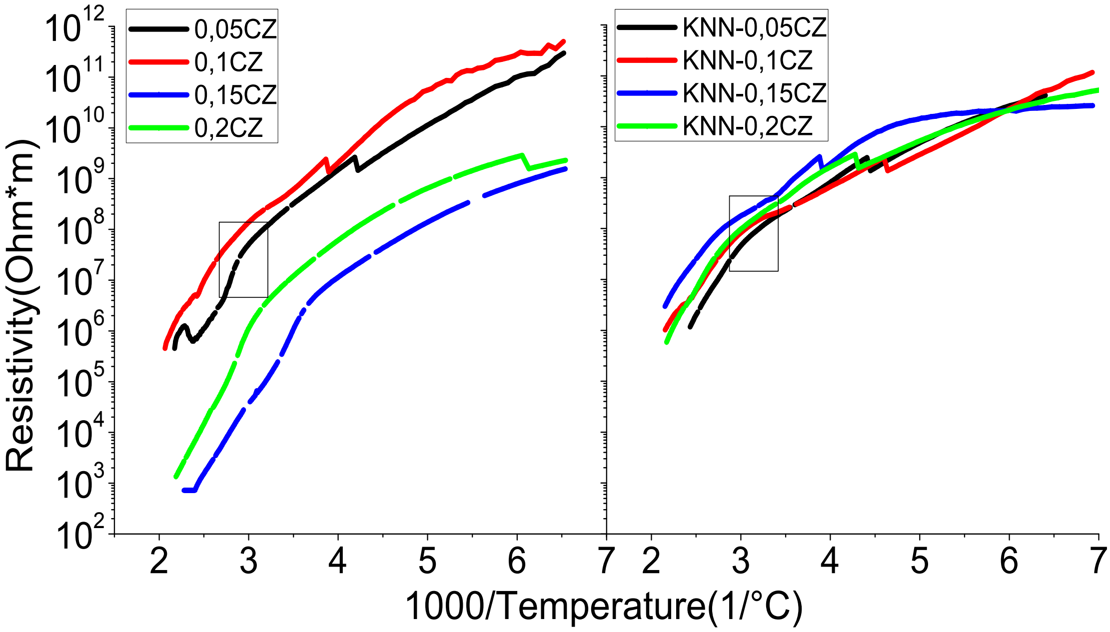

Figure 52: Resistivity vs. 1/temperature curves for the BNT-BT-CZ and BNT-BT-KNN-CZ systems. Two anomalies are observed in the curves: the diffuse one can be attributed to a change in the conductivity mechanism of the materials. The abrupt one is due to an artifact of the measuring machine. Note that a quality problem is observed for the BNT-BT-0.15CZ and BNT-BT-KNN-0.2CZ samples.

All the samples of the BNT-BT-KNN-CZ system present similar resistivity, which is increased with increasing CZ doping from 5 to 15% CZ and decreased with 20% CZ (Figure 52). This phenomenon may be attributed to the second phase observed in this last sample (Figure 24). In the BNT-BT-CZ system a different behavior is observed with increasing CZ doping. The samples with 5 and 10% CZ present the highest resistivity from all the compositions, while the ones with 15 and 20% CZ present the lowest ones. This may also be attributed to the presence of second phases (Figure 23). For this reason it was decided to increase the sintering temperatures to 1150 and 1200 ºC. Thereafter, it was observed that the resistivity at high-temperatures of these samples was increased. In other words, the quality problem was solved for the 15% CZ sample with a sintering temperature of 1150 ºC; while for the 20% CZ sample it was solved for 1200 ºC (Figure 53). Nevertheless, even at these high sintering temperatures the second phases in both compositions are still observable (Figure 25). Therefore, the second phases appearing in these samples may not be responsible for their high-conductivity. Note that all the 1100 ºC sintered samples present a change in their conductivity mechanism at high-temperatures (anomaly marked for the 5% CZ samples, Figure 52). On the other hand, this anomaly is not observed in the samples sintered above 1100 ºC.

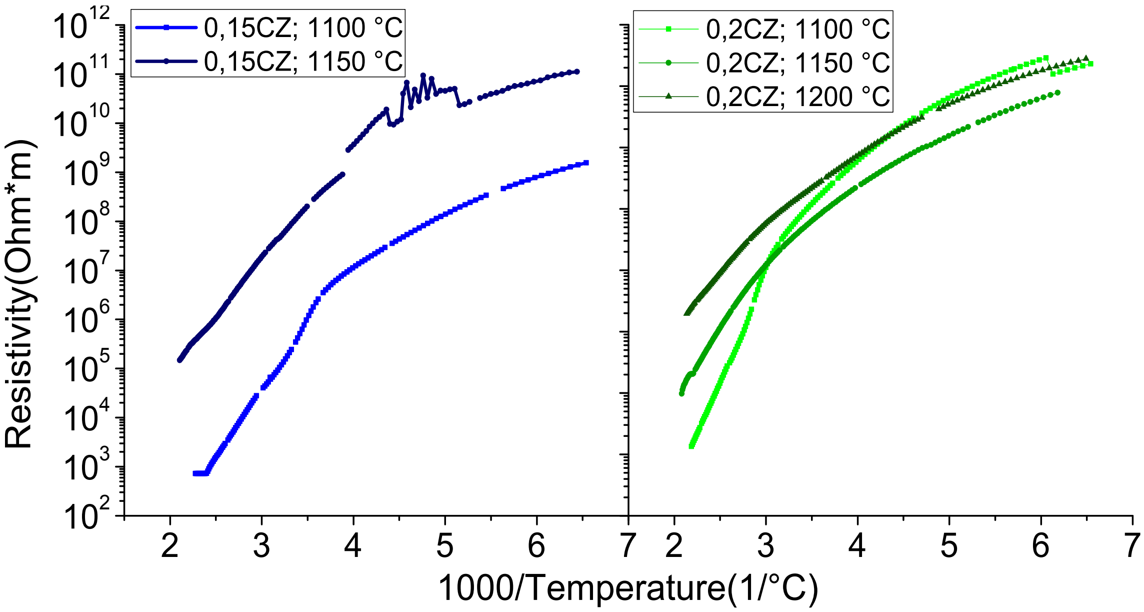

Figure 53: Effect of the sintering temperature in the resistivity vs. 1/temperature curves for the samples with 15 and 20% CZ. Note that the change in the conductivity mechanism disappears for the samples sintered above 1100 ºC. Moreover, the quality problem mentioned was solved for the 15% CZ sample by a sintering temperature of 1150 ºC; while for the 20% CZ sample it was solved by a sintering temperature of 1200 ºC.

Taking into account the resistance and capacitance of the samples, the RC constants of the developed materials was calculated at 300 ºC and 1 kHz. Note that they resulted in high values compared to others reported in literature (Figure 54).

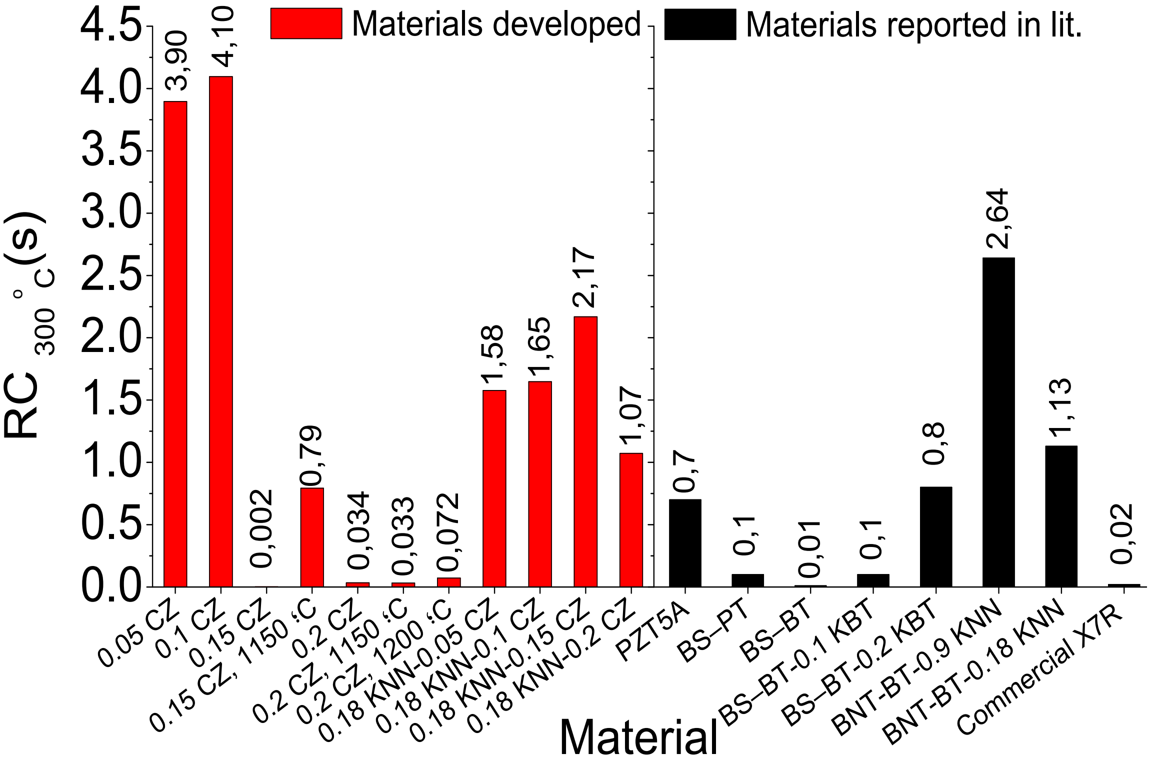

Figure 54: RC constants calculated at 300 ºC and 1 kHz for the materials developed in the present work and for other materials reported in literature [2] [57].

5.2.3 Polarization and strain measurements

These measurements were done in order to confirm the ferroelectricity of the materials developed and the influence of the CZ in this property. Moreover, the strain was measured to observe the strain occurred due to $\mathbf{E_0}$. From Figure 55 and Figure 56, it is observed that the samples with 10 and 20% CZ present an electrostrictive behavior. Moreover, the ferroelectric hysteresis loops are reduced with increasing CZ content, resulting in an almost linear behaviour for the samples with 20% CZ. Therefore, increasing the CZ doping reduces the ferroelectricity of both systems.

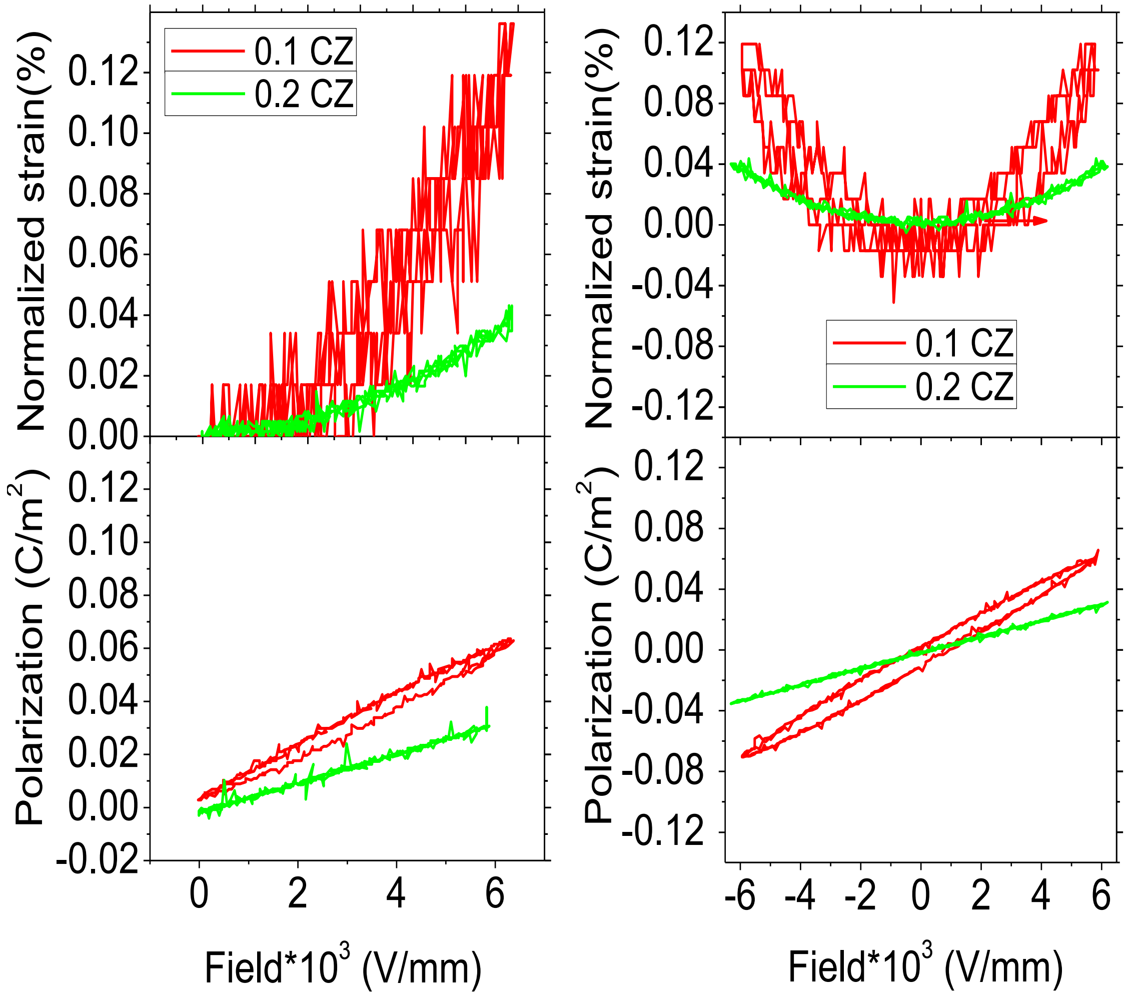

(A) **(B)**

Figure 55: (A) Unipolar and (B) Bipolar strain and polarization for the BNT-BT-0.1CZ and BNT-BT-0.2CZ samples. Note the electrostrictive behavior of both compositions and the almost linear polarization (such as in a paraelectric material) for the 20% CZ doped sample.

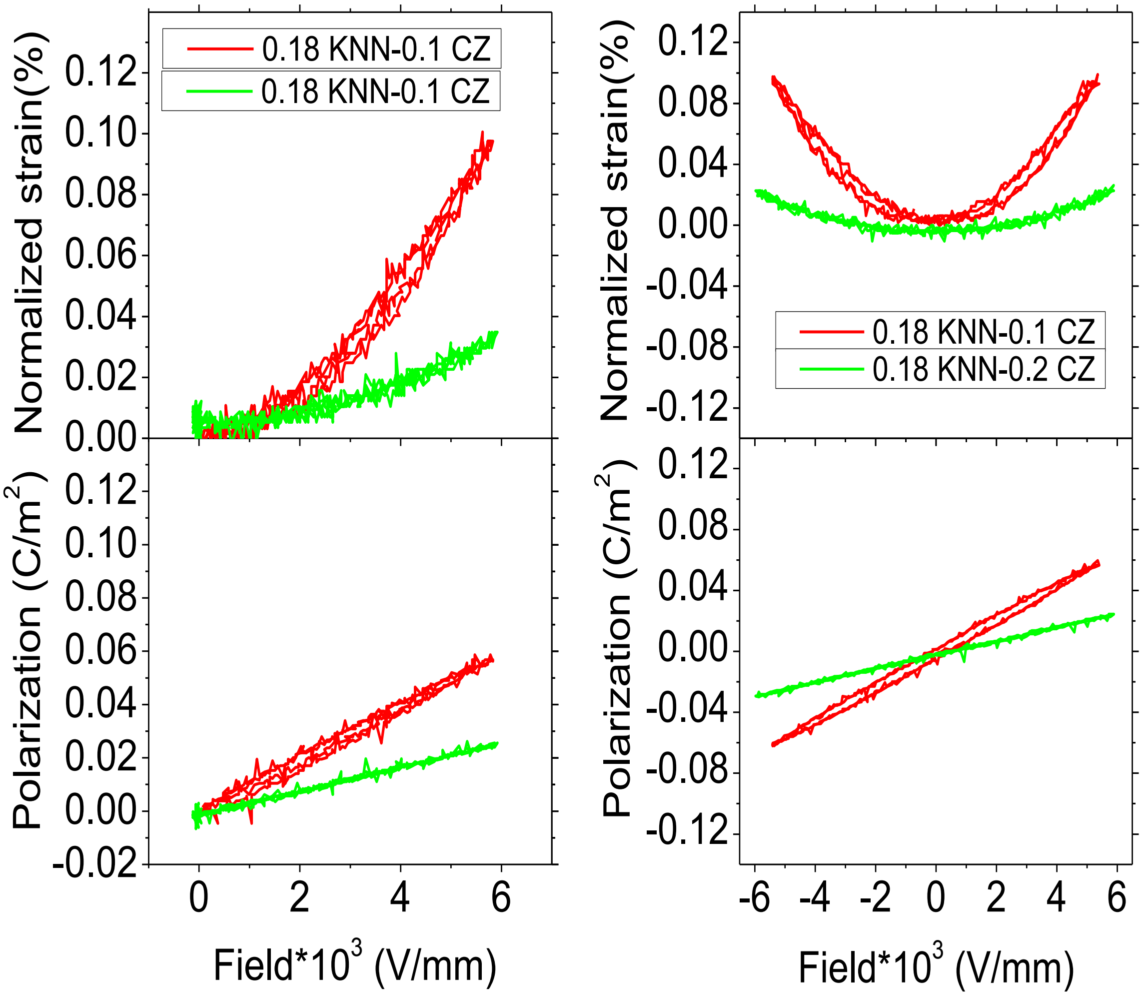

(A) **(B)**

Figure 56: (A) Unipolar and (B) Bipolar strain and polarization for the BNT-BT-KNN-0.1CZ and BNT-BT-KNN-0.2CZ samples. Note the electrostrictive behavior of both compositions and the almost linear polarization (such as in a paraelectric material) for the 20% CZ doped sample.

Note that if the temperature previously called T_f (observed in the DSC, ε_r and tan(δ) results, Section 5.1.2 and Section 5.2.1, respectively) is actually the freezing/defreezing temperature, since this temperature is quite low (about room temperature) it would be expected that the materials are in a relaxor ergodic state. The relaxor ferroelectrics at this state present a collapse of their $\mathbf{P_r}$ as consequence of the fluctuation kinetics. When the kinetics approach observable time periods (such as in the developed materials even at room temperature) the polar axes of the nanopolar regions begin to randomize and consequently a poled sample looses its macroscopic polarization and anisotropy [111]. This result was corroborated by measuring the frequency dependent ε_r and tan(δ) for the 10% CZ poled sample (not shown). These curves were the same as the ones for the unpoled sample; therefore, it can be said that the depoling of the sample was produced by the thermal fluctuations product of an ergodic state at room temperature.

5.3 Reproducibility of results

The reproducibility of the powders synthesis and samples processing was confirmed by producing (following the same powder and ceramic processing, Section 4.1) the BNT-BT-0.1CZ, BNT-BT-0.2CZ, BNT-BT-KNN-0.1CZ, BNT-BT-KNN-0.2CZ samples. The high-temperature frequency dependent ε_r and tan(δ) for these samples is presented together with the results of the samples previously produced (Figure 57 and Figure 58).

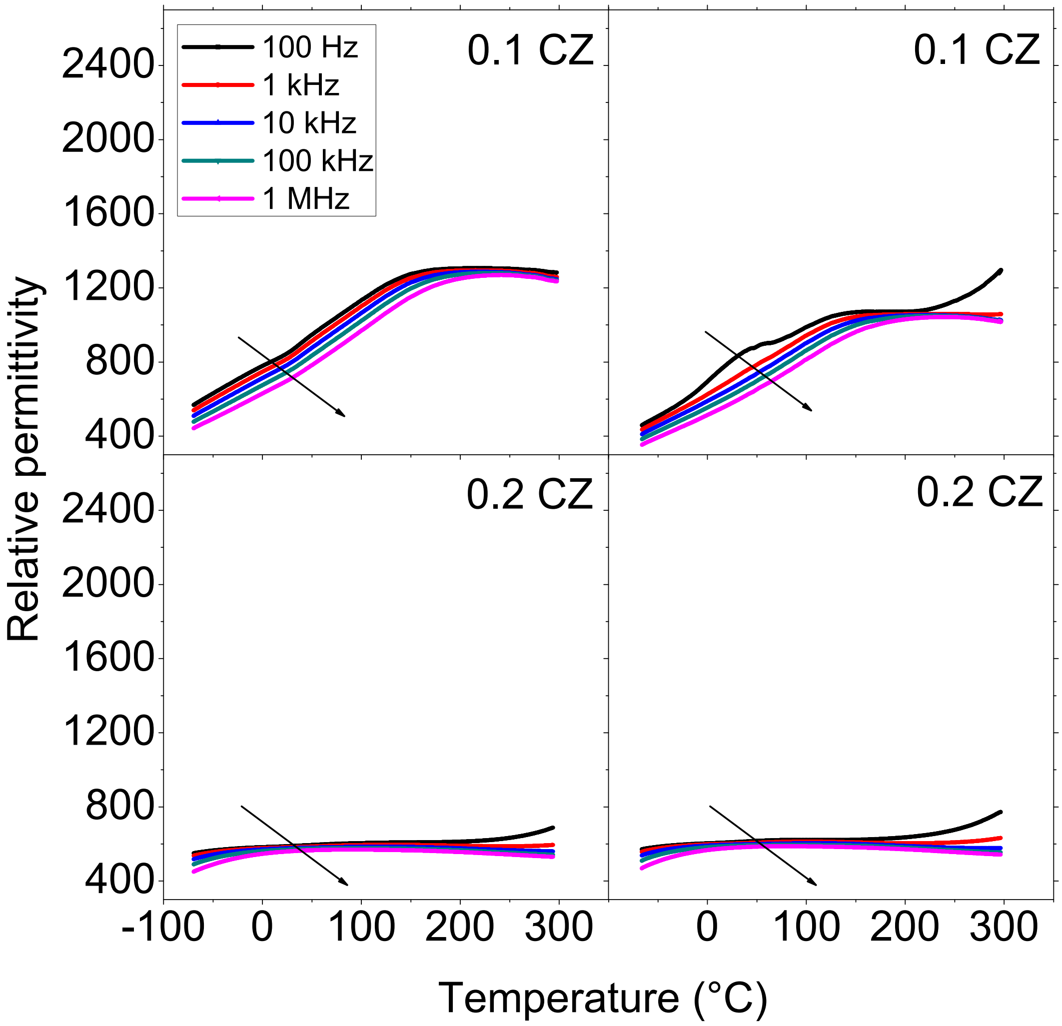

Figure 57: Relative permittivity vs. temperature for the previous synthesized samples (left) and for the new ones (right). Note that the reproducibility for the BNT-BT-CZ system is confirmed, though a low-frequency anomaly at around 45 ºC for the sample with 10% CZ can be observed.

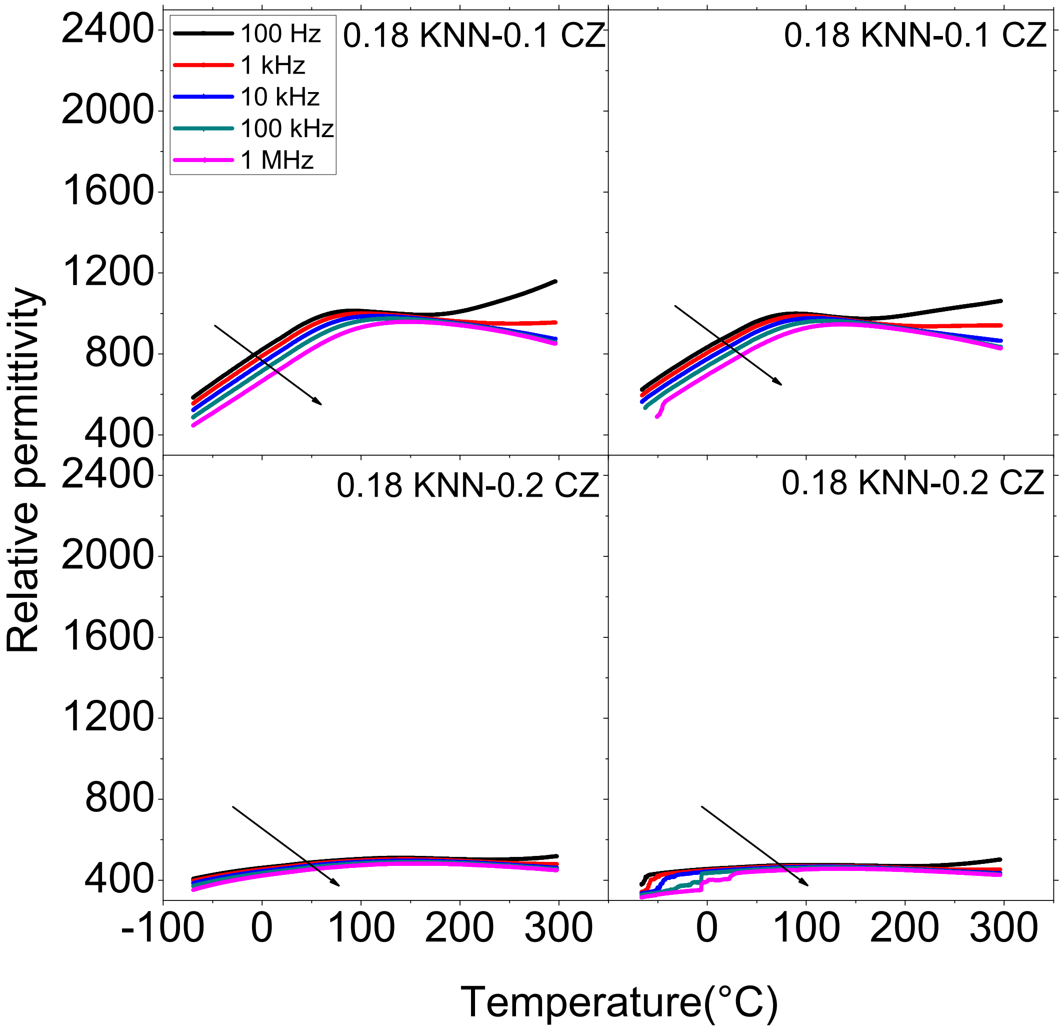

Figure 58: Relative permittivity vs. temperature for the previous synthesized samples (left) and for the new ones (right). Note that the reproducibility for the BNT-BT-KNN-CZ system is confirmed.

Note that the reproducibility of the samples dielectric properties was confirmed for both BNT-BT-CZ and BNT-BT-KNN-CZ systems (Figure 57 and Figure 58, respectively). It should be highlighted that the sample BNT-BT-0.1CZ sample presents a low-frequency anomaly at around 45 ºC. This anomaly, as the one observed for the BNT-BT-0.2CZ sample sintered at 1200 ºC (Figure 41), is frequent-independent (which can be seen in the imaginary part of the ε_r, not shown). This may be associated with nanopolar regions of big sizes and a narrow distribution size, as proposed for the 20% CZ sample previously.

6 Physical Model

Taking into account all the results presented a phase diagram for the BNT-BT-CZ system was done (Figure 59). Note that it was not possible to do one for the BNT-BT-KNN-CZ system due to the wide temperature range of the anomalies present in this system.

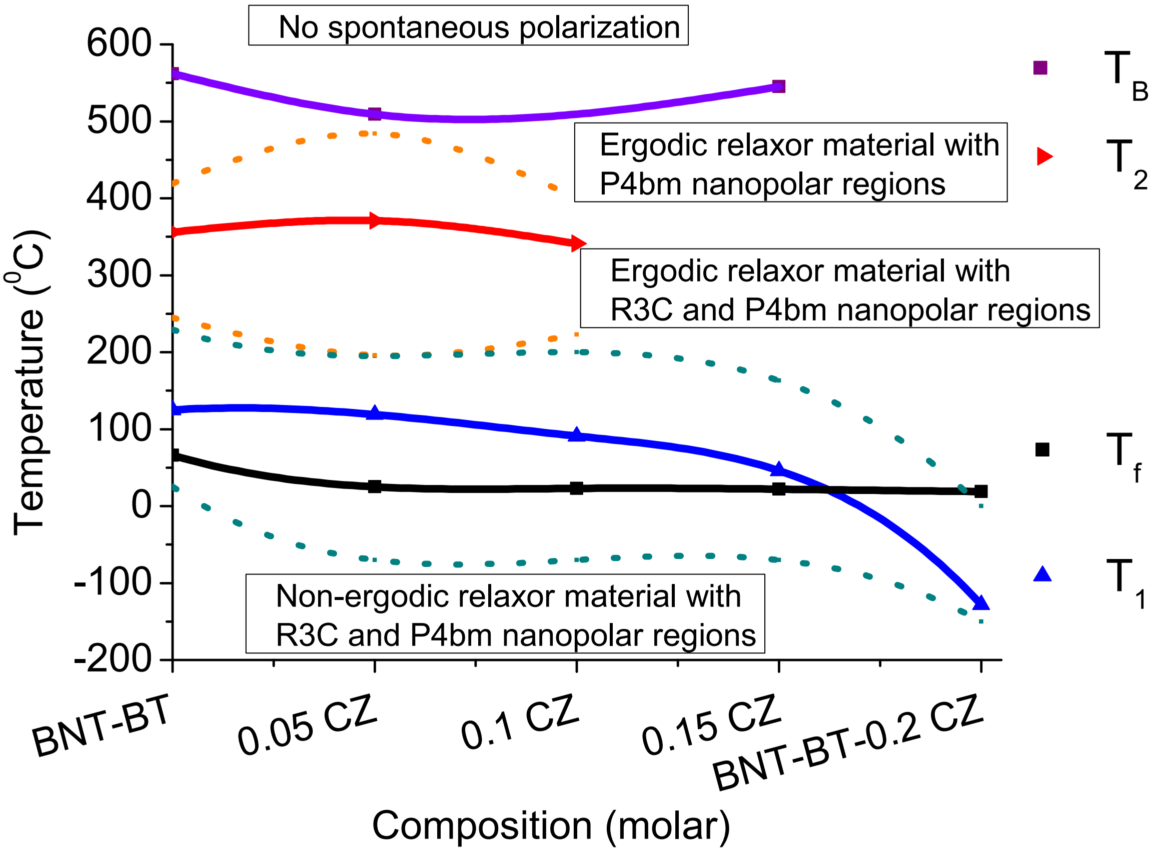

Figure 59: Phase diagram for the BNT-BT-CZ system. The solid lines correspond to the local maxima of T_B, T_2, T_1 and T_f. The dashed lines correspond to the broadness of the peaks measured in the dielectric properties.

The phase diagram was done taking into account the electrical and DSC measurements. The solid lines correspond to the local maxima of T_B,T_2,T_1 and T_f. The dashed lines correspond to the broadness of the peaks measured in the dielectric properties results.

7 Conclusions

New non contaminant high-temperature dielectrics were developed in the (1–x)($0.94Bi_{0.5}Na_{0.5}TiO_3$–$0.06BaTiO_3$)–x$CaZrO_3$ and (1–x)(0.82($0.94Bi_{0.5}Na_{0.5}TiO_3$–$0.06BaTiO_3$)–$0.18K_{0.5}Na_{0.5}NbO_3$)–x$CaZrO_3$ systems, with x=0, 0.05, 0.1 and 0.2. These materials were synthesized via a mixed oxide route and sintering temperatures of 1100, 1150 and 1200 ºC. The materials were characterized regarding their microstructural and electrical properties. The microstructural analysis was done measuring the X-ray diffraction patterns, the DSC curves and density; as well as obtaining HREM micrographs. The electrical characterization was done measuring the temperature and frequency dependent ε_r and tan(δ), DC conductivity, polarization and strain.

From the XRD measurement, it was observed that all the peaks corresponded to a cubic perovskite-type unit-cell. Nevertheless, it should be mentioned that in the BNT-BT-0.15CZ, BNT-BT-0.2CZ and BNT-BT-KNN-0.2CZ samples a second phase was observed. Therefore, it can be said that the solubility limit of the BNT-BT based materials is around 15% CZ. Both systems presented an almost linear increment of the lattice parameter with increasing CZ, which is in agreement with the expected increment considering the ionic radius of the elements introduced in both systems. Moreover, a reduction in the lattice parameter with increasing sintering temperature was observed.

There was no clear change in the samples density with increasing CZ doping. All the samples presented relative densities above 96%, with the exception of the BNT-BT-0.1CZ sample which presented a relative density of 84%.

For the BNT-BT-CZ system, no clear tendency in the samples porosity or grain size with increasing CZ doping was observed in the HREM results. Nevertheless, it should be highlighted that the 10% CZ sample presented a higher porosity than that observed in other samples. This result was in agreement with the low density measured for this composition. On the other hand, in the BNT-BT-KNN-CZ system, it was observed that the porosity was reduced, while the grain size was increased with increasing CZ doping. Furthermore, for both systems a bimodal distribution of grain sizes was observed.

Three anomalies were observed in the temperature and frequency dependent ε_r and tan(δ) for the BNT-BT-CZ system. They presented a frequency dispersion, but with different tendencies. Moreover, around them after a heating-cooling cycle, frequency dependent thermal hysteresis loops could be seen in both the ε_r and tan(δ). These anomalies were explained considering that the material is a relaxor ferroelectric. The anomaly at low-temperature was attributed to the freezing/defreezing temperature (T_f) from an ergodic to a non-ergodic state. The second anomaly at T_1 was attributed to the thermal evolution of rhombohedral *R3C* (and presumably also to the thermal evolution of the coexisting tetragonal *P4bm* nanopolar regions). The high-temperature anomaly at T_2 was attributed to a convolution of the thermal evolution of the *P4bm* nanopolar regions and the change in symmetry of the *R3C* to the *P4bm* nanopolar regions. It should also be mentioned that in some samples the anomaly at T_f was not observed, presumably due to a convolution between it and the one appearing at T_1, since the temperatures of both anomalies were in a short temperature range. It was also observed that the dielectricity and ferroelectricity of the system was decreased significantly with increasing CZ doping, this would indicate that it stabilizes the non-polar cubic matrix (or almost non-polar), thus resulting in nanopolar regions of smaller sizes. This was corroborated taking into account that the anomalies observed at T_1 were shifted to lower temperatures, the ε_r was decreased significantly and the ferroelectric hysteresis loops were slimmer with increasing CZ doping. Moreover, the ergodic relaxor state was corroborated by measuring the ε_r and tan(δ) curves of the 10% CZ poled sample, which resulted in the same shape as the unpoled one. The temperature and frequency dependent ε_r and tan(δ) for the BNT-BT-KNN-CZ system was also measured. The described anomalies were also observed for this system. Nevertheless, the one at T_2 presented a more diffuse shape. Moreover, all the anomalies were observed at lower temperatures than that in the BNT-BT-CZ system. Nevertheless, a flattened ε_r and tan(δ) similar to that observed for the BNT-BT-CZ resulted with increasing CZ content.

The BNT-BT-0.2CZ, BNT-BT-KNN-0.05CZ, BNT-BT-KNN-0.1CZ, BNT-BT-KNN-0.15CZ, BNT-BT-KNN-0.2CZ samples presented suitable properties for high-temperature dielectric materials since they presented at least a working temperature range of 370 ºC within 15% of variation in their ε_r. The working temperature-ranges reported are significantly wide if they are compared to that observed in literature or international standards (Section 3.1.2). Moreover, all the presented materials have RC constants far above from that reported in a commercial X7R material. Taking into account that the raw materials used were non-contaminant and inexpensive, the simple processing and the dielectric properties of the developed materials, it can be said that these systems are highly attractive for high-temperature industrial applications such as high-temperature capacitors or short-period high-temperature energy storage devices. Last but not least, it should also be highlighted that the materials and dielectric properties reproducibility were corroborated.

8 References

[1] A. N. Hammoud and I. T.Myers, ‘‘Evaluation of High-temperature Capacitor Dielectrics, Electrical Insulation and Dielectric Phenomena,’’ Annu. Rep., Vol. 29 (1989), 459.

[2] R. Dittmer, W. Jo, D. Damjanovic, J. Rödel, “Lead-free high-temperature dielectrics with wide operational range“, J. App. Phys., Vol. 109 (2011).

[3] C. A. Randall, H. Ogihara, J.-R. Kim, G.-Y. Yang, C. S. Stringer, S. Trolier-McKinstry, and M. Lanagan, Proceedings of the IEEE Pulsed Power Conference 2009, Washington, DC, 28 June-2 July 2009, 346.

[4] H.C. Ling, M.F Yan, W.W. Rhodes, “High dielectric constant and small temperature coefficient bismuth-based dielectric compositions”, J. Mater. Res., Vol. 5 (1990), 1752.

[5] Global Industry Analysts, Inc., “Discrete Capacitors: A global strategic Business Report“, Press Release (2009), Code: MCP-1841.

[6] E. Sugimoto, ‘‘Applications of Polyimide Films to the Electrical and Electronic Industries in Japan,’’ IEEE Electr. Insul. Mag., Vol. 5 (1989), 15.

[7] R. W. Johnson, J. L. Evans, P. Jacobsen, J.R. Thompson, M. Christopher, “The changing Automotive Enviroment: High-Temperature Electronics“, IEEE Trans. Electr. Pack. Manuf., Vol. 27 (2004), 164.

[8] J. Goetz, “High-temperature Electronics for Sensor Interface and Data Acquisition“, Sensors Exposition, October 1998.

[9] D. E. Aspnes, “Local field effects and effective-medium theory: A microscopic perspective”, Am. J. Phys.(1982), Vol. 50, 8.

[10] F. Cardarelli, “Materials Handbook: A Concise Desktop Reference”, 2nd Edition, Springer (2008), Chapter 8: “Insulators and Dielectrics”.

[11] C. Kittel, “Introduction to Solid State Physics”, 7th Edition, John Wiley and Sons (1996), Chapter 13: “Dielectrics and Ferroelectrics”.

[12] A.J. Moulson, J.M. Herbert, “Electroceramics: Materials, Properties, Applications”, Second Edition, Wiley (2003), Chapter 2: “Elementary solid State Science”.

[13] G. H. Haertling, “Ferroelectric Ceramics: History and Technology”, J. Am. Ceram. Soc. (1999), Vol. 82, 797.

[14] B. Jaffe, “Piezoelectric Ceramics”, Academic Press Public (1971), Chapter 2: “The piezoelectric effect in Ceramics”.

[15] K. Momma, F. Izumi, "VESTA: a three-dimensional visualization system for electronic and structural analysis," J. Appl. Crystallogr., Vol. 41 (2008), 653.

[16] K. Rabe, Ch. H. Ahn, J.M. Triscone, "Physics of ferroelectrics: A Modern Perspective", Top. in App. Phys., Vol. 105 (2007).

[17] J. Jo, J. E. Daniels, J.L. Jones, X. Tan, P.A. Thomas, D. Damjanovic, J. Rödel, “Evolving morphotropic phase boundary in lead-free $(Bi_{1/2}Na_{1/2})TiO_3$-$BaTiO_3$ piezoceramics”, Journal of Ap. Phys., Vol. 109 (2011), 014110.

[18] K. Hirota, S. Wakimoto , D. E. Cox, “Neutron and X-ray Scattering Studies of Relaxors”, *J. Phys. Soc. Jpn.*, Vol. 75 (2006), 111006.

[19] L. E. Cross, “Relaxor Ferroelectrics”, Ferroelectrics, Vol. 76 (1987), 241.

[20] E. Blinc, “Order and Disorder in Perovskites and Relaxor Ferroelectrics”, Sreuct. Bond, Vol. 124 (2007), 51.

[21] Z.G. Ye, “Relaxor Ferroelectric Complex Perovskites: Structure, Properties and Phase Transitions”, Key Engineering Mat., Vols. 155-156 (1998), 81.

[22] ‘‘EU-Directive 2002/96/EC: Waste Electrical and Electronic Equipment (WEEE),’’ Off. J. Eur. Union, Vol. 46 (2003), 24.

[23] ‘‘EU-Directive 2002/95/EC: Restriction of the Use of Certain Hazardous Substances in Electrical and Electronic Equipment (RoHS),’’ Off. J. Eur. Union, Vol. 46 (2003), 19.

[24] Verordnung zur Reduktion von Risiken beim Umgang mit bestimmten besonders gefährlichen Stoffen, Zubereitungen und Gegenständen (Chemikalien-Risikoreduktions-

Verordnung, ChemRRV).'' Amtliche Sammlung des Bundesrechts (Swiss Federal Legislation, 2005) [AS 2005 2917].

[25] ''Regulations Relating to Restrictions on the Manufacture, Import, Export, Sale and Use of Chemicals and Other Products Hazardous to Health and the Environment'', Product Regulations Norway (2004).

[26] ''Restriction of the Use of Certain Hazardous Substances in Electrical and Electronic Equipment.'' Ministry of Environment and Forestry Turkey Regulation (2008), No. 26891.

[27] ''Act for Resource Recycling of Electrical and Electronic Equipment and Vehicles.'' Environment and Labor Committee of the National Assembly of Korea Bill No. 6319 (2007).

[28] ''Law for Promotion of Effective Utilization of Resources'', Minister of Economy, Trade and Industry (2001), Japan.

[29] ''Measures for the Administration on Pollution Control of Electronic Information Products.'' Ministry of Information Industry China Order No. 39 (2006).

[30] ''Preliminary Environmental and Economic Assessment of Australian RoHS Policy", Hyder Consulting Pty Ltd for the Department of Environment and Water Resources (2007).

[31] T. Lindhqvist, P. Manomaivibool, N. Tojo, "La responsabilidad extendida del productor en el contexto latinoamericano: La gestión de recursos de aparatos eléctricos y electrónicos en Argentina", IIIEE Reports Lund University (2008).

[32] J. Rödel, W. Jo, K. T.P. Seifert, E.M. Anton, T. T. Granzow, "Perspective on the Development of Lead-free Piezoceramics", J. Am. Ceram. Soc., Vol. 92 (2009), 1153.

[33] Electronic Industries Alliance (EIA): EIA-198-1-F, Ceramic Dielectric Capacitors Classes I, II, III and IV - Part I: Characteristics and Requirements. United States: EIA, 2002.

[34] K. D. Jamison, R. D. Wood, B. G. Zollars, M. E. Kordesch, "Use of Amorphous Oxides as High-temperature Dielectric Material in Wound Capacitors", Conference Paper Nanohmics Austin TX (2008).

[35] N. Venkat, T. D. Dang, Z. Bai, V. K. cNier, J. N. Decerbo, B.H. Tsao, J. T. Stricker, "High-temperature polymer film dielectrics for aerospace power conditioning capacitor applications", Mat. Sci. and Eng., Vol. 168 Sec. B (2010), 16.

[36] J. Stricker, J. Scofield, N. Brar, J. DeCerbo, "Evaluation of flurene polyester film capacitors", United Stated Air Force Public release (2010).

[37] K. Saarinen, E. Matero, J. Perälä, "SMD Plastic Film Capacitors for High-temperature Applications", Carts: 24th Annual Capacitor and Resistor Technology Symposium (2004).

[38] M. Akram, A. Javed, T. Z. Rizvi, "Dielectric Properties of Industrial Polymer Composite Materials", Turk. J. Phys., Vol. 29 (2005), 355.

[39] Z.M. Dang, H. T. Song, Y. Q. Lin, L.J. Ma, "High and low dielectric permittivity polymer-based nanohybrid dielectric films", J. of Phys. Conf. Series, Vol. 152 (2009).

[40] J. Dun, B. Jones, M. Lanagan, "Preparation and characterization of dielectric glass-ceramics in Na_2O-PbO-Nb_2O_5-SiO_2", Mat. Lett., Vol. 59 (2005), 2821.

[41] C. Mao, X. Sun, J. Du, Q. Tang, "Preparation and dielectric properties of Nb_2O_5-BaO-Na_2O-SiO_2 glass-ceramic for energy storage capacitors", J. of Phys. Conf. Series, Vol. 152 (2009).

[42] K. D. Jamison, M. E. Kordesch, U.S. Patent No. US7.460.352 B2 (2008).

[43] K. R. Bray, R.L.C. Wu, S. F. Carr, J. Weimer, "Aluminum oxynitride dielectrics for multilayer capacitors with higher energy density and wide temperature properties", Thin Sol. Films, Vol. 518 (2009), 366.

[44] F.E. Kamel, P. Gonon, F. Jomni, "Electrical properties of low-temperature deposited amorphous barium titanate thin films as dielectrics for integrated capacitors", Thin Sol. Films, Vol. 504 (2006), 201.

[45] J. M. Wilson, U.S. Patent No.: 5,128,289 (1992).

[46] X. Wang, R. Chen, Z. Gui, L. Li, U.S. Patent No.: US 2004/0138050 A1 (2004) .

[47] K . Kamigaki, D. Fukuda, U.S. patent No.: US 2009/0207556 A1 (2009).

[48] X. Wang, R. Chen, Z. Gui, L. Li, U.S. patent No.: US 7,022,635 B2 (2006).

[49] Y. Yuan, X. H. Zhou, B. Li, S. R. Zhang, "Effects of $BiNbO_4$ and Nb_2O_5 additions on the temperature stability of modified $BaTiO_3$", Ceramics-Silikáty, Vol. 54 (2010) 258.

[50] Y. Yuan, S.R. Zhang, X.H. Zhou, B. Tang, B. Li, “High-Temperature Capacitor Materials Based on Modified $BaTiO_3$”, J. of Electroceramic Mat., Vol. 38 (2009), 706.

[51] S. Zhang, S. Wang, X: Zhou, B. Li, Z. Chen, “Influence of ·d-elements on dielectric properties of $BaTiO_3$”, J. of Mat. Science: Mat. in Electr., Vol. 16 (2005), 669.

[52] S. Wang, S. Zhang, X. Zhou, B. Li, Z. Chen, “Investigation on dielectric properties of $BaTiO_3$ co-doped with Ni and Nb”, Mat. Lett., Vol. 60 (2006), 909.

[53] D. Hennings, G. Rosenstein, “Temeprature-Stable Dielectrics Based on Chemically Inhomogoneous $BaTiO_3$”, J. of Am. Ceram. Soc., Vol. 67 (1984), 249.

[54] H. Wen, X. Wang, Z. Gui, L. Li, “Modeling of the core-shell microstructure of temperature-stable $BaTiO_3$ based dielectrics for multilayer ceramic capacitors”, J. Electroceram., Vol. 21 (2008), 545.

[55] H. Naghib-zadeh, C. Glitzky, W. Oesterle, T. Rabe, “Low-temperature sintering of barium titanate based ceramics with high dielectric constant for LTCC applications”, J. of the Europ. Ceram. Soc., Vol. 31 (2011), 589.

[56] S. H. Yoon, J. H. Lee, D. Y. Kim, N. M. Hwang, “Core-Shell Structure of Acceptor Rich, Coarse Barium Titanate Grains”, J. Am. Ceram. Soc., Vol. 85 (2002), 3111.

[57] J. B. Lim, S. Zhang, N. Kim, T.R. Shrout, “High-Temperature Dielectrics in the $BiScO_3$-$BaTiO_3$-$(K_{1/2}Bi_{1/2})TiO_3$ Ternary System”, J. Am. Ceram. Soc., Vol. 92 (2009), 679.

[58] S. Zhang, E. F. Alberta, R. E. Eitel, C. A. Randall, and T. R. Shrout, “Elastic, Piezoelectric, and Dielectric Characterization of Modified $BiScO_3$-$PbTiO_3$ Ceramics”, IEEE Trans. Ultrason. Ferroelectr. Freq. Control, Vol. 52 (2005), 2131.

[59] H. L. Du, W. C. Zhou, F. Luo, D. M. Zhu, S. B. Qu, Y. Li, and Z. B. Pei, “Phase structure, dielectric properties, and relaxor behavior of $(K_{0.5}Na_{0.5})NbO_3$–$(Ba_{0.5}Sr_{0.5})TiO_3$ lead-free solid solution for high-temperature applications”, J. Appl. Phys., Vol. 104 (2008).

[60] K. Tsuzuku, M. Fujimoto, “Temperature-Stable Lead-Relaxor-Based Ceramic Dielectrics with Chemical Inohomogeneity”, J. Am. Ceram., Vol. 77 (1994),1451.

[61] L. Ruan, L. Li, Z. Gui, “Temperature stable dielectric properties for $Pb(Mg_{1/3}Nb_{2/3})O_3$-$BaTiO_3$-$PbTiO_3$ system ceramics”, J. of Mat. Sci., Vol. 16 (1997), 1020.

[62] Y. Yuan, X.H. Zhou, C.J. Zhao, B. Li, S.R. Zhang, “High-Temperature Capacitor Based on Ca-Doped $Bi_{0.5}Na_{0.5}TiO_3$-$BaTiO_3$ Ceramics”, J. Electr. Mat., Vol. 39 (2010), 2471.

[63] J.S. Park, S.C. Lee, M.H. Lee, D.J. Kim, Y.S. Sung, M. H. Kim, T.K. Song, “Effects of Zr doping on the Depolarization Temperature and the Piezoelectric Properties in $(Bi_{0.5}Na_{0.5})TiO_3$-$BaTiO_3$ Lead-free Ceramics”, J. of Kor. Phys. Soc., Vol. 57 (2010), 1905.

[64] K. Bridger, A.V. Cook, W.A. Schulze, U.S. Patent No. US7.697.263 B2 (2010).

[65] Y. Wang, J. Wu, D. Xiao, B. Zhang, W. Wu, W. Shi, J. Zhu, “Electrical properties and temperature stability of a new kind of lead-free piezoelectric ceramics”, J. Phys. D: App. Phys., Vol. 41 (2008).

[66] B. Tang, S. Zhang, X. Zhou, L. Xiang, “Microstructure and dielectric properties of $BaTiO_3$-Nb_2O_5-$Zn_{0.8}Mg_{0.2}TiO_3$ ternary system”, Ceramics- Silikaty, Vol. 52 (2008), 45.

[67] K. Bridger, A. V. Cooke, W. A. Schulze, U.S. Patent No.: 11/691,837 (2007).

[68] K. Bridger, A. V. Cooke, W. A. Schulze, U.S. Patent No.: US 2008/0239627 A1 (2008).

[69] G.A. Smolenskii, V.A. Isupov, A.I. Agranovskaya, and N.N.Krainik, "New Ferroelectrics of Comlex Composition ", Sov. Phys. Solid State, Vol. 2 (1961), 2651.

[70] T. Takenaka, K. Maruyama, and K. Sakata, "$(Bi_{1/2}Na_{1/2})TiO_3$-$BaTiO_3$ System for Lead-Free Piezoelectric Ceramics", Jpn. J. Appl. Phys., Vol. 30 (1991), 2236.

[71] T. Takenaka and K. Sakata," Dielectric, Piezoelectric and Pyroelectric Properties of $(Bi/Na)_{1/2}TiO_3$-Based Ceramics ", Ferroelectrics, Vol. 95 (1989), 153.

[72] H. Nagata and T. Takenaka, "Lead-Free Piezoelectric Ceramics of $(Bi_{1/2}Na_{1/2})TiO_3$–$1/2(Bi_2O_3{\cdot}Sc_2O_3)$ System", Jpn. J. Appl. Phys., Vol. 36 (1997), 6055.

[73] Wang Y P, Yuan G L, Chen X Y, Liu J-M and Liu Z G, "Electrical and magnetic properties of single-phased and highly resistive ferroelectromagnet $BiFeO_3$ ceramic ", J. Phys. D: Appl. Phys., Vol. 39 (2006), 2019.

[74] Eitel R E, Randall C A, Shrout T R, Rehrig P W and Park S, "Preparation and Characterization of High-temperature Perovskite Ferroelectrics in the Solid-Solution (1-x)$BiScO_3$-x$PbTiO_3$", Japan. J. Appl. Phys., Vol. 40 (2001). 5999.

[75] X. Wang, A. Yang, "Dielectric and ferroelectric properties of $(Bi_xBa_{1-x})(Zn_{x/2}Ti_{1-x/2})O_3$ ceramics", J. Appl. Phys., Vol. 42 (2009).

[76] Y. M. Li, W. Chien, Q. Xu, J. Zhou, H.J. Sun, M.S. Liao, "Dielectric and Piezoelectric Properties of $Na_{0.5}Bi_{0.5}TiO_3$-$K_{0.5}Bi_{0.5}TiO_3$-$NaNbO_3$", J. of Electroceram., Vol. 14 (2005), 53.

[77] G.O. Jones, P.A. Thomas, "Investigation of the structure and phase transitions in the novel A-site substituted distorted perovskite compound $Na_{0.5}Bi_{0.5}TiO_3$", Acta Crys., Vol. 58 Sec. B (2001), 168.

[78] A. M. Glazer, "The Classification of Tilted Octahedra in Perovskites", Acta Cryst., Vol. 28 Sec. B (1972), 3384.

[79] G. O. Jones, P. A. Thomas, "The tetragonal phase of $Na_{0.5}Bi_{0.5}TiO_3$ a new variant of the perovskite structure", Acta Cryst., Vol. 56 Sec. B (2000), 426.

[80] J. Suchanicz, M. G. Gavshini, A. Y. Kudzin, C. Kus, "Dielectric properties of $(Na_{0.5}Bi_{0.5})_{1-x}Me_xTiO_3$ ceramics near morphotropic phase boundary", J. Mat. Sci., Vol. 36 (2001), 1981.

[81] K. Sakata, Y. Masuda, "Ferroelectric and Antiferroelectric Properties of $Na_{0.5}Bi_{0.5}TiO_3$-$SrTiO_3$ Solid Solution Ceramics", Ferroelec. , Vol. 7 (1974), 347.

[82] X.X. Wang, H.L. Chan, C.L. Choy, "Piezoelectric and dielectric properties of CeO_2-added $(Bi_{0.5}Na_{0.5})_{0.94}Ba_{0.06}TiO_3$ lead-free ceramics", Solid State Comm., Vol. 125 (2003), 395.

[83] J.Kreisel, A. M. Glazer, G. O. Jones,P. A. Thomas,L. Abello, G. Lucazeau, "An X-ray diffraction and Raman spectoscropy investigation of A-site substituted perovskite compounds: the $(Na_{1-x}K_x)_{0.5}Bi_{0.5}TiO_3$ $(0<x<1)$ solid solution", J. Phys. Condens. Matter, Vol. 12 (2000), 3267.

[84] R. Zuo, H. Wang, B. Ma, L. Li, "Effects of Nb^{5+} doing on sintering and electrical properties of lead-free $(Bi_{0.5}Na_{0.5})TiO_3$ ceramics", J. Mat. Sci.:Mater. Electron., Vol. 20 (2009), 1140.

[85] Y. Yuan, C.J. Zhao, X.H. Xhou, B. Tang, S.R. Zhang, "High-temperature stable dielectrics in Mn-modified (1.x)$Bi_{0.5}Na_{0.5}TiO_3$-$CaTiO_3$ ceramics", J. Electrocer., Vol. 25 (2010), 212.

[86] Y. Hiruma, Y. Watanabe, H. Nagata, T. Takenaka, "Phase Transition Temperatures of Divalent ad Trivalent Ions Substituted $(Bi_{1/2}Na_{1/2})TiO_3$ Ceramics", Key Engine. Mat., Vol. 350 (2007), 93.

[87] B. Jaffe, W. R. Cook Jr, and H. Jaffe, "Piezoelectric Ceramics", Academic Press London (1971), 317.

[88] D. Hennings, A. Schnell, and G. Simon, ''Diffuse Ferroelectric Phase Transitions in $Ba(Ti_{1-y}Zr_y)O_3$ Ceramics,' J. Am. Ceram. Soc., Vol. 65 (1982), 539.

[89] Y. Okino, N. Kohzu, Y. Mizuno, M. Honda, H. Chazono, and H. Kishi, ''Effects of the Microstructure on Dielectric Properties for $BaTiO_3$-Based MLC with Ni Electrode,'' Key Eng. Mater., Vol. 157 (1999), 9.

[90] K. G. Webber, Y. Zhang, W. Jo, J,E. Daniels, J. Rödel, "High-temperature stress-induced "double loop-like"phase transitions in Bi-based perovskites", J. App. Phys., Vol. 108 (2010), 014101.

[91] S.T. Zhang, A. B. Kounga, E. Aulbach, Y. Deng,"Temperature-Dependent Electrical Properties of $0.94Bi_{0.5}Na_{0.5}TiO_3$–$0.06BaTiO_3$ Ceramics", J. Am. Ceram. Soc., Vol. 91 (2008), 3950.

[92] B. J. Chu, D.R. Chen, G. R. Li, Q.R. Yin, "Electrical properties of $Na_{1/2}Bi_{1/2}TiO_3$-$BaTiO_3$", J. of the Europ. Ceram. Soc., Vol. 22 (2002), 2115.

[93] C. Ma, X. Tan, E. Dul´kin, M. Roth, "Domain structure-dielectric property relationship in lead-free (1-x)$(Bi_{1/2}Na_{1/2})TiO_3$-x$BaTiO_3$ ceramics", J. App. Phys., Vol.108 (2010).

[94] F. Cordero, F. Cracium, F. Trequattrini, E. Mercadelli, C. Galassi, "Phase transitions and phase diagram of the ferroelectric perovskite $(Na_{0.5}Bi_{0.5})_{1-x}Ba_xTiO_3$ by anelastic and dielectric measurements", Phys. Rev. B, Vol. 81 (2010).

[95] J. Yao, L. Yan, W. Ge, L. Luo, J. Li, D. Viehland, "Evolution of domain structures in $Na_{1/2}Bi_{1/2}TiO_3$ single crystals with $BaTiO_3$", Phys. Rev. B, Vol. 83 (2011).

[96] J. Yao, L. Yan, W. Ge, L. Luo, J. Li, D. Viehland, "Evolution of domain structures in $Na_{1/2}Bi_{1/2}TiO_3$ single crystals with $BaTiO_3$", Phys. Rev., Vol. 83 Sec. B (2011).

[97] J. B. Babu, G. Madeswaran, X. L. Chen, R. Dhanasekaran, "Effect of oxygen vacancies on ferroelectric behavior of $Na_{1/2}Bi_{1/2}TiO_3$-$BaTiO_3$ single crystals", Mat. Sci. and Eng., Vol. 156 Sec. B (2009), 26.

[98] X. Chen, W. Pan, H. Tian, X. Gong, X. Bian, P. Liu, "Microstructure, dielectric and ferroelectric properties of $0.94Bi_{0.5}Na_{0.5}TiO_3$-$0.06BaTiO_3$ (NBTB) and $0.05BiFeO_3$-0.95NBTB ceramics: Effect of sintering atmosphere", J. of Alloys and Comp., Vol. 509 (2011), 1824.

[99] X.M. Chen, X.X. Gong, T.N. Li, Y. He, P. Liu, "Microstructure, dielectric and ferroelectric properties of $(1-x)(0.94Bi_{0.5}Na_{0.5}TiO_3$–$0.06BaTiO_3)$–$xBiFeO_3$ lead-free ceramics synthesized via a high energy ball milling method ", J. Alloys Compd., Vol. 507 (2010), 535.

[100] C. Peng, J.F. Li, W. Gong, "Preparation and properties of $(Bi_{1/2}Na_{1/2})TiO_3$-$Ba(Ti,Zr)O_3$ lead-free piezoelectric ceramics", Mat. Lett., Vol. 59 (2005), 1576.

[101] R. Zuo, C. Ye, X. Fang, J. Li, "Tantalum doped $0.94Bi_{0.5}Na_{0.5}TiO_3$-$0.06BaTiO_3$ piezoelectric ceramics", J. of the Europ. Soc., Vol. 28 (2008), 871.

[102] S. T. Zhang, A. B. Kounga, W. Jo, C. Jamin, K. Seifert, T. Granzow, J. Rödel, D. Damjanovic, "High-Strain Lead-free Antiferroelectric Electrostrictors", Adv. Mat., Vol. 21 (2009), 1.

[103] S.T. Zhang, F. Yan, B. Yang, W. Cao, "Phase diagram and electrostrictive properties of $Bi_{0.5}Na_{0.5}TiO_3$-$BaTiO_3$-$K_{0.5}Na_{0.5}NbO_3$ ceramics", App. Phys. Lett., Vol. 97 (2010).

[104] M. Hinterstein, M. Knapp, M. Hölzel, W. Jo, A. Cevellino, H. Ehrenberg, H. Fuess, "Field-induced phase transition in $Bi_{1/2}Na_{1/2}TiO_3$-based lead-free piezoelectric ceramics", J. Appl. Cryst., Vol. 41 (2010) , 1314.

[105] L. A. Schmitt, M. Hinterstein, H. J. Kleebe, H. Fuess, "Comparative study of two lead-free piezoceramics using diffraction techniques", Appl. Cryst., Vol. 43 (2010), 805.

[106] W. Jo, T. Granzow, E. Aulbach, J. Rödel, D. Damjanovic, "Origin of the large strain response in $(K_{0.5}Na_{0.5})NbO_3$-modified $(Bi_{0.5}Na_{0.5})TiO_3$-$BaTiO_3$ lead-free piezoceramics", J. Appl. Phys., Vol. 105 (2009).

[107] R. D. Shannon, "Revised effective ionic radii and systematic studies of interatomic distances in halides and chalcogenides". Acta Cryst. Vol. 32 Sec. A (1976), 751.

[108] W. Jo, S. Schaab, E. Sapper, L. A. Schmitt, H. J. Kleebe, A. J. Bell, J. Rödel, "On the phase identity and its thermal evolution of lead-free $(Bi_{1/2}Na_{1/2})TiO_3$- 6 mol.% $BaTiO_3$", submitted.

[109] G. W. H. Höhne, W.F. Hemminger, H.J. Flammersheim, "Differential Scanning calorimetry", 2nd revised and enlarged edition, Springer (2003), Chapters 3 and 6.

[110] G. A. Samara, "Ferroelectricity Revisited-Advances in Materials and Physics", Sol. State Phys. (2001), Vol. 56.

[111] D. Viehland, S.J. Jang and L.E. Cross, M. Wuttig, "Freezing of the polarization fluctuations in lead magnesium niobate relaxors", J. Appl. Phys., Vol. 68 (1990).

[112] A. Levstik, Z. Kutnjak, C. Filipic, R. Pirc, "Glassy freezing in relaxor ferroelectric lead magnesium niobate", Vol. 57 Sec. B (1998).

[113] X. Dai, Z. Xu, D. Viehland, Long-time Relaxation from Relaxor to Normal Ferroelectric State in $Pb_{0.91}La_{0.06}(Zr_{0.65}Ti_{0.35})O_3$, J. Am. Ceram. Soc. Vol. 79 (1996), 1957.

[114] R. Jimenez, B. Jimenez, J. Carreaud, J. M. Kiat, B. Dkhil, J. Holc, M. Kosec, M. Alguero, "Transition between the ferroelectric and relaxor states in $0.8Pb(Mg_{1/3}Nb_{2/3})O_3$-$0.2PbTiO_3$", Phys. Rev. Vol. 78 Sec. B (2006).